Numerical Computations in Conformal Field Theory

by

Charles Hussong

A dissertation submitted to The Johns Hopkins University
in conformity with the requirements for the degree of
Doctor of Philosophy

Baltimore, Maryland
August 2018

Abstract

This thesis discusses two major computational projects in conformal field theory (CFT) and the interpretation of their results. The first, concerning the Virasoro Conformal Blocks of 2-dimensional CFT, uses dynamic programming and extreme precision arithmetic to prove that information is not lost after it falls into a black hole in 3-dimensional anti-de Sitter spacetime. The second, a 3-dimensional realization of a generic CFT technique called conformal truncation, uses a truncated basis of operators to naturally map CFT questions to finite-dimensional linear algebra problems, then solves them with dynamic programming and large matrix methods. To demonstrate the correctness of the program, we use it to show the closure of the mass gap in the 3D Ising model.

Thesis Committee

Primary Readers

Jared Kaplan (Primary Advisor)
Assistant Professor
Department of Physics and Astronomy
Johns Hopkins University

Ibrahima Bah
Assistant Professor
Department of Physics and Astronomy
Johns Hopkins University

Andrei Gritsan
Professor
Department of Physics and Astronomy
Johns Hopkins University

David Yarkony
Professor
Department of Chemistry
Johns Hopkins University

Lan Cheng
Assistant Professor
Department of Chemistry
Johns Hopkins University

Table of Contents

List of Figures

Chapter 1

Introduction

The study of theoretical particle physics has been dominated by relativistic quantum field theory (QFT) since the middle of the last century [1]. By far the most well-known outgrowth of QFT is the standard model of particle physics, which is by many measures the most precise and accurate scientific theory ever created. QFT is extremely versatile, however: in addition to the scattering of unimaginably tiny particles inside a collider[2], it can equally be used to model things as large as a condensed matter experiment on a tabletop[3] or a black hole more massive than the sun[4]. Accordingly, if we can detach ourselves from models of particular systems and instead focus on results about the structure of QFT itself, we can apply that knowledge to very diverse scenarios and answer questions from unexpected angles. This is essentially the goal of research into pure conformal field theory.

We will go into more detail about the concrete nature of conformal field theory in chapter 2, but roughly speaking, conformal field theories are quantum field theories which behave in qualitatively the same way at any length scale (or, equivalently, energy scale). The standard model is not a CFT: most

particles have mass energy, so if the total energy of a system is below this, it's not possible for that particle to be created, meaning that physics is qualitatively different below and above this threshold. However, many interesting quantum systems *can* be modeled as CFTs, particularly in condensed matter, where the Ising model near its critical point is the most famous example. Additionally, even though particle physics models are generally not CFTs overall, they act like CFTs near fixed points of the renormalization group[5].

Perhaps even more intriguing is the relatively recently-discovered AdS/CFT correspondence[6]. This is a series of mathematical proofs showing an exact, one-to-one correspondence between processes in a conformal field theory with d spacetime dimensions and quantum gravity processes in anti-de Sitter spacetime with $d+1$ dimensions (roughly, the most generic $d+1$-dimensional spacetime having a tendency to collapse in on itself). This correspondence can be thought of as akin to that between an object in a candlelit room and its shadow: when one moves, the other must move as well, because they are really two views of the same thing.

The AdS/CFT correspondence is much stronger than this, however: looking at a shadow, one might easily mistake the head of a duck for a human prankster's hand, or vice versa, but quantum operators in the "shadow" CFT contain *all* of the information in their AdS counterparts, such that it's always possible in principle to deduce the full situation in AdS by looking solely at the CFT, and vice versa. In fact, the information parity is so complete that there is no sense in which one side of the correspondence is more "real" than the other: they are merely two ways of thinking of the same phenomenon.

The discovery of this correspondence has presented an enormous opportunity for theoretical physics: any result about a generic CFT can equally be interpreted through the lens of quantum gravity, and likewise any result from gravity which holds in a maximally symmetric theory with a negative cosmological constant can be translated into a statement about generic conformal field theories. Furthermore, many questions with no hint of a clear answer in their own domain can be mapped to a dual question on the other side, answered there, and then the answer can in turn be mapped back to the original domain. The first project presented in this thesis, described in chapter 3, is an example of this strategy.

Because generic CFT results can be applied to so many problems in areas as diverse as particle physics, quantum gravity, and condensed matter, they are quite eagerly sought by physicists of all stripes. The standard way to produce these results is by careful mathematical proofs. As in pure math, however, there are many questions with interesting implications for which no solid proof is forthcoming. In these cases, one can often find sufficiently good approximate answers by modelling the problem numerically on a computer. This thesis presents two cases where numerical methods successfully uncovered new insights into previously unsolved generic CFT problems.

The first case, described in chapter 3, involves the black hole information paradox. The behavior of objects falling into black holes is a quantum gravity process, which under the AdS/CFT correspondence can also be viewed as a process inside a generic CFT. This process is governed by the so-called Virasoro Conformal Blocks, a class of functions. The blocks are constrained by

conformal symmetry to have a particular form, but this form is known only obliquely through various unsolved equations. Accordingly, if we can narrow down the form of these functions, we can inspect them for insights into the gravitational processes at work around black holes. In this project, we used a novel algorithm to approximate the Virasoro blocks to a level which was previously impossible, and thereby extract previously unknown information about the controversial topic of black hole decay.

The second case, described in chapter 4, concerns the explicit calculation of a number of observables in some generic CFTs using the method of *conformal truncation*. Quantum states in a conformal field theory can be classified by their eigenvalues under dilatations of spacetime; these eigenvalues, Δ, are called the *scaling dimensions* or *conformal weights* of the states.

There is a lot to say about scaling dimensions, which will be discussed in a bit more detail in chapter 2, but two properties are particularly important for this application: firstly, over relatively long distances, states with lower scaling dimensions are more important; secondly, there is a minimum scaling dimension, but no maximum (they continue increasing forever). Therefore, while there are an infinite number of states in total, we can naturally restrict this to a finite number by imposing a cutoff and only considering states below that cutoff. As we will discuss, these states with lower dimension will be more relevant to low energy (long distance) physics, so when that's what we're interested in, we should expect to reproduce important behaviors using this finite set of states. We were able to show that this is indeed the case in three spacetime dimensions, and created a program for approximately determining

the elements of this basis and their interactions with each other. This information can be used to parley information about CFTs into information about low energy non-conformal QFT phenomena.

Chapter 2

Conformal Field Theory

2.1 What is CFT?

I will begin by briefly explaining the relevant aspects of conformal field theory. As I mentioned before, conformal field theory is the study of quantum fields which are broadly stationary under infinitesimal conformal transformations; in physics, these transformations can be understood as all those with the following action on the metric $g_{\mu\nu}$[5]:

$$g_{\mu\nu} \to \Omega(x) g_{\mu\nu}, \tag{2.1.1}$$

where $\Omega(x)$ is a function which can depend on the coordinates in any way, but crucially is applied to every entry of the metric tensor democratically. Transformations of this form are angle-preserving, in that all vectors which are orthogonal on the old metric will also be orthogonal on the new metric, and vice versa. Indeed, the conformal transformations can be thought of as being defined as the members of the group of angle-preserving maps, which will be more familiar to those with a background in mathematics. In fact, in

two dimensions they are quite the same as the conformal maps which are used extensively in complex analysis. In the context of general relativity, being angle-preserving means that these transformations also preserve causality, so they can also be thought of as the most general group of causality-preserving spacetime symmetries.

It turns out to be quite straightforward to enumerate the conformal group's constituent transformations: they are the Poincaré transformations of special relativity, along with scaling of all coordinates by a constant $\vec{x} \to a\vec{x}$ (usually referred to as dilatation), and inversion of spacetime $\vec{x} \to \vec{x}/x^2$; both of these have been centered on $\vec{0}$, but of course they could be performed about any point. If we want to preserve orientations in addition to angles, then we have to replace the inversion with a *special conformal transformation*, which is an inversion followed by a translation followed by a second inversion to return to the original orientation; these operations are sufficient to reproduce all orientation-preserving conformal maps.

If one demands that a theory[1] respects conformal symmetry, then the conformal operators $\mathcal{O}$ representing its quantum states must behave in a particular way under infinitesimal conformal transformations, such as the

[1] In particle physics parlance, '**a** theory' means a mathematical model for some system (possibly the whole universe) which includes an inventory of degrees of freedom (generally particles) and a prescribed method for calculating their evolution through spacetime. 'A [relativistic] quantum field theory' means a theory whose degrees of freedom are quantum fields which are symmetric under Poincaré transformations; 'a conformal field theory' is a QFT which is symmetric under all conformal transformations. One can think of 'a CFT' as being a particular instantiation of the more general concept of conformally symmetric models.

infinitesimal dilatation D:

$$[D, \mathcal{O}_\Delta] = (\Delta + x^\mu \partial_\mu)\mathcal{O}_\Delta. \tag{2.1.2}$$

Δ, the dilatation eigenvalue, is known as the *[scaling] dimension* of the operator $\mathcal{O}_\Delta$, and is an inherent feature of the operator which is not changed by coordinate transformations. This can be exponentiated to produce the following behavior under full coordinate scaling:

$$\mathcal{O}_\Delta(ax) = a^{-\Delta}\mathcal{O}_\Delta \tag{2.1.3}$$

which is the origin of the term *dimension*: in ordinary old-fashioned geometry, when the reference length scale is doubled in every direction, the size of a 3-dimensional object decreases by a factor of 2^3, so the scaling dimension of a cube is $\Delta = 3$.

2.2 Correlation Functions and the OPE

Naturally, there is much, much more which could be said about CFTs, but the other concept which is central to this paper is the *correlation function*. This is not originally a CFT concept, but due to the restrictions imposed by conformal symmetry, it takes a central role in the CFT world: since the two scalar operators $\mathcal{O}_\Delta$ and $\mathcal{O}_{\Delta'}$ have definite behavior under dilatations and their correlation function must be a scalar due to Poincaré invariance, we can

make the following conclusion:

$$\langle \mathcal{O}_\Delta(ax)\mathcal{O}_{\Delta'}(ax')\rangle = \left\langle a^{-\Delta}\mathcal{O}_\Delta(x)a^{-\Delta'}\mathcal{O}_{\Delta'}(x')\right\rangle \tag{2.2.1}$$

$$= f((ax-ax')^2) = a^{-\Delta-\Delta'}f((x-x')^2) \tag{2.2.2}$$

so the correlation function of two conformal operators is another conformal operator whose scaling dimension is the sum of the two constituent ones. In a non-interacting theory, the new operator is the simplest possible one:

$$f((x-x')^2) = \frac{C(\Delta)\delta_{\Delta\Delta'}}{(x-x')^{2\Delta}} \tag{2.2.3}$$

where $C(\Delta)$ is some constant number; we can get rid of this as well by redefining $\mathcal{O}_\Delta \to \mathcal{O}_\Delta/\sqrt{C_\Delta}$, which is always done in practice.

This procedure is closely related to that of the *operator product expansion*, or OPE, which says that the product of two operators located very near each other can be represented as a single operator of its own, which can in turn be represented as an expansion in (i.e. sum over) other operators in the theory with some constant coefficients λ:

$$\mathcal{O}_A\mathcal{O}_B = \mathcal{O}_{\text{complicated}} = \sum_i \lambda_{ABi}\mathcal{O}_{i,\text{simple}}. \tag{2.2.4}$$

Note the lack of brackets: this is not a statement about correlation functions of operators, but rather one about literally expressing the operators themselves in a new way; (2.2.2) can be recovered by placing brackets around the resulting expression, causing everything except the identity (2.2.3) to vanish because conformal symmetry forbids one-point expectation values for operators.

Once we know that it's possible to replace pairs of operators by their OPE,

a natural next question is "does this mean that any combination of arbitrarily many operators can be reduced to a sum over single ones?" The answer is yes, and it turns out there's a great deal one can say about these sums. Consider a 4-point correlation function

$$\langle \mathcal{O}_A \mathcal{O}_B \mathcal{O}_C \mathcal{O}_D \rangle = \sum_i \sum_j \lambda_{ABi} \lambda_{CDj} \langle \mathcal{O}_i \mathcal{O}_j \rangle . \tag{2.2.5}$$

The $\langle \mathcal{O}_i \mathcal{O}_j \rangle$ above are called *conformal blocks* and are fixed by conformal symmetry to always be the same for a given $\mathcal{O}_i$ and $\mathcal{O}_j$, so if a complete set can be characterized, they can be used to express correlation functions of any set of four operators (and, in principle, arbitrarily large correlation functions as well). In chapter 3 we numerically characterize the 2-dimensional conformal blocks and then build four-operator states representing black hole dynamics with them.

2.3 AdS/CFT Holography

In addition to being used to describe systems which are themselves conformally symmetric (or perhaps merely approximately so), conformal field theory can also be applied to superficially unrelated problems in quantum gravity. This is due to the AdS/CFT Correspondence, which conjectures that states in a conformal field theory are exactly dual to states in a theory of quantum gravity in anti-de Sitter spacetime, the maximally symmetric spacetime with a negative cosmological constant[6]. The correspondence is such that any dynamic process on either side must have a dual process on the other side, which is itself a perfectly natural process in its own domain. Crucially, there is

no sense in which one of these processes is 'real' and the other is an 'image' of it – they are both valid independently, and neither side can intrinsically be taken to be more fundamental than the other. The two sides are descriptions of the same thing in two different languages: words, inflection, and even the structure of the sentences may be totally different, but they're still talking about the same object and are capable in principle of expressing all the same ideas about it.

There is no generic proof of the AdS/CFT correspondence, but it has been extensively 'tested' in the sense that it has been used to approach many complicated problems in ways which have produced reasonable (or known-true) results[7]. Furthermore, a number of simple quantities can be explicitly shown to be equivalent – consider AdS_{d+1} in compactified global coordinates, which looks like a cylinder with the metric

$$ds^2 = \frac{1}{\cos\rho}\left(-dt^2 + L^2 d\rho^2 + L^2 \sin^2\rho\, d\Omega_{d-1}^2\right) \tag{2.3.1}$$

where t is an infinite temporal coordinate, ρ is a compact spatial coordinate running from 0 to $\pi/2$, and L is a constant physical length scale which is a property of this particular instantiation of AdS.

The reason for using the compactified coordinates is apparent if one considers the null geodesics of the spacetime: from the metric, we see immediately that such a geodesic in the $+t$ and $+\rho$ directions will follow a path given by $\rho(t) = t/L$, and will therefore reach $\rho = \pi/2$ in finite coordinate time. Spatial infinity in AdS is thus causally connected to the interior, making it sensible to compute correlations between so-called 'bulk' operators on the

$d+1$-dimensional interior and 'boundary' operators on the d-dimensional surface at spatial infinity.

As an explicit example of an exact correspondence, consider a free bulk scalar field ϕ with mass M. We will write this field in so-called Poincaré coordinates, which cover a wedge-shaped patch of AdS:

$$ds^2 = \frac{L^2}{z^2}\left(-dt^2 + dz^2 + \sum_i^{d-1} dx_i^2\right) \tag{2.3.2}$$

where $z \in (0,\infty)$ and $z \to 0$ is the wall of the cylinder ($z \to \infty$ is the single point on the boundary on the far side); the other coordinates are in $(-\infty,\infty)$, just like the usual ones for flat spacetime; in particular, at constant z, this is just Minkowski space with all distances scaled by L/z.

ϕ obeys the Klein-Gordon equation; since the metric is Minkowski at constant z, we can use Minkowski momentum space for all directions except z. If the momenta in these non-z directions is k^μ, the Klein-Gordon equation becomes

$$-M^2\phi = z^{1+d}\partial_z z^{1-d}\partial_z\phi - (M^2 + k_\mu k^\mu z^2)\phi = 0 \tag{2.3.3}$$

The solutions to this are Bessel functions, producing mode functions of the form

$$\phi(x,z) = e^{ik_\mu x^\mu} z^{\frac{d}{2}} J_\nu(\kappa z) \tag{2.3.4}$$

where $\nu = \sqrt{\frac{d^2}{4} + M^2}$.

Now, when we bring this field to the boundary at $z \to 0$, the leading z behavior becomes the power law $z^{\frac{d}{2}+\nu}$. If we want to find a conformal operator corresponding to this field, the natural next question is "if we ignore this z

dependence, is the rest of the field conformal?" It turns out that the answer is yes: because the original field is a scalar under the AdS isometries, if we take the transformation $x, z \to ax, az$, ϕ remains the same, which means 'ϕ ignoring the z dependence', i.e. $\lim_{z\to 0} z^{-\frac{d}{2}-\nu}\phi(x,z)$, is rescaled by $a^{-\frac{d}{2}-\nu}$. This is precisely the required dilatation behavior for a conformal operator, so by doing this we have produced an $\mathcal{O}_\Delta$ with $\Delta = \frac{d}{2} + \nu$. This means that any free massive field in AdS_{d+1} can be placed in exact correspondence with a particular operator in CFT_d, and the converse is also possible by merely attaching the Bessel function!

Unfortunately, this so-called 'dictionary' between fields and operators relies on the free equations of motion holding, so it's not strictly true in interacting theories, though it holds up to calculable corrections in weakly-interacting theories[8]. The conjecture of the AdS/CFT correspondence is substantially stronger than this, though: it is that *any* state in *any* AdS_{d+1} can be expressed in terms of operators in a CFT_d, and vice versa. While the simple proof only works for free theories, time and again we find that observables in general theories (particularly N-point correlation functions) are in exact correspondence with those of their dual theory, so the vast preponderance of circumstantial evidence suggests that the more general statement of the correspondence is also true[7].

Broadly speaking, practical research into AdS/CFT tends to focus on taking problems which are intractable in either quantum gravity or conformal field theory, translating them into the other language, answering them there, and then translating the results back into the terms of the original problem. This

is particularly useful in quantum gravity, where extremely few problems are readily solved, and about which very little is known. The next chapter of this thesis concerns one such project, and we will now turn to its particulars.

Chapter 3

Virasoro Blocks and the Black Hole Information Paradox

Adapted from a "A Numerical Approach to Virasoro Blocks and the Information Paradox," a collaboration with Hongbin Chen, Jared Kaplan, and Daliang Li

3.1 Introduction and Summary

Many of the most challenging conceptual problems in theoretical physics were only resolved after physicists discovered how to 'shut up and calculate' a large variety of observables to high precision. For example, our modern understanding of quantum field theory was only developed after the physics community had decades of experience with perturbative calculations. And it is hard to imagine how decoherence could have been understood without the temporary crutch provided by the Copenhagen interpretation and its instrumental approach to the Born rule.

Though we have struggled with the black hole information paradox for decades, major progress has been possible through the development of AdS/CFT.

Resolving the information paradox in AdS/CFT will require a precise understanding of bulk reconstruction and its limitations. Although reconstruction presents thorny conceptual problems, the limitations on reconstruction should ultimately stem from discrepancies between the predictions of gravitational effective field theory in AdS and conformal field theory. This means that to make progress, it will be crucial to be able to directly compare the approximate correlation functions of bulk EFT and the exact correlators of the CFT.

AdS_3/CFT_2 may provide the best opportunity for such comparisons. Many features of quantum gravity in AdS_3 can be understood 'kinematically' as a consequence of the structure of the Virasoro algebra. To be specific, the Virasoro conformal blocks have a semiclassical large central charge limit that precisely accords with expectations from AdS_3 gravity, reproducing the physics of light objects probing BTZ black holes. In the semiclassical approximation, the Virasoro blocks exhibit information loss in the form of 'forbidden singularities' and exponential decay at late times [9–14]. Moreover, these problems can be partially addressed by performing explicit analytic calculations [15]. The blocks can also be computed directly from AdS_3 [16–23].

In this work we will investigate the discrepancies between semiclassical gravity and the exact CFT by computing the Virasoro blocks numerically to very high precision. This is possible via a slightly non-trivial implementation of the Zamolodchikov recursion relations [24–26]. We discuss the blocks and the algorithm in detail in section 3.2 and appendix 3.A. For the remainder of the introduction we will explain the physics questions to be addressed and summarize the results.

When is the Semiclassical Approximation Valid?

The Virasoro conformal blocks have a semiclassical limit. CFT_2 correlators can be written in a Virasoro block decomposition as

$$\langle \mathcal{O}_1(0)\mathcal{O}_2(z)\mathcal{O}_3(1)\mathcal{O}_4(\infty)\rangle = \sum_{h,\bar{h}} P_{h,\bar{h}} \mathcal{V}_{h_i,h,c}(z)\mathcal{V}_{\bar{h}_i,\bar{h},c}(\bar{z}) \tag{3.1.1}$$

the holomorphic Virasoro blocks $\mathcal{V}_{h_i,h,c}$ depend on the holomorphic dimensions h_i of the primary operators $\mathcal{O}_i$, on an intermediate primary operator dimension h, and on the central charge c. A semiclassical limit emerges when $c \to \infty$ with all h_i/c and h/c fixed; the blocks take the form

$$\mathcal{V} = e^{-\frac{c}{6} f\left(\frac{h_i}{c}, \frac{h}{c}, z\right)} \tag{3.1.2}$$

It is natural to ask about the range of validity of this approximation – how does it depend on the kinematic variable z and the ratios h_i/c and h/c?

One reason to ask is simultaneously speculative and pragmatic – one might like to know if it is possible to explore AdS_3 quantum gravity in the lab by engineering an appropriate CFT_2 (for a concrete idea see [27]). But gravity will only be a good description if the semiclassical limit provides a reasonable approximation at accessible values of c. Unfortunately, even in the semiclassical limit the Virasoro blocks are not known in closed form for general parameters. But we can partially test the validity of this limit by computing $\frac{c_2}{c_1}\frac{\log \mathcal{V}(c_1)}{\log \mathcal{V}(c_2)}$ for $c_2 \approx c_1$, as this ratio will be 1 when the semiclassical limit holds. We plot this ratio in figure 3.7, which shows that the blocks adhere to the semiclassical form of equation (3.1.2) remarkably well (up to an important caveat to be discussed later).

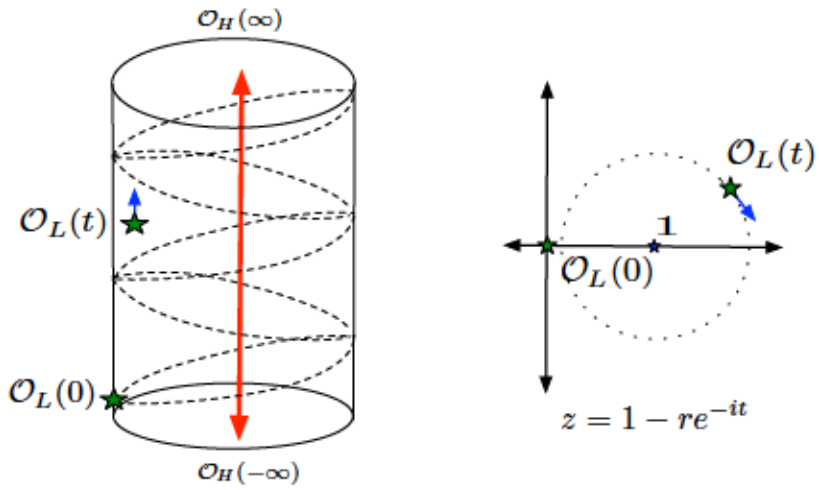

Figure 3.1: This figure suggests the analytic continuations necessary to obtain a heavy-light correlator with increasing (Lorentzian) time separation between the light operators. We take $r \lesssim 1$ to avoid singularities on the lightcones displayed on the left; one can also use r as a proxy for a Euclidean time separation between the light operators.

We would also like to understand if the semiclassical limit breaks down in specific kinematic regimes associated with quantum gravitational effects in AdS_3. This is what we will explore next.

Information Loss and OPE Convergence in a New Regime

Information loss can be probed using the correlators of light operators in a black hole background [28], as illustrated in 3.1. When computed in a BTZ or AdS-Schwarzschild geometry, these correlators decay exponentially as we increase the time separation t between the light operators, even as we take $t \to \infty$. This behavior represents a violation of unitarity for a theory with a finite number of local degrees of freedom on a compact space. Thus it is interesting to see how it is resolved by the exact CFT description.

As a first step, one would like to understand how unitary CFTs are able

to mimic bulk gravity, including the appearance of information loss. This arises from the heavy-light large central charge approximation [13–15] of the Virasoro blocks. Thus it seems to be very universal, as it is largely independent of CFT data. The next step is to understand how finite c physics corrects this approximation, and what CFT data are involved in resolving information loss.

It is useful to think about the Fourier representation of both the correlator and the individual Virasoro blocks. For the full correlator this is

$$\langle \mathcal{O}_H(\infty)\mathcal{O}_L(t)\mathcal{O}_L(0)\mathcal{O}_H(-\infty)\rangle = \int dE\, \lambda^2(E) e^{iEt} \tag{3.1.3}$$

where $\lambda(E)$ is the OPE coefficient density and we have taken $z = 1 - e^{-it}$ to study Lorentzian time separations between the light probe operators. At large t we probe the fine structure of $\lambda(E)$, which means that the least analytic features of $\lambda(E)$ dominate the late time limit. Practically speaking, this means that the very late time limit probes the discrete nature of the spectrum, and we become sensitive to the fact that $\lambda^2(E)$ is a sum of delta functions. At early or intermediate times we only discern the coarse features of $\lambda(E)$.

There are at least five different timescales associated with black holes in AdS/CFT. The inverse temperature $\beta = \frac{2\pi}{|\alpha_H|}$ where $\alpha_H \equiv \sqrt{1 - \frac{24h_H}{c}}$ sets the shortest relevant scale, where h_H is the holomorphic dimension of $\mathcal{O}_H$. The scale $\beta \log c$ estimates the time it takes for infalling matter to be scrambled [29, 30]. At times of order the entropy $S = \frac{\pi^2 c}{3\beta}$, heavy-light correlators cease their exponential decay; this is also the evaporation timescale for black holes in flat spacetime. We expect that the typical energy splittings among neighboring eigenstates to be of order e^{-S}, which means that at times of order e^S we will

be sensitive to the discreteness of the spectrum. Finally, on timescales of order e^{e^S} the phases of the eigenestates can come back into approximate alignment, leading to recurrences.

As discussed in detail in section 3.3, what we find is that the Virasoro blocks with $h_L < \frac{c}{24} < h_H$ behave very differently at early and late times, as was presaged by analytic results [15]:

- The blocks with intermediate operator dimension $h \lesssim \frac{c}{24}$ are well-described by their semiclassical limit [9, 10, 13] for

$$t \lesssim t_D \equiv \frac{\pi c}{6h_L} \tag{3.1.4}$$

  When $h > \frac{c}{24}$ the blocks are also well-described by the semiclassical limit at early times, but we do not have a precise formula quantifying 'early'.

- Heavy-light blocks with $h \gtrsim h_H$ initially grow, as was found from a semiclassical analysis [13]. We find that they reach a maximum

$$|\mathcal{V}|_{\max} \approx 16^{h-\frac{c-1}{24}} \left(\frac{h}{c}\right)^{-\frac{5}{2}h_H} \quad \text{at} \quad t_{\max} \approx A_t \sqrt{\frac{24h}{c} - 1} \tag{3.1.5}$$

  and then subsequently decay. The factor $\frac{5}{2}$ comes from empirical fits; the function $A_t(\frac{c}{h_H})$ is always order one and is approximately linear in $\frac{c}{h_H}$. Other sub-leading behavior is discussed in section 3.3.

- Numerical evidence indicates that all heavy-light Virasoro blocks decay as

$$|\mathcal{V}(t \gg t_D)| \propto t^{-\frac{3}{2}} \tag{3.1.6}$$

at late times, independent of h and c, as long as $h_H > \frac{c}{24} > h_L$. We present evidence that this decay persists beyond the exponentially long timescale $\sim e^S$, so we believe that it represents the true asymptotic behavior of the heavy-light blocks.

From the point of view of the $\frac{1}{c} \propto G_N$ expansion, the universal late-time power-law decay comes from non-perturbative effects. If this behavior persists to all times, as our empirical evidence indicates, then the late time behavior of CFT_2 correlators must come from an infinite sum over Virasoro blocks in the heavy-light channel.[1]

From a pure CFT perspective, the late Lorentzian time behavior represents a new limit in which the bootstrap may be analytically tractable. Most analytic bootstrap results, including the Cardy formula [31], OPE convergence [32], and the lightcone OPE limit [33, 34] arise in a similar way. In fact, because the expansion of CFT_2 correlators in the uniformizing q-variable, defined in (3.2.2), converges everywhere, including in deeply Lorentzian regimes, it affords the opportunity to explore many new 'analytic bootstrap' limits.

Forbidden Singularities and Bulk Reconstruction

It is interesting to understand when exact CFT correlators differ markedly from predictions obtained from a semiclassical AdS description. The late time regime we discussed above provides one example of this phenomenon. As we discuss here and in section 3.4, there are also Euclidean regimes where the

[1] In the $\mathcal{O}_H\mathcal{O}_L \to \mathcal{O}_H\mathcal{O}_L$ OPE channel, the late time behavior can be understood from the discreteness of the spectrum, without including states with energies $E \gg h_H$. It appears that in the $\mathcal{O}_L\mathcal{O}_L \to \mathcal{O}_H\mathcal{O}_H$ channel one needs to include states of arbitrarily high energy.

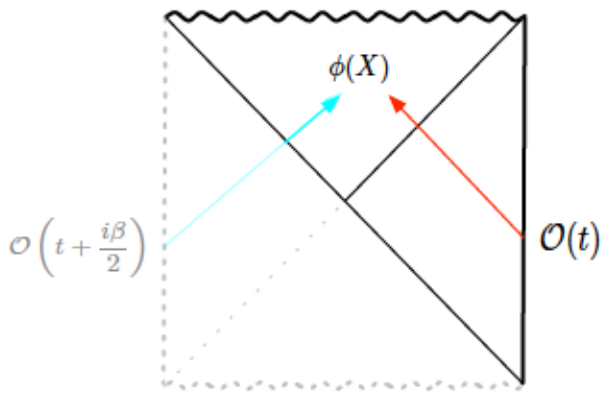

Figure 3.2: This figure shows the Penrose diagram for an energy eigenstate black hole in AdS, suggesting the role of ingoing and outgoing modes behind the horizon and their relationship with local CFT operators. Analytic continuation provides a painfully naive but instrumentally effective method for studying correlators behind the horizon.

semiclassical approximation to the Virasoro blocks fails completely.

Correlation functions in CFT_2 must be non-singular away from the OPE limits where local operators collide [15, 35]. The Virasoro conformal blocks must have this same property [13]. But in the semiclassical approximation, the blocks develop additional 'forbidden singularities' [15] that represent a violation of unitarity. These singularities are a signature of semiclassical black hole physics in AdS_3. They arise because thermal correlators exhibit a Euclidean-time periodicity under $t \to t + i\beta$, and so the OPE singularities have an infinite sequence of periodic images. The exact Virasoro blocks are not periodic, but in the semiclassical approximation they develop a periodicity at the inverse Hawking temperature $\beta = \frac{1}{T_H}$ associated with a BTZ black hole in AdS_3.

By studying the Virasoro vacuum block in the vicinity of potential forbidden singularities, one can show that at finite c the singularities are resolved in

a universal way [15] via an analytic computation. This method predicts the kinematic regimes where non-perturbative effects should become important; it can be extracted from equation 3.4.2 and the results are displayed in figure 3.17. Thus it is interesting to investigate the divergence between the exact blocks and their semiclassical approximation more generally. We study this question numerically in section 3.4.

Discrepancies between exact and semiclassical CFT correlators near the forbidden singularities could have implications for the reconstruction of AdS dynamics. Bulk reconstruction in black hole backgrounds is rather subtle [36–39], and perhaps requires some understanding of the analytic continuation of CFT correlators. But there is also a very simple and physical reason to expect that the analyic properties of correlators could have something to do with black hole interiors [36].

As emphasized by Raju and Papadodimas [40, 41], a field operator behind the horizon consists of both ingoing and outgoing modes, but only the ingoing modes can be immediately associated with local CFT operators. This issue is portrayed in figure 3.2. The analytic continuation of local operators by $t \to t + \frac{i\beta}{2}$ provides a naive, instrumental source for the outgoing modes.[2] Thus it is natural to ask whether the exact and semiclassical correlators differ

[2]This idea has significant problems. Although it may be applied to single-sided black holes, which are our object of study, it cannot then apply to the case of eternal black holes involving two different entangled CFTs. But even in the single-sided case, there is a problem because the ingoing and outgoing modes must commute, yet this property may fail when we use $\mathcal{O}(t)$ and $\mathcal{O}(t + \frac{i\beta}{2})$ for the ingoing and outgoing modes [40, 42]. It can be imposed by fiat if we take an appropriate linear combination of correlators with different analytic continuations. But this seems to require a form of state-dependence. We have discussed this procedure rather than e.g. mirror operators [40, 41] because it is easier to define in an unambiguous way. We thank Suvrat Raju and Daniel Harlow for correspondence on these issues.

significantly at $t + \frac{i\beta}{2}$, which is 'halfway' to the first forbidden singularity.

We will observe in section 3.4 that the exact and semiclassical correlators behave very similarly at these points, though they seem to differ markedly both very near (within $\frac{1}{\sqrt{c}}$) and beyond the first forbidden singularity. The results can be seen in figure 3.15. As previously discussed [15], we expect that Stokes and anti-Stokes lines emanate from the locations of the forbidden singlarities, so that different semiclassical saddle points dominate in different regions of the q-unit disk. It appears that different saddles dominate as we cross the locations of the forbidden singularities, so that the naive semiclassical blocks (the saddles that dominate near $q = 0$) are not a good approximation beyond the first singularity. In fact the semiclassical approximation appears to break down in a finite kinematic region, as shown in figure 3.17. Furthermore, the existence of such regions seems to depend in an essential way on the presence of a black hole, ie a state with energy above the Planck scale ($h_H > \frac{c}{24}$), as semiclassical/exact agreement is excellent when $h_H < \frac{c}{24}$, as we see in figure 3.18.

Perhaps future investigations will uncover bulk observables that are sensitive to Stokes phenomena in the large c expansion of the Virasoro blocks. We hope that the black hole information paradox can be understood with more precision and detail through such calculations. This work takes steps in that direction by identifying new kinematic regimes where the semiclassical limit breaks down badly and by providing results for the correct non-perturbative Virasoro blocks.

3.2 Kinematics, Convergence, and the Semiclassical Limit

A great deal of information about the behavior of CFT_2 correlation functions is encoded in the structure of the Virasoro conformal blocks. We are interested in 4-pt correlators of primary operators, which can be written as

$$\langle \mathcal{O}_1(0)\mathcal{O}_2(z)\mathcal{O}_3(1)\mathcal{O}_4(\infty)\rangle = \sum_{h,\bar{h}} P_{h,\bar{h}} \mathcal{V}_{h_i,h,c}(z)\mathcal{V}_{\bar{h}_i,\bar{h},c}(\bar{z}) \tag{3.2.1}$$

where the $P_{h,\bar{h}}$ are products of OPE coefficients. The $\mathcal{V}_{h_i,h,c}(z)$ are the holomorphic Virasoro blocks, which will be the main object of study in this work. The blocks are uniquely fixed by Virasoro symmetry and depend only on the external dimensions h_i, the exchanged primary operator dimension h, and the central charge c. Often it will convenient to write $z = \frac{4\rho}{(1+\rho)^2}$ so that the full z-plane lies inside the ρ unit circle [32]. The Virasoro blocks are not known in closed form, but they can be computed order-by-order in a series expansion using recursion relations. We provide a brief summary here, leaving the details to appendix 3.A.

There are two versions of the Zamolodchikov recursion relations (for a nice review see [43]). The first [24] is based on writing $\mathcal{V}_{h_i,h,c}$ as a sum over poles in the central charge c, plus a remainder term that survives when $c \to \infty$ with operator dimensions fixed. The second [25], which is more powerful, arises from expanding the blocks as a sum of poles in the intermediate dimension h plus a remainder term that survives as $h \to \infty$. The remainder term can be computed from the large h limit of the Virasoro blocks [25, 26]. This large h limit of the blocks takes a simple form when written in terms of the

uniformizing variable

$$q(z) = e^{i\pi\tau(z)} \equiv e^{-\pi\frac{K(1-z)}{K(z)}} \tag{3.2.2}$$

where $K(z)$ is the elliptic function

$$K(z) = \frac{1}{2}\int_0^1 \frac{dt}{\sqrt{t(1-t)(1-zt)}} \tag{3.2.3}$$

The q-coordinate can be derived from the accessory parameter/monodromy method in the semiclassical limit [44] or from a quantization of the theory on the pillow metric [35]. It has the remarkable feature that $q(z)$ covers the full multisheeted z-plane (the sphere with punctures at $0, 1, \infty$), as depicted in figure 3.3. The Virasoro blocks can then be written in the form

$$\mathcal{V}_{h,h_i,c}(z) = (16q)^{h-\frac{c-1}{24}} z^{\frac{c-1}{24}-h_1-h_2} (1-z)^{\frac{c-1}{24}-h_2-h_3} [\theta_3(q)]^{\frac{c-1}{2}-4\sum_{i=1}^4 h_i} H(c,h,h_i,q) \tag{3.2.4}$$

where $H(c,h,h_i,q)$ can be obtained from the recursion relation:

$$H(c,h,h_i,q) = 1 + \sum_{m,n=1}^{\infty} \frac{q^{mn} R_{m,n}}{h-h_{m,n}} H(c,h_{m,n}+mn,h_i,q) \tag{3.2.5}$$

We note that this recursion relation naturally produces a series expansion in the variable q. For more details along with the definitions of the quantities appearing in these equations see appendix 3.A.

In this work, we will be using the recursion relations to obtain the q-expansion of the Virasoro blocks to very high orders. It appears that most prior implementations of the Zamolodchikov recursion relations could not reach

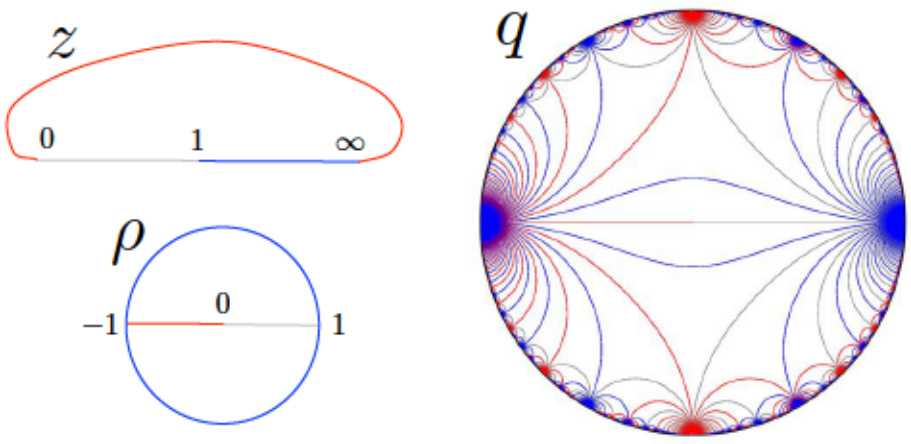

Figure 3.3: The $q(z)$ map takes the universal cover of the z-plane (the sphere with punctures at $0, 1, \infty$) to $|q| < 1$. This figure suggests the relationship between the z plane, the unit ρ disk, and the unit q disk, with branch cuts indicated with colored lines [35]. The relations between these variables are $q = e^{-\pi \frac{K(1-z)}{K(z)}}$ and $z = \frac{4\rho}{(1+\rho)^2}$, and the inverse transformations are $z = \left(\frac{\theta_2(q)}{\theta_3(q)}\right)^4$ and $\rho = \frac{z}{(1+\sqrt{1-z})^2}$. The Virasoro blocks converge throughout $|q| < 1$, with OPE limits occurring on the q unit circle.

the $N \sim 1000$ that we will study.[3] Our improvements are fairly elementary, and are based on computing and storing the specific coefficients of powers of q in $H(c, h_{m,n} + mn, h_i, q)$, as we describe in more detail in appendix 3.A. The computational time complexity of our algorithm is roughly $O(N^3(\log N)^2)$, while it seems that some earlier implementations scaled exponentially with N. The maximum N is limited by memory consumption, with memory usage scaling roughly as $O\left(N^3 \log N\right)$. We have verified our code by comparing to a number of previous results, including prior implementations, the semiclassical blocks, blocks computed by brute force from the Virasoro algebra, and the special case of degenerate external operators.

[3] Prior implementations such as this code [45] and other similar, modestly improved versions we are aware of. Perhaps [46] are using roughly the same algorithm we describe. We have only used laptops; one could perhaps achieve $N \sim 10^4$ with more computing power.

3.2.1 Kinematics and Convergence of the q-Expansion

Both the correlator and the Virasoro blocks in equation (3.2.1) can have singularities in the OPE limits, which occur when $z \to 0, 1, \infty$. Generically we expect branch cuts in the z-plane running between these three singularities. So for our purposes, the most remarkable feature of the variable $q(z)$ is that the region $|q| < 1$ covers not only the complex z-plane, but also every sheet of its cover. The relationship of the z plane and its branch cuts to the region $|q| < 1$ [35] is depicted in figure 3.3. The Zamolodchikov recursion relations provide an expansion for the Virasoro blocks that converges for all $|q| < 1$, which means that they can provide a good approximation to the 4-pt correlator in any kinematic configuration. In particular, we can use the q-expansion to study the Lorentzian regime with arbitrary time-orderings for the operators.

The existence of the q-variable implies that in CFT_2, there are an infinite number of distinct regimes where the bootstrap equation may be analytically tractable. In the case of $d \geq 3$, one can study the OPE limit $z \to 1$ using conformal blocks expanded in the OPE limit of small z, and this implies various exact results about the properties of large spin operators [33, 34, 47]. However, because the Euclidean OPE in $d \geq 3$ does not converge deep in the Lorentzian region, one cannot study other OPE channels in the same way. This obstruction disappears in $d = 2$, where one must be able to reproduce all of the distinct OPE limits $|q| \to 1$ pictured in figure 3.3 using the small q expansion. The large Lorentzian time limit that we will discuss in section 3.3 provides a physically motivated example of this idea.

We will be studying numerical approximations to the Virasoro blocks

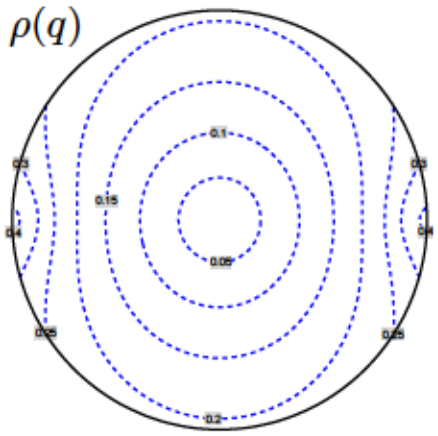

Figure 3.4: This figure displays contours of constant $|q|$ inside the ρ unit circle, which corresponds to the entire z-plane via $z = \frac{4\rho}{(1+\rho)^2}$. Since this is only the first sheet of the z-plane, it corresponds to the region in the q-disk enclosed by the two blue lines connecting ± 1 in figure 3.3. The correlator can have singularities in the OPE limits $\rho \to -1, 1$ and these correspond to $q \to -1, 1$ as well. Away from these limits $|q| < |\rho|$ and the q-expansion converges much more rapidly than the ρ expansion.

based on a large-order expansion in the q variable. Thus to understand the convergence properties of our expansion, it may be useful to map out the regions of constant $|q|$. For this purpose we can use the coordinate $\rho(z)$ defined via $z = \frac{4\rho}{(1+\rho)^2}$ [32], because the entire z-plane can be easily visualized as the region $|\rho| < 1$. The operators at $z = 1$ and ∞ are mapped to $\rho = 1$ and -1, respectively. In figure 3.4 we have plotted contours of constant $|q|$ in the ρ-coordinate system. In figure 3.5 we present results on the convergence region of the q-expansion of the Virasoro blocks for various values of the dimensions and central charge.

A kinematic configuration that will be of particular interest represents $z = 1 - re^{-it}$ (and $\bar{z} = 1 - re^{-it}$ as well) and is depicted in the AdS/CFT context in figure 3.1. With this setup we can study the correlator of light operators $\mathcal{O}_L(z)\mathcal{O}_L(0)$ at timelike separation in the background created by

a heavy operators $\mathcal{O}_H$. At large times t, this correlator can be used as a probe of information loss in pure state black hole backgrounds, as we will discuss in section 3.3. On the z plane, the late time behavior is obtained by analytically continuing the conformal block around the branch-cut starting at $z = 1$ multiple times. Explicitly, the Lorentzian value of the q variable is obtained with the following analytic continuation of the elliptic integral:

$$K|_{z\to 1-e^{-it}} = K(1-re^{-it}) - 2i\left\lfloor \frac{1}{2} - \frac{t}{2\pi}\right\rfloor K(e^{-it}), \tag{3.2.6}$$

where the elliptic functions on the right-hand side are evaluated on the principle sheet with the branch-cut chosen to be $z \in [1,\infty)$. At large t we have

$$q(t) \approx 1 + \frac{i\pi^2}{t} - \frac{\pi^4 + 2\pi^3 g(r,t)}{2t^2} + \cdots \tag{3.2.7}$$

where

$$g(r,t) = \frac{K\left(1-e^{-it}r\right)}{K\left(e^{-it}r\right)} + 2i\left\lfloor \frac{t+\pi}{2\pi}\right\rfloor - \frac{it}{\pi} \tag{3.2.8}$$

with the elliptic function $K(z)$ are taken on their principle sheet, so that $g(r,t)$ is periodic in t. This means that $|q|^2 \approx 1 - \frac{\pi^3}{t^2}(g+g^*) + \cdots$ and the real part $\mathrm{Re}[g(r,t)] > 0$, so that $|q| < 1$ for all t, as expected. In the limit that $r \ll 1$, we have $g(r,t) \approx \frac{1}{\pi}\log\frac{16}{r}$, which leads to the estimate

$$|q|^2 \approx 1 - \frac{2\pi^2 \log\frac{16}{r}}{t^2} \tag{3.2.9}$$

in the limit of $r \ll 1$ and $t \to \infty$. Thus we can translate between convergence in $|q|$ and t; very roughly, we expect that working to order q^N will allow us to probe $t \propto \sqrt{N}$ at large N. We can visualize the trajectory of $q(r,t)$ for various

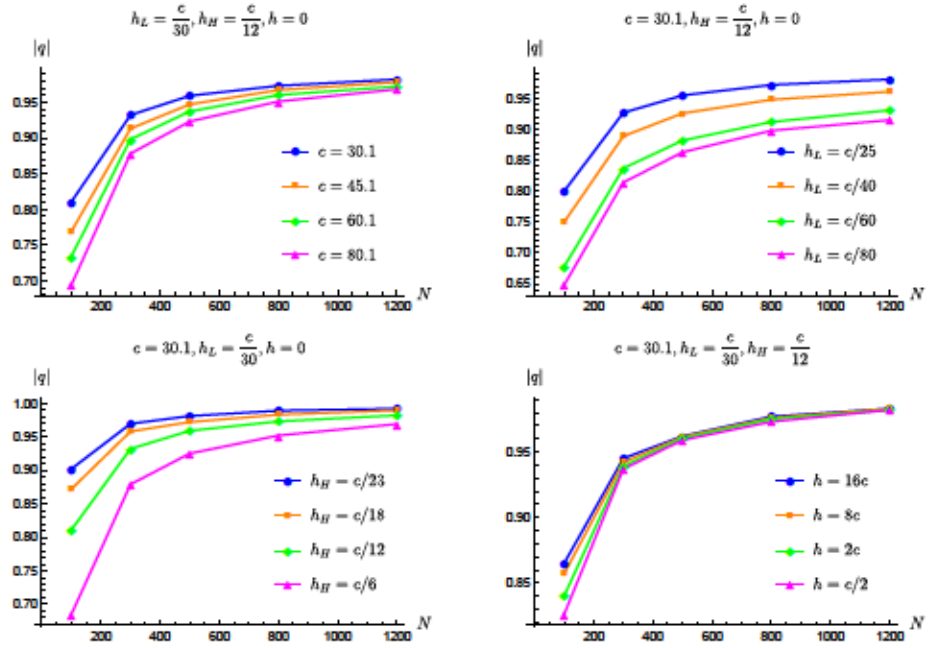

Figure 3.5: These plots display the maximum $|q|$ where the q-expansion converges for various choices of parameters. Convergence improves when h_L and h_H move closer to $c/24$ and when c decreases. The intermediate primary dimension h seems to have little effect on convergence. These plots define 'convergence' as $\left|\left|\frac{\mathcal{V}_{0.95N}(q)}{\mathcal{V}_N(q)}\right| - 1\right| < 10^{-5}$, where $\mathcal{V}_M$ includes an expansion up to order q^M.

r in figure 3.6.

3.2.2 Review of Blocks and Adherence to the Semiclassical Form

Much is known about the Virasoro blocks in various limits. In the limit $c \to \infty$ with all dimensions held fixed, the Virasoro blocks simply reduce to global conformal blocks, which are hypergeometric functions. Corrections to this result up to order $1/c^3$ are known explicitly [48]. In the heavy-light limit, where we take $c \to \infty$ with two 'heavy' operator dimensions $h_H \propto c$, and the two 'light' dimensions h_L and the intermediate operator dimension h fixed,

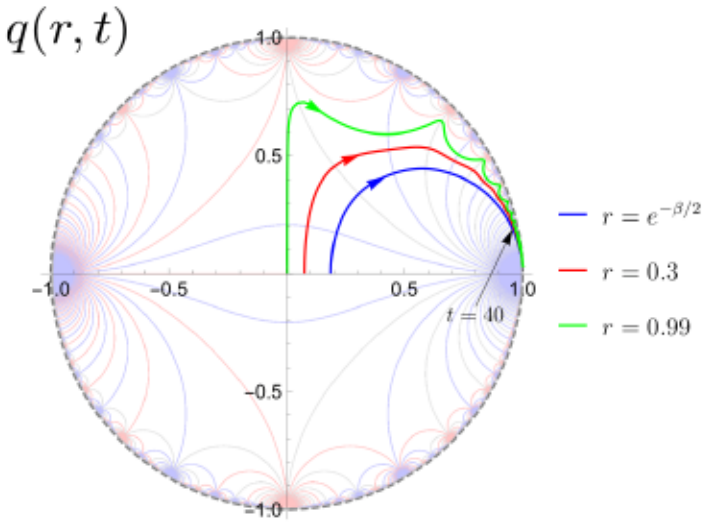

Figure 3.6: The function $q(r,t)$ for different r, where we have written $z = 1 - re^{-it}$ and plotted the lines $t \in [0, \infty)$. For the blue curve we chose $\beta = 2\pi$, which corresponds with $h_H = \frac{c}{12}$. Note that the wiggles are due to the fact that when $t = 2\pi n$ and $r \approx 1$, the coordinate z approaches an OPE singularity. The large time limit of q was given in equation (3.2.7).

the blocks take the form [10]

$$\mathcal{V} = (1-w)^{h_L \frac{\alpha_H - 1}{\alpha_H}} \left(\frac{w}{\alpha_H}\right)^{h-2h_L} {}_2F_1(h,h,2h,w) \tag{3.2.10}$$

where $w \equiv 1-(1-z)^{\alpha_H}$ and $\alpha_H \equiv \sqrt{1-\frac{24h_H}{c}}$. Note that when $h_H > \frac{c}{24}$, we have $\alpha_H = 2\pi i T_H$ where T_H is the Hawking temperature of a corresponding BTZ black hole. In the case of the vacuum block, which is $h = 0$, the $1/c$ corrections to this limit are also known explicitly [12] for any h_H/c. Finally, in the semiclassical large c limit, where all dimensions $h_i, h \propto c$, there is overwhelming evidence that the blocks take the form

$$\mathcal{V} = e^{-\frac{c}{6} f\left(\frac{h_i}{c}, \frac{h}{c}, z\right)} \tag{3.2.11}$$

as though they are derived from a semiclassical path integral (and in fact they have an sl(2) Chern-Simons path integral representation [22]). The semiclassical saddle points have been classified [13], and in some kinematic limits we can determine the behavior of f analytically. In particular, the large Lorentzian time behavior of f with the kinematics of figure 3.1 and $h_L < \frac{c}{24} < h_H$ has been determined [13]. The result is that the leading semiclassical contribution always decay exponentially at sufficiently large times[4] at the rate

$$\mathcal{V}(t) \approx \exp\left[-\frac{c}{12}|\alpha_H|\,(1-\alpha_L)\,|t|\right] \tag{3.2.12}$$

where $\alpha_L = \sqrt{1-\frac{24h_L}{c}}$ and $\alpha_H = 2\pi i T_H$ with T_H the corresponding Hawking temperature. As we will review in section 3.3, this demonstrates that information loss due to black hole physics [28] occurs as a consequence of the behavior of the individual Virasoro blocks [13, 15]. Finally, some exact information about the behavior of the Virasoro blocks can be obtained by studying degenerate states [15].

Most of these approximations hold in the large central charge limit when the kinematic configuration is held fixed. But the deviations between the exact and semiclassical Virasoro blocks may depend importantly on the kinematics. As we will discuss in detail below, the semiclassical blocks have 'forbidden singularities' that are absent from the exact blocks [15]. We also find that as expected [13, 15], the exact and semiclassical blocks have very different behavior at large Lorentzian times. More generally, we would like to map out

[4] As we increase the intermediate operator dimension this behavior may not set in until later and later times. Here we are studying late times with all other parameters held fixed.

the kinematic regimes where non-perturbative corrections to the semiclassical Virasoro blocks become large.

But at a more basic level, it is interesting to ask how large c must be before the semiclassical limit of the Virasoro blocks provides a reasonable approximation to their behavior. This has immediate implications for the possibility of constructing a 2d CFT and probing quantum gravity in an experimental lab. A natural way to probe the existence of the semiclassical limit is by studying the ratio of logarithms of blocks

$$R \equiv \frac{c_2 \log \mathcal{V}(c_1, q)}{c_1 \log \mathcal{V}(c_2, q)} \stackrel{?}{=} 1 \tag{3.2.13}$$

at somewhat different central charges c_1 and c_2. If the semiclassical limit of equation (3.2.11) is a good approximation, then this quantity will be 1, but otherwise we expect it to deviate from 1 by effects of order $\frac{1}{c}$. In figure 3.7 we explore this ratio and find that the semiclassical form $\mathcal{V} \approx e^{cf}$ provides a remarkably good approximation for very small values of c.

There is an important caveat that we will return to in section 3.4. An infinite number of distinct semiclassical saddle points can contribute to the Virasoro blocks in the large c limit [13]. Thus it is possible that $\mathcal{V} \approx e^{cf}$ for some f, but that due to Stokes phenomena, the dominant saddle f changes as we move in the q unit disk. So although the semiclassical limit may appear to describe the blocks well for all q, as indicated by figure 3.7, in fact the saddle that is leading near $q \approx 0$ may be sub-leading at general q. Thus the naive semiclassical blocks may differ greatly from the exact blocks; in fact we will find this to be the case in section 3.4.

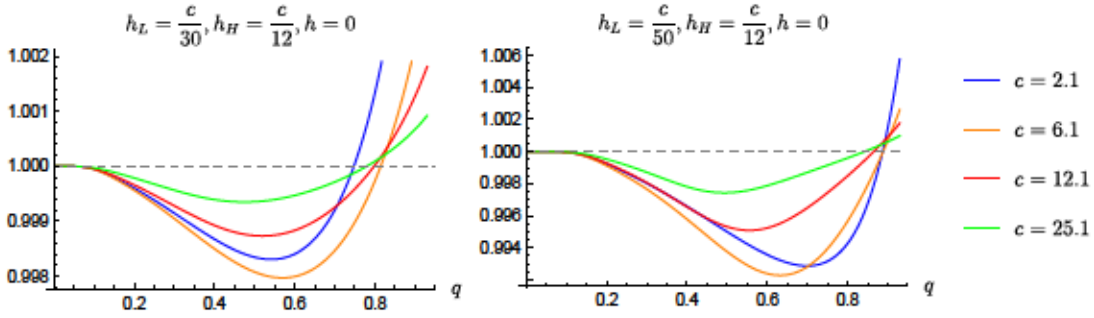

Figure 3.7: In this figure we plot $R = \frac{c' \log \mathcal{V}(c,q)}{c \log \mathcal{V}(c',q)}$ with $c' \equiv \frac{11}{10}c$ in order to test the semiclassical limit. As we increase c, the semiclassical limit becomes a better approximation and $R \to 1$, but even for $c = 2.1$ the blocks are remarkably well approximated by the semiclassical form. For the larger choices of c the functions have similar shapes up to an overall rescaling; this suggests that the first $1/c$ correction is dominating the discrepancy $R - 1$. In the OPE limit $q \to 0$ the semiclassical limit always applies. We find similar results for non-vacuum blocks.

Nevertheless, figure 3.7 suggests that we should be optimistic about probing semiclassical CFT_2 correlators in the lab! It would be very interesting to engineer a CFT_2 with $c > 1$ and no conserved currents aside from the stress tensor [27].

3.3 Late Time Behavior and Information Loss

One sharp signature of information loss in AdS/CFT [28] is the exponential decay of correlation functions at large time separations in a black hole background. This can be studied using heavy-light 4-point functions in CFT [9]. As portrayed in figure 3.1, we can interpret this correlator as the creation and subsequent measurement of a small perturbation to an initial high-energy state. In a unitary theory on a compact space with a finite number of local degrees of freedom, this initial perturbation cannot completely disappear. But a computation in the black hole background displays eternal exponential

decay, capturing the physical effect of the signal falling into the black hole. At a more technical level, the exponential decay rate can be obtained from the quasinormal mode spectrum of fields propagating in the black hole geometry.

The simplest way to see that heavy-light correlators cannot decay forever is to expand in the $\mathcal{O}_H\mathcal{O}_L \to \mathcal{O}_H\mathcal{O}_L$ channel, giving

$$\langle \mathcal{O}_H(\infty)\mathcal{O}_L(t)\mathcal{O}_L(0)\mathcal{O}_H(-\infty)\rangle = \sum_E \lambda^2(E) e^{iEt} \tag{3.3.1}$$

where $\lambda^2(E)$ is a product of OPE coefficients. Because the sum on the right-hand side is discrete, the correlator must have a finite average absolute value at late times. When $h_H \gtrsim \frac{c}{24} \gg h_L$, we expect the states contributing in (3.3.9) to be a chaotic collection of e^S blackhole microstates with energy near that of $\mathcal{O}_H$, and with $S = \frac{\pi^2}{3} T_H c$. The amplitude will initially decay due to cancellations between the essentially random phases, but these cancellations cannot become arbitrarily precise. Roughly speaking, the decay should stop when the correlator reaches $\sim e^{-S}$ and begins to oscillate chaotically. At a more detailed level, the time dependence can change qualitatively on timescales of order S and e^S as different features of $\lambda^2(E)$ come into play [49–52].

In this work, we will not study the $\mathcal{O}_H\mathcal{O}_L \to \mathcal{O}_H\mathcal{O}_L$ channel directly. Instead we work in the channel where $\mathcal{O}_H\mathcal{O}_H \to \mathcal{O}_L\mathcal{O}_L$, which is related to the first channel by the bootstrap equation (or by modular invariance in the case of the partition function [51]). In this channel we are sensitive to the exchange of states between the heavy and light operators. For example, pure 'graviton' states in AdS_3 correspond to the exchange of the Virasoro descendants of the vacuum, which are encapsulated by the Virasoro vacuum

block. Other heavy-light Virasoro blocks include a specific primary state along with its Virasoro descendants, which one can think of as gravitational dressing. We are interested in this channel because heavy-light Virasoro blocks encode many of the most interesting features of semiclassical gravity. We would like to understand to what extent the exact Virasoro blocks know about the resolution of information loss.

It is convenient to think of the time dependence of the Virasoro blocks as coming from a potentially continuous $\lambda_h(E)$ associated with each block, via

$$\mathcal{V}_h(t) = \int dE\, \lambda_h^2(E) e^{iEt} \tag{3.3.2}$$

where h labels the dimension of an intermediate Virasoro primary operator $\mathcal{O}_h$ in both the $\mathcal{O}_H(x)\mathcal{O}_H(0)$ and $\mathcal{O}_L(x)\mathcal{O}_L(0)$ OPEs. Roughly speaking, the late time dependence of $\mathcal{V}_h(t)$ will come from the least analytic features of $\lambda_h^2(E)$.

For example, in the leading semiclassical limit, heavy-light Virasoro blocks decay exponentially at late times at a universal rate given in equation (3.2.12). This semiclassical behavior comes from a function $\lambda_h^2(E)$ that is smooth on the real axis, but has poles in the complex E-plane. In AdS_3 these poles can be interpreted as the quasinormal modes of a BTZ black hole background (at least for small h). A straightforward contour deformation of equation (3.3.2) connects these poles to the exponential decay.

At sufficiently late times, the physics of the quasinormal modes will be subdominant to less analytic features in $\lambda_h^2(E)$. For example, if $\lambda_h^2(E)$ exhibits thresholds of the form $(E - E_*)^{p-1}$ with E_* real, then $\mathcal{V}(t)$ will inherit a

power-law behavior t^{-p} at late times. And if $\lambda_h^2(E)$ receives delta function type contributions, then $\mathcal{V}(t)$ will have a finite average absolute value at late times. If such features are present in $\mathcal{V}_h(t)$, then it is natural to investigate the timescale where $\mathcal{V}_h(t)$ transitions from exponential decay to some other late-time behavior.

The full CFT_2 correlator should not become much smaller than $\sim e^{-S}$. Since Virasoro blocks associated with light operators initially decay exponentially, one might naively expect that $\mathcal{V}_h(t)$ should change qualitatively after a time of order S. More specifically, for heavy-light correlators dominated by the vacuum block, we would expect a departure from exponential decay by a time

$$t_D = \frac{\pi c}{6h_L} \tag{3.3.3}$$

up to an unknown order one factor. This argument is rather weak, since the full correlator might not behave like the light-operator Virasoro blocks. However, the same prediction for t_D was derived from an analysis of non-perturbative effects [15] in the vacuum block. We discuss the equation that led to that prediction in section 3.4.3.

We will see empirically that Virasoro blocks with small h do undergo a transition at a timescale remarkably close to t_D. Furthermore, at late times the behavior of the heavy-light Virasoro blocks appears to be a universal power-law:

$$|\mathcal{V}_{h_L,h_H,h,c}(t \gg t_D)| \propto t^{-\frac{3}{2}}, \tag{3.3.4}$$

where we require $h_H \geq \frac{1}{24}$, so that at least one external operator is heavy

enough to create a blackhole. When the intermediate dimension $h \gtrsim h_H$ the late time power-law behavior remains the same, although the transition time then also depends on h (and we do not have an analytic prediction to compare to). This universal behavior suggests a threshold $\sqrt{E - E_*}$ in $\lambda_h^2(E)$, which seems to correspond with random matrix behavior [50, 53, 54]. Our results indicate that the $t^{-\frac{3}{2}}$ power-law persists to timescales $\sim e^S$, so individual heavy-light Virasoro blocks are not sensitive to the discreteness of the spectrum.

These results show that the time-dependence of the heavy-light Virasoro blocks has some qualitative similarities with that of the Virasoro vacuum character after an S transformation and the analytic continuation $\beta \to \beta + it$ [51]. Both the heavy-light blocks with small h and the vacuum character have an initial exponential-type decay, though the precise time-dependence is rather different. The heavy-light blocks and the vacuum character have the same power-law decay at late times, though non-vacuum characters decay with a different late-time power-law [51].

In what follows we will study the heavy-light blocks $\mathcal{V}_h(t)$ empirically to establish the robust features of their time-dependence. We also translate the late-time $t^{-3/2}$ behavior into a statement about the coefficients of q^N in $\mathcal{V}_h(q)$ at large orders in the q-expansion, as one might hope to derive this asymptotic behavior for the coefficients using the Zamolodchikov recursion relations. One might also compute $\lambda_h^2(E)$ directly using the crossing relation [55, 56]. Finally we discuss the implication of our results for the late time behavior of the correlator.

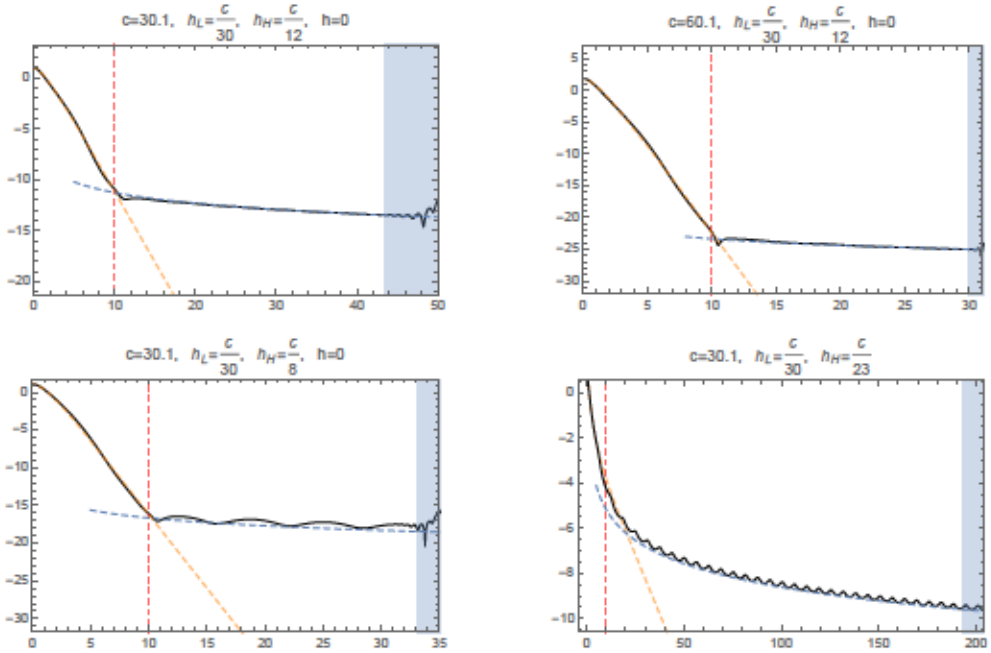

Figure 3.8: Heavy-light Virasoro vacuum blocks switch from an initial exponential decay to a slow, universal power law decay at roughly the time scale $t_d = t_D - b$, where the constant offset b depends on the choice of r in $z = 1 - re^{-it}$. The vertical axis is $\log|\mathcal{V}|$, while the horizontal axis is the Lorentzian time t. The black lines are full Virasoro vacuum blocks computed to order q^{1200}. This polynomial truncation stops converging in the shaded region. The yellow dashed lines are the semiclassical vacuum blocks using methods of [13]. The red dashed lines are the time scale (3.3.3). The blue dashed lines are the power law $at^{-\frac{3}{2}}$ with a properly chosen to match the full blocks.

3.3.1 Numerical Results and Empirical Findings

3.3.1.1 Vacuum Virasoro Blocks

Using the methods discussed in section 3.2, we compute the vacuum Virasoro blocks at late times. Figure 3.8 shows the result along with a comparison to the semiclassical blocks computed using semi-analytic methods [13]. For numerical convenience we avoid certain rational values of c to prevent singularities in intermediate steps of the computation.

Using the numerical result of the full Virasoro blocks, we can measure the departure time t_d when the semiclassical block drops below the exact block. We compare this measured value to the prediction of (3.3.3) in figure 3.9. The logic leading up to (3.3.3) is only valid parametrically, so it is remarkable that it agrees with the measured t_d up to a small constant shift. Note that we parameterize the time dependence via $z = 1 - re^{-it}$, and this constant shift depends on r. We have also checked that t_d is primarily controlled by the ratio $\frac{h_L}{c}$ and has a very weak dependence on h_H and c.

Around the time t_D, all vacuum blocks show an obvious change of behavior from an initial exponential decay to a much slower power law decay. To very good accuracy, the power of this decay seems to be $t^{-\frac{3}{2}}$ universally in all of the parameter space we were able to explore with an external operator with dimension $h_H > \frac{1}{24}$. A few examples are provided in figure 3.8, but we tested this behavior with hundreds of different parameter choices.

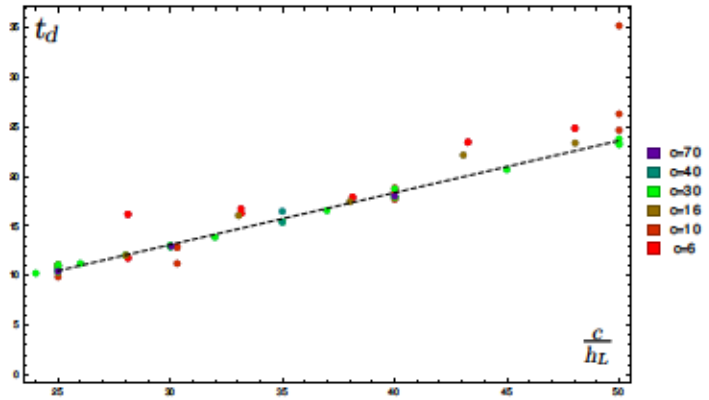

Figure 3.9: This figure displays the time t_d at which the semiclassical vacuum blocks drop below the exact vacuum blocks. The dashed line is a fit to the analytic prediction $t_D \equiv \frac{\pi c}{6h_L}$ with an empirical offset $t_d = t_D - 2.6$; the offset depends on the choice of r with $z = 1 - re^{-it}$. Note that the data with smaller values of c is noisy, but the larger values fit the linear behavior extremely well. The plot includes a variety of choices for $\frac{h_H}{c}$.

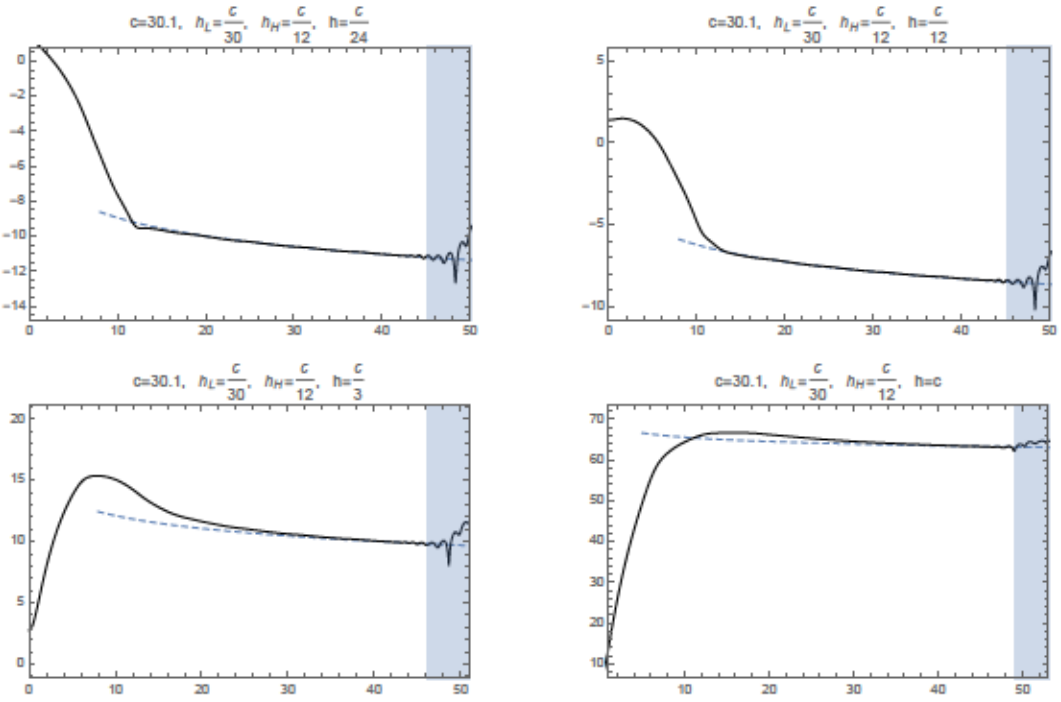

Figure 3.10: The late time behavior of various non-vacuum Virasoro blocks. The vertical axis is $\log|\mathcal{V}|$ and the horizontal axis is the time t. The black lines are full Virasoro blocks computed to order q^{1200}, plotted using $z = 1 - re^{-it}$ with $r = 0.3$. The polynomial truncation no longer converges in the shaded region. The blue dashed lines are the power law $a\,t^{-\frac{3}{2}}$ with the constant a fitted to the blocks. We refer to the time and height of the maxima as t_{max} and $|\mathcal{V}|_{\text{max}} = 16^{h-\frac{c-1}{24}}|\tilde{\mathcal{V}}|_{\text{max}}$.

3.3.1.2 General Virasoro Blocks

The non-vacuum blocks also exhibit universal $t^{-\frac{3}{2}}$ late-time decay. The difference from the vacuum case is that we no longer have a simple estimate for the time scale of the transition. In particular, we find that generically the non-vacuum blocks grow at early times, reach a maximum at time t_{max}, and then start to decay, finally settling down to the $t^{-\frac{3}{2}}$ power law behavior. These features are illustrated by examples in figure 3.10.

From the data plotted in figure 3.11, we see that beyond the blackhole

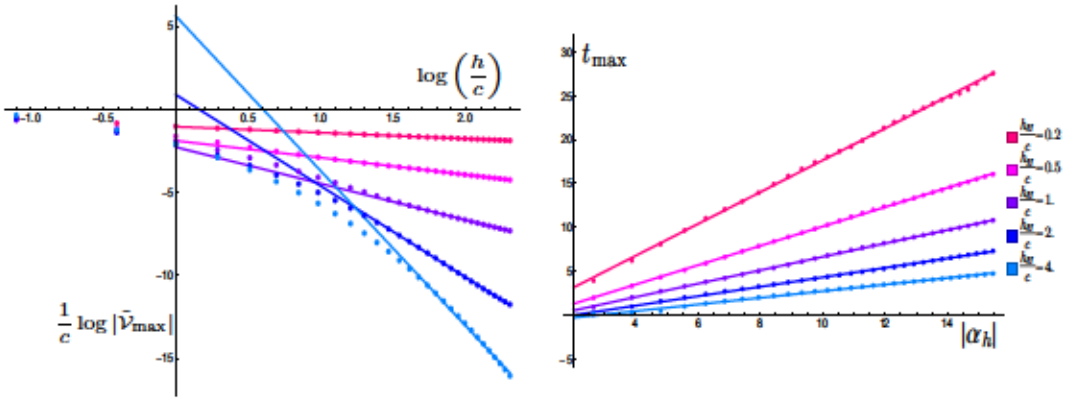

Figure 3.11: These plots show a host of data demonstrating that $|\tilde{\mathcal{V}}_{\max}|$ and $t_{\max}$ have simple dependence on $\frac{h}{c}$ when $h \gtrsim h_H$ (recall $\alpha_h \equiv \sqrt{1-\frac{24h}{c}}$) for a large variety of different choices of h_H. For all of these plots we choose $c = 10$, but we have found that the results are robustly c-independent. These plots use $h_L = \frac{c}{30}$, but h_L dependence is mild, as seen in figure 3.12.

threshold $h > \frac{c}{24}$, the timescale $t_{\max}$ has a simple dependence on parameters. We can fit it to the ansatz

$$t_{\max} = A_t|\alpha_h| + b_{\text{time}} \tag{3.3.5}$$

with $\alpha_h = \sqrt{1-\frac{24h}{c}}$ and obtain A_t and b_{time} empirically. The parameter A_t is almost a linear function of $\frac{c}{h_H}$, as can be seen in figure 3.12, with virtually no dependence on other parameters such as h_L. It approaches $A_t \approx \frac{c}{2h_H} +$ constant when $h_H \gtrsim \frac{c}{2}$. For smaller values of h_H we find $\frac{1}{2} \geq \frac{dA_t}{d(c/h_H)} \geq \frac{1}{5}$. We cover a larger range of h_H in figure 3.22 in the appendix, which displays the variation in A_t.

On the left of figure 3.11 we plot $|\tilde{\mathcal{V}}_{\max}|$, which is the maximum of the absolute value of the block after extracting a universal prefactor via $|\mathcal{V}_{\max}| = 16^{h-\frac{c-1}{24}}|\tilde{\mathcal{V}}_{\max}|$. We see that $|\tilde{\mathcal{V}}_{\max}|$ also has a simple dependence on $\frac{h}{c}$. We can

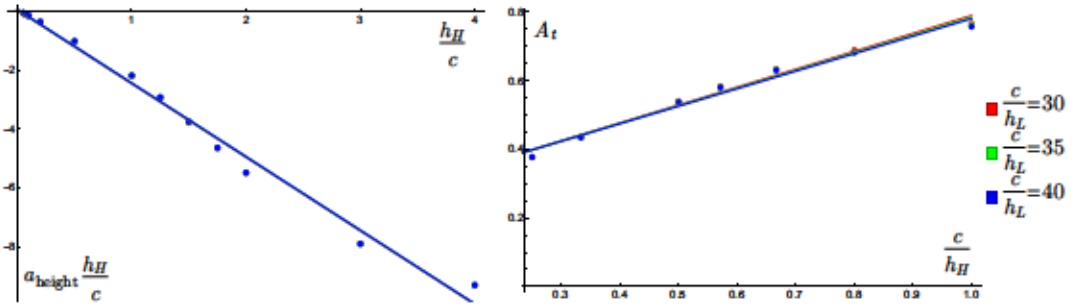

Figure 3.12: We have found empirically that the time and height of the maxima of heavy-light Virasoro blocks have a simple dependence on both h and h_H. This figure shows linear fits used to obtain the parameters a_{height} and A_t defined in equations (3.3.6) and (3.3.5). These plots both have $c = 10$. Each point is obtained from the slope of $\frac{\log|\tilde{\mathcal{V}}_{\text{max}}|}{c}$ and t_{max} as linear functions of $\log\frac{h}{c}$ and $|\alpha_h|$ respectively (we've used points with $\frac{h}{c} = \frac{n}{3}$ for $n = 1, 2, \cdots, 30$). We find that both plots are robustly c-independent for $c \gtrsim 5$, as expected in the semiclassical limit. We see explicitly that there is little dependence on h_L; in the a_{height} plot the variation with h_L is almost invisible.

perform a similar fit for $|\tilde{\mathcal{V}}_{\text{max}}|$, and we find that

$$\frac{\log|\tilde{\mathcal{V}}_{\text{max}}|}{c} = a_{\text{height}}\frac{h_H}{c}\log\frac{h}{c} + b_{\text{height}} \tag{3.3.6}$$

Empirically we obtain $a_{\text{height}} \approx -2.5$ from the fit in figure 3.12. The b_{time} and b_{height} parameters do not fit a simple pattern; we provide some data on these parameters in figure 3.21 in the appendix. These fits led to the result summarized by equation (3.1.5) in the introduction, which neglects the small offsets from the b-parameters. We expect that $|\mathcal{V}_{\text{max}}|$ and t_{max} are controlled by semiclassical physics (for example, see figure 3.20), so it would be interesting to try to prove these empirical relations using analytic results [13] on the semiclassical time-dependence. In principle these results could also be obtained from an AdS calculation involving black holes and deficit angles.

3.3.1.3 Probing Exponentially Large Timescales

Formally, we are interested in high-energy pure states corresponding to BTZ black holes, which have a large entropy $S = \frac{\pi^2}{3} c T_H$ in the large central charge limit where AdS gravity provides a reliable description. This suggests that timescales of order e^S will be unreachably large. Nevertheless, by considering either small c or small T_H, we can probe order one S, and thus reach $t \sim e^S$ within the range of convergence of our numerics.

In fact, the plot on the bottom-right of figure 3.8 is already in this regime. Due to its low temperature of $T_H \approx 0.03$ in AdS units, we have $S \approx 3.3$ so that times of order $e^S \approx 27$ are within the range of convergence. Thus this plot already suggests that the $t^{-\frac{3}{2}}$ power-law decay persists to exponentially large timescales. In figure 3.13 we have displayed four other choices of parameters where timescales of order e^S, and even e^{e^S}, are visible within the range of convergence. Two examples have order one T_H and small c, while two others have very small T_H and relatively large c. In all cases we see that the $t^{-\frac{3}{2}}$ late-time decay persists on these exponentially large timescales. This provides good evidence that the heavy-light Virasoro blocks really do decay in this way at very late times. This means that these blocks are not sensitive to the discreteness of the spectrum in other channels.

3.3.2 Power Law Behavior of q-Expansion Coefficients

We have observed an apparently universal late-time power-law behavior in the heavy-light Virasoro blocks $\mathcal{V}_h(t)$. One might try to derive this behavior by studying its implications for the q-expansion. In fact, for a large region

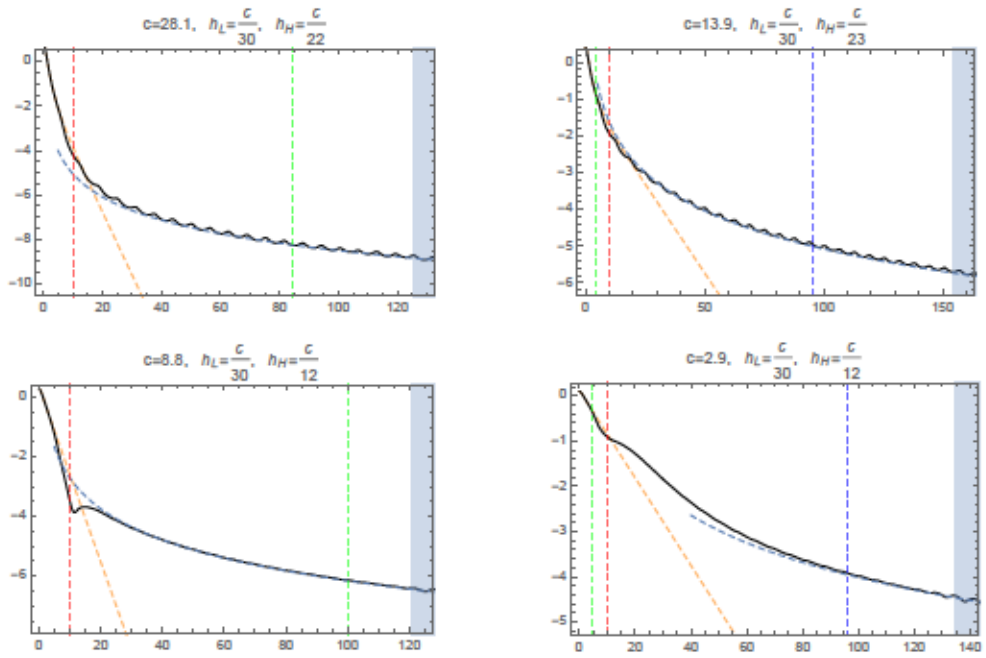

Figure 3.13: These plots show a variety of parameter choices where the behavior of Virasoro blocks on the timescale e^S (green vertical line), and even e^{e^S} (blue vertical line), are visible. Yellow lines indicate semiclassical behavior, while the light blue fit corresponds to $t^{-\frac{3}{2}}$. Recall $S = \frac{\pi^2}{3} c T_H$ with $2\pi T_H = \sqrt{\frac{24 h_H}{c} - 1}$, so some plots have relatively large c and small T_H, while others have order one T_H but small c. In all cases we see that the $t^{-\frac{3}{2}}$ late-time decay persists on these exponentially long timescales. These plots all display vacuum blocks, but we have found similar behavior with $h > 0$.

of parameter space, the $t^{-\frac{3}{2}}$ decay translates to a power law growth of the coefficients in the q expansion.

To see this, we note that at late times q approaches 1 with a rate given by (3.2.7). This implies that $\theta_3(q) \sim \sqrt{t}$, which means that the prefactor in (3.2.4) behaves like $t^{\frac{1}{2}\left(\frac{c-1}{2} - 8(h_H + h_L)\right)}$ at late times. In order to have the entire block decay as $t^{-\frac{3}{2}}$, the polynomial part $H(c, h, h_L, h_H, q)$ must cancel all c and h_i

dependence in the prefactor. This means:

$$H(t) = \sum_{n=0}^{\infty} c_n q(t)^{2n} \sim t^{4\left((h_H+h_L)-\frac{c}{16}-\frac{5}{16}\right)} \tag{3.3.7}$$

A power law in the late time behavior of the H can be directly related to the large order behavior of the q-expansion coefficients c_n. We find that $c_n \sim n^s$ with

$$s = 4\left(h_H + h_L - \frac{c}{16} - \frac{9}{16}\right) \tag{3.3.8}$$

where s is the dominant power of the coefficient growth, and we are assuming that $H(t)$ does grow at large t, which roughly requires $h_H > \frac{c}{16}$. Examples of this behavior are shown in figure 3.14. If $H(t)$ decays at late times, then there must be cancellations in the sum over q^n, and we cannot predict such a simple power-law.

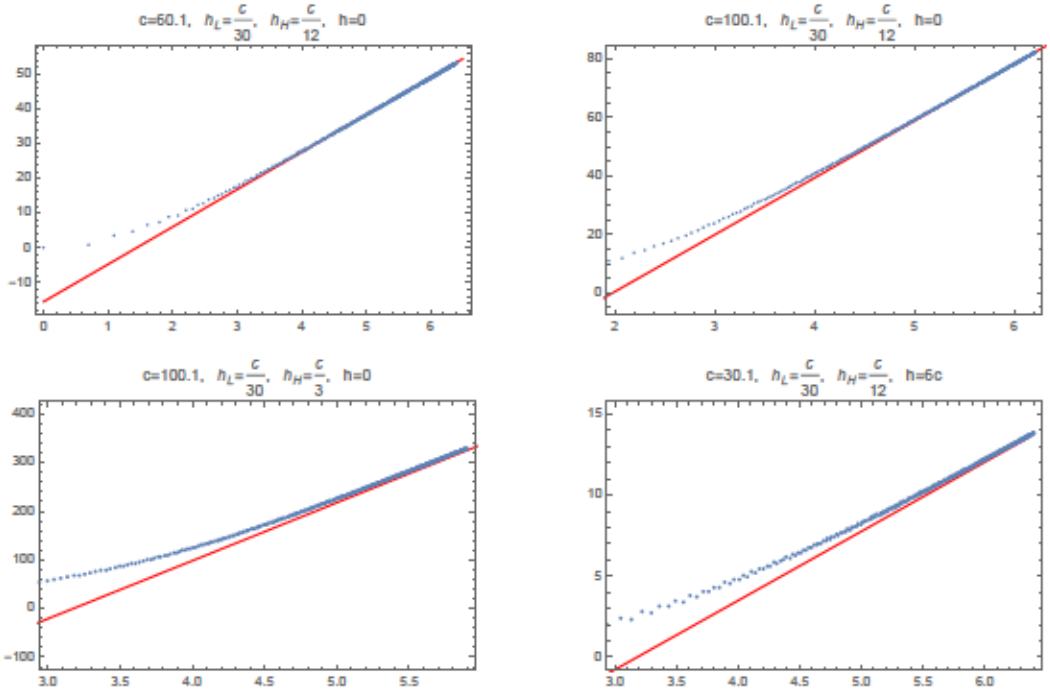

Figure 3.14: The behavior of the coefficients of the q^{2n} term in the polynomial H in (3.2.4) compared to the prediction (3.3.8). The horizontal axis is $\log n$ and the vertical axis is $\log c_n$, where c_n is the coefficient of q^{2n} in H. The red lines are power-laws an^s with the constant a determined by the fit.

So in addition to directly computing the late time values of the Virasoro blocks, we can test whether the blocks follow the $t^{-\frac{3}{2}}$ decay simply by comparing the coefficients of the q-expansion of H to the prediction (3.3.8). This is actually a more efficient method that allows us to access certain regimes, such as larger c and h_H of the parameter space where the direct Virasoro block calculation converges poorly.

However, the prediction (3.3.8) is less universal than the $t^{-\frac{3}{2}}$ behavior. For example, outside the regime where $H(t)$ grows, the coefficients c_n can have alternating signs, so that there are large cancellations between different

terms in the q-expansion. Then the magnitude of the coefficients will no-longer follow the simple pattern depicted in figure 3.3.8. Empirically, another example is when $\frac{h_L}{c}$ is small. In this case the coefficients are pretty small and show complicated irregular behaviors. Examples can be see in figure 3.23 in the appendix. Yet in all cases the overall late time behavior of the heavy-light Virasoro blocks is still the $t^{-\frac{3}{2}}$ power law.

One would hope to derive the power-law behavior $c_n \sim n^s$ using the Zamolodchikov recursion relations. Unfortunately, it appears that this behavior arises from a large number of cancellations between much larger terms. Thus we leave this problem to future work.

3.3.3 Implications for Information Loss and the Bootstrap

In the semiclassical limit, heavy-light Virasoro blocks decay exponentially at late times. We do not expect that perturbative corrections in $G_N = \frac{3}{2c}$ will alter this conclusion, and to first order this has been demonstrated explicitly [12]. Thus the late time power-law behavior of the exact blocks represents a non-perturbative correction that ameliorates information loss (insofar as information loss is tantamount to late-time decay). However, since the Virasoro blocks continue to decay, albeit much more slowly, this effect does not solve the information loss problem. For this we need an infinite sum over Virasoro blocks in the $\mathcal{O}_L\mathcal{O}_L$ OPE channel.[5]

Let us examine the correlator as a sum over blocks from the point of view

[5]Of course we are assuming that we are dealing with a chaotic large c theory, rather than e.g. a rational CFT. For special values of the external dimensions and c, such as those corresponding to degenerate external operators, the individual Virasoro blocks may not decay at late times.

of the bootstrap equation [57–59]. This equation dictates that[6]

$$\langle \mathcal{O}_H(\infty)\mathcal{O}_L(t)\mathcal{O}_L(0)\mathcal{O}_H(-\infty)\rangle = \sum_E \lambda_{LH}^2(E)e^{iEt} = \sum_{h,\bar{h}} P_{h,\bar{h}}\mathcal{V}_h(t)\bar{\mathcal{V}}_{\bar{h}}(t) \quad (3.3.9)$$

Here we have equated a sum over energies in the $\mathcal{O}_H\mathcal{O}_L$ OPE channel with a sum over heavy-light Virasoro blocks in the $\mathcal{O}_L\mathcal{O}_L$ OPE channel. In $d > 2$ dimensions this equation would be meaningless at large t, because we would be well outside the regime of convergence of the OPE expansion on the right-hand side. Remarkably, as discussed in section 3.2.1, the Virasoro block decomposition converges for all values of t, so it is possible to try to 'solve' for the coefficients $P_{h,\bar{h}}$ by equating the large t behavior of both sides. More generally, one could take the limit $|q| \to 1$ with various phases for q and derive new, potentially analytic regimes for the bootstrap (this is non-trivial because it could enable a partial analytic treatment without requiring a complete solution to the bootstrap equation). The only obvious obstruction to this procedure is that we do not have simple analytic formulas for the Virasoro blocks in such limits.

As we have already noted, equation (3.3.9) can only be satisfied at late times if we have an infinite number of Virasoro blocks contributing on the right-hand side. Such infinite sums are compulsary in order to reproduce conventional OPE limits [31–34]. But it is easy to see that the Cardy formula and the asymptotic expectations on $P_{h,\bar{h}}$ from Euclidean crossing or the light-cone OPE limit are insufficient to account for the late-time behavior. The

[6] We are being schematic to emphasize the time dependence. One should define $z = 1 - e^{-t+i\phi}$ and $\bar{z} = 1 - e^{-t-i\phi}$ in the Euclidean region, and then analytically continue $t \to it$, so that both channels depend on the coordinates t and ϕ pictured in figure 3.1. We are suppressing these details.

reason is that conventional arguments require the large $h, \bar{h}$ terms in equation (3.3.9) to reproduce either the identity (vacuum) or perhaps the contribution of low dimension or low twist operators in the crossed channel. These would correspond to the very small E region of $\lambda_{LH}(E)$. But the late time behavior arises from the collective contributions of $\sim e^S$ states with large $E \sim h_H + \bar{h}_H$, not from the small E states.[7]

In this regard there is an amusing connection with Maldacena's original discussion [28] of the large time behavior. He suggested that in a black hole background, contributions from the vacuum, corresponding to the $E = 0$ term in equation (3.3.9), might resolve the information loss problem. But the vacuum in the $\mathcal{O}_H \mathcal{O}_L$ OPE channel just corresponds with the Cardy-type growth (or more precisely OPE convergence [32] type growth) of $P_{h,\bar{h}}$. So this simple OPE convergence growth fails to account for the late time behavior for the same reason that Maldacena's suggestion did not resolve the information loss problem.

In summary, the late-time bootstrap equation (3.3.9) cannot be solved without providing a more refined asymptotic formula for $P_{h,\bar{h}}$ at large $h, \bar{h}$. However, it does not appear that a discrete spectrum in the $\mathcal{O}_L \mathcal{O}_L$ channel is required to obtain the correct late-time behavior. We will not pursue this in detail since we only have some rough empirical information about the behavior of $\mathcal{V}_h(t)$, but it might be interesting to study this bootstrap equation for the case of the partition function [51] where the Virasoro characters are

[7] Here we are imagining subtracting off the contributions from the expectation values $\langle \mathcal{O}_H | \mathcal{O}_L | \mathcal{O}_H \rangle$. These are generically expected to be exponentially suppressed [60] in holographic CFT_2.

known in closed form.

3.4 Euclidean Breakdown of the Semiclassical Approximation

3.4.1 Some Philosophy

Eventually, we hope to learn about bulk reconstruction – and its limitations – by comparing exact CFT correlators to their semiclassical approximations. It is not clear whether this is possible, even in principle, due to ambiguities in the reconstruction process associated with bulk gauge redundancies (see e.g. [61] for a recent discussion). For now we will take a very instrumental approach, or in other words, we will try to 'shut up and calculate' some potentially interesting observables.

The information paradox pits local bulk effective field theory in the vicinity of a horizon against quantum mechanical unitarity. But in the strict semiclassical limit, information is lost and the (approximate) CFT correlators agree precisely with perturbative AdS field theory or string theory. Thus one would expect that bulk reconstruction should be possible in this approximation, since we have allowed the local bulk theory to 'win' the fight, at the expense of unitarity.[8]

[8]This suggests that solving the reconstruction problem in the strict semiclassical limit should not have much to do with the information paradox or the existence of firewalls [62], except insofar as it is a first step towards the problem of bulk reconstruction from the data and observables of the exact CFT. As an alternative perspective, one might claim that even in the semiclassical limit reconstructing black hole interiors is impossible because firewalls are completely generic.

But even in the semiclassical limit, bulk reconstruction has been controversial [36–39]. On an intuitive level, this is because correlators at infinity must have exponential sensitivity to 'observe' physics near or behind a black hole horizon. At an instrumental level, this means that there may be obstructions to the existence of smearing functions mapping boundary to bulk observables. These issues can be avoided by going to momentum space [40, 41], or perhaps via an appropriate analytic continuation [36] or cutoff procedure [39].

Another elementary issue with semiclassical bulk reconstruction is pictured in figure 3.2. The problem is that only the ingoing modes behind the horizon can be reconstructed in an obvious way from the degrees of freedom of a single CFT [36]. This can be understood by considering the extended AdS-Schwarzschild spacetime, or simply by studying Rindler space. Field theory degrees of freedom behind the horizon appear as a linear combination of modes from the left and right 'wedges', but in a single-sided black hole, only one asymptotic region is present.

If the goal is simply to compute correlators behind the horizon of a single-sided black hole, then there is a naive, instrumental way to obtain outgoing modes. One can obtain correlators that behave like those of the other asymptotic region by analytically continuing [36] CFT operators $\mathcal{O}(t,x)$ in Euclidean time to $\tilde{\mathcal{O}}(t,x) \equiv \mathcal{O}\left(t+\frac{i\beta}{2},x\right)$. This procedure has an important flaw – operators on opposite sides of the black hole should commute, but $\mathcal{O}$ and $\tilde{\mathcal{O}}$ may not. Nevertheless, we can force $\mathcal{O}$ and $\tilde{\mathcal{O}}$ to commute (by definition) if we choose an appropriate but ad hoc analytic continuation procedure for correlators involving $\mathcal{O}$ and $\tilde{\mathcal{O}}$. Conceptually, this does not seem to be an

improvement on state-dependent mirror operators [40, 41], which represent a modification of quantum mechanics. In fact, our procedure implements its own form of state-dependence, since the analytic continuations will depend on all of the other local operators inserted into the correlator. However, the prescription does have the simple advantage of being relatively precise and unambiguous.

In any case, we are led to a very simple question – do the correlators of operators like $\mathcal{O}\left(t+\frac{i\beta}{2},x\right)$ receive large non-perturbative corrections? Do the semiclassical Virasoro blocks provide a good approximation to the exact blocks with these kinematics?

3.4.2 Forbidden Singularities and Thermofield Doubles

The questions raised in the previous section can be explored using the methods of this paper. They are also closely related to observations about information loss [15]. Finite-temperature correlation functions must satisfy the KMS condition, which for identical operators just means that $\langle\mathcal{O}(t,x)\mathcal{O}(0)\rangle_\beta$ must be periodic in Euclidean time with period β. It has been shown that in the large central charge limit with $h_H > \frac{c}{24}$, heavy-light Virasoro blocks appear thermal.[9] Since the 4-point correlator has an OPE singularity

$$\langle\mathcal{O}_H(0)\mathcal{O}_L(z)\mathcal{O}_L(1)\mathcal{O}_H(\infty)\rangle = \frac{1}{(1-z)^{2h_L}} + \cdots \tag{3.4.1}$$

[9]The vacuum block is exactly periodic. The general case in equation (3.2.10) would be periodic except for the branch cuts of the hypergeometric function, but these do not obstruct the KMS condition for the full correlator, and are compatible with the Virasoro block decomposition of correlators obtained from BTZ black hole backgrounds [10].

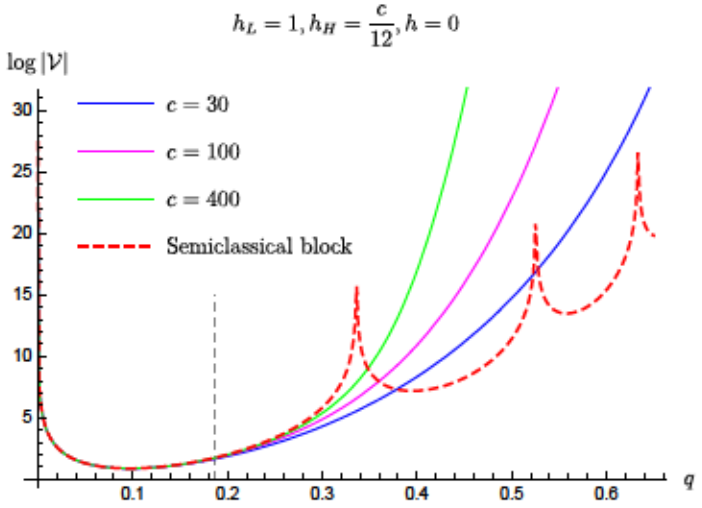

Figure 3.15: In this plot, we compare the exact and semiclassical blocks. One can see that at the positions of the semiclassical forbidden singularities, the exact blocks are smooth. Fixing h_L and $\frac{h_H}{c}$ as we increase c, the exact blocks approach the semiclassical block in the region between the origin and the first forbidden singularity. However, beyond the first forbidden singularity the exact blocks deviate greatly as we increase c. This indicates that we have passed a Stokes line (emanating from the forbidden singularity) and some other semiclassical saddle dominates the exact blocks in the large c limit. The gray line is the position of $t = \frac{i\beta}{2}$.

as $z \to 1$, in the heavy-light semiclassical limit, it will also have singularities at $z_n = 1 - e^{n\beta}$ for all integers n.

While such singularities are permissible for correlators in the canonical ensemble, they are forbidden [15, 35] from 4-point correlators of local operators in unitary CFTs. They are also forbidden from individual Virasoro blocks at finite central charge [13, 15]. Thus exact Virasoro blocks completely disagree with their semiclassical counterparts at $z_n = 1 - e^{n\beta}$, the locations of the singularities. So to summarize, we know that the exact and semiclassical blocks match at $z = 0$, and completely disagree at $z = 1 - e^{n\beta}$ for $n \neq 0$. Thus it is natural to wonder whether the semiclassical blocks are a good approximation at $z = 1 - e^{-\frac{\beta}{2} - it}$, which corresponds to the location of $\mathcal{O}(t +$

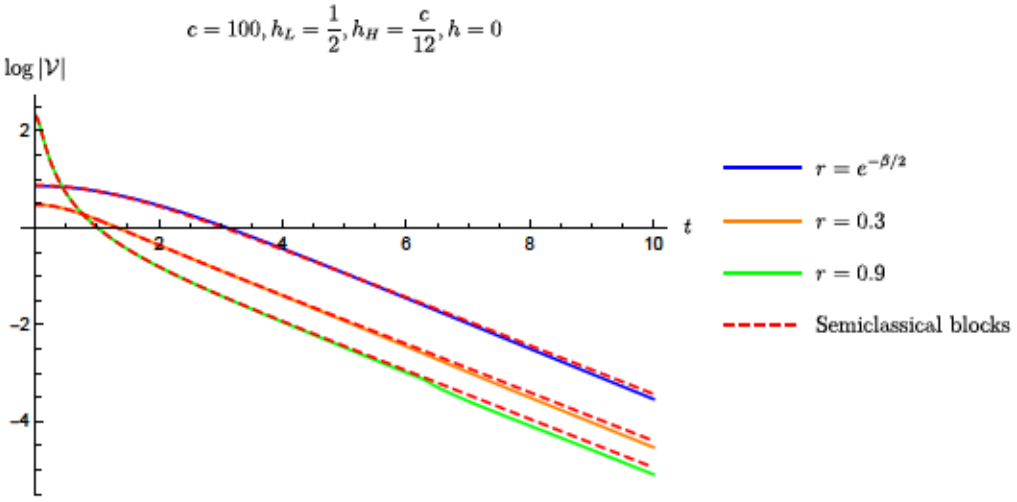

Figure 3.16: In this figure we compare the semiclassical and exact blocks associated with $\mathcal{O}(t)$ and $\mathcal{O}(t + \frac{i\beta}{2})$. The plot suggests that the semiclassical approximation remains valid for correlators of $\mathcal{O}(t + \frac{i\beta}{2})$. We implement time dependence via $z = 1 - re^{-it}$ and so a shift by $\frac{i\beta}{2}$ simply corresponds to a different choice of r. Corresponding trajectories in the unit q disk are pictured in figure 3.6. Apparently the semiclassical approximation works well at $t + \frac{i\beta}{2}$.

$\frac{i\beta}{2}$). More generally we would like to understand the kinematical regimes where the (leading) semiclassical approximation breaks down.

We observe from figure 3.15 that as expected, the exact Virasoro blocks do not have forbidden singularities. Nevertheless one might have expected to see bumps or local maxima at $z_n = 1 - e^{n\beta}$, whereas the exact correlator simply grows as a function of $z \in [0, 1)$. In fact local maxima are prohibited because the exact blocks are analytic functions of q and z away from the true OPE singularities.[10] Thus the semiclassical approximation breaks down badly

[10]Moreover it is not too surprising that a finite series expansion of the exact blocks simply grows in the region where the semiclassical blocks have forbidden singularities. For example, the finite-order series expansion of a function like $\frac{1}{(1-x)^2(2-x)^2}$ will grow monotonically on the positive real x-axis; one can only see the correct behavior on $x \in (1, 2)$ by summing the full series and analytically continuing around $x = 1$.

beyond the first forbidden singularity.

We compare the exact and semiclassical blocks at finite time in figure 3.16. We see that the semiclassical blocks remain a good approximation to correlators of $\mathcal{O}(t + \frac{i\beta}{2})$ as long as we avoid the long-time region of $t \propto S$ that was discussed in section 3.3. In particular, there is not a significant difference between the quality of the semiclassical approximation to correlators of $\mathcal{O}(t + \frac{i\beta}{2})$ and $\mathcal{O}(t)$. The most naive interpretation of this fact is that non-perturbative quantum gravitational effects do not obstruct local physics across the horizon of pure, energy-eigenstate black holes. A qualitatively similar conclusion was reached for late-time deviations [63] from the semiclassical limit. This result was also anticipated by the analytic analysis of [15], which only suggested large non-perturbative corrections within $\frac{1}{\sqrt{c}}$ of the forbidden singularites. In the next section we will discuss that analysis and compare it with our numerical results.

3.4.3 Fate of the Semiclassical Approximation from Analytics and Numerics

We do not have to rely entirely on numerics to explore the regime of validity of the semiclassical limit. It has been shown that the vacuum block's forbidden singularities have a universal resolution due to non-perturbative effects in central charge. Specifically, the heavy-light vacuum block (with h_L and $\frac{h_H}{c}$ held fixed at large c) should obey an approximate differential equation [15]

$$h_L g_H(\tau)\frac{\mathcal{V}(\tau)}{\mathcal{V}'(\tau)} - 1 \quad = \quad \frac{6}{c}\Sigma_H(\tau)\frac{\mathcal{V}''(\tau)}{\mathcal{V}'(\tau)} \tag{3.4.2}$$

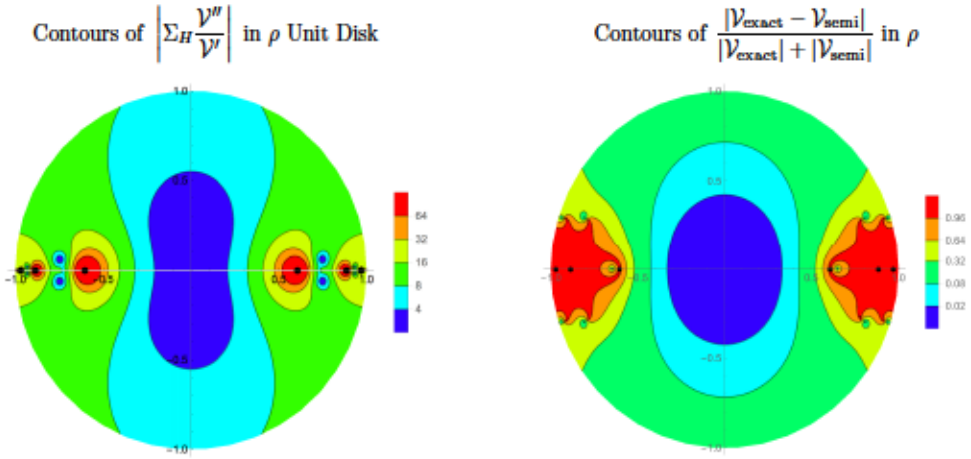

Figure 3.17: The figure on the left shows a contour plot of the function $|\Sigma_H \frac{\mathcal{V}''}{\mathcal{V}'}|$ from equation (3.4.2) in the ρ unit disk with $h_L = 1$ and $h_H = \frac{c}{4}$. The figure on the right is the deviation of the exact and semiclassical Virasoro vacuum blocks with the same parameters and $c = 60$. The positions of the forbidden singularities are indicated with black dots. The plot on the left can be viewed as a kind of analytic prediction for the deviation plotted on the right.

where $\tau = -\log(1-z)$ is a Euclidean time variable, and this equation neglects terms of order $1/c^2$ and higher as well as effects that are less singular near the forbidden singularities. We provide the functions g_H and Σ_H in appendix 3.B.1. This differential equation also predicts [15] that the semiclassical vacuum block will receive large non-perturbative corrections after a Lorentzian time of order $\frac{S_{BH}}{h_L T_H} \propto \frac{c}{h_L}$. That prediction was corroborated in section 3.3.

Neglecting the term proportional to $\frac{1}{c}$ on the right-hand side, equation (3.4.2) is solved by the semiclassical heavy-light vacuum block. But when the right-hand side of this equation becomes large, non-perturbative effects come into play, resolving the forbidden singularities. We plot contours of the function $|\Sigma_H \frac{\mathcal{V}''}{\mathcal{V}'}|$ for $h_L = 1$ in figure 3.17. We see that this function becomes large and makes important contributions in the immediate vicinity of the forbidden singularities, though at sufficiently large c the right-hand

side of equation (3.4.2) will remain small a finite distance away from these singularities. At a more detailed level, the function $|\Sigma_H \frac{\mathcal{V}''}{\mathcal{V}'}|$ can be compared directly to the deviation of the numerical and semiclassical vacuum block. We plot contours of the ratio of the exact and semiclassical blocks in the ρ unit disk, corresponding to the entire Euclidean z-plane in figure 3.17 (recall that we compared various kinematic variables in figures 3.3 and 3.4).

Our numerical results demonstrate that the semiclassical approximation breaks down in a finite region enclosing the forbidden singularities. We believe this phenomenon occurs because Stokes and anti-Stokes lines (for review see e.g. [64]) emanate from the forbidden singularities, as has been demonstrated for the correlators of degenerate operators [15]. As we cross Stokes lines, the coefficients of semiclassical saddles change by discrete jumps. Across anti-Stokes lines saddles exchange dominance.

Near the OPE configuration $z \propto \rho \propto q \approx 0$ where the light operators collide, a special 'original' semiclassical saddle dominates the large c limit [15] of the Virasoro blocks. But in a finite region near the forbidden singularities, different semiclassical saddles [13] can come to dominate, and the original saddle may become sub-leading. In other words, analytic continuation in the kinematic variables does not commute with the large c limit. Non-perturbative effects can dramatically alter the behavior of CFT_2 correlation functions with these kinematics, supplanting the naive semiclassical limit and the perturbation expansion around it.

It would be fascinating if the black hole interior depends in some way on the behavior of CFT correlation functions in these regimes. Note that when

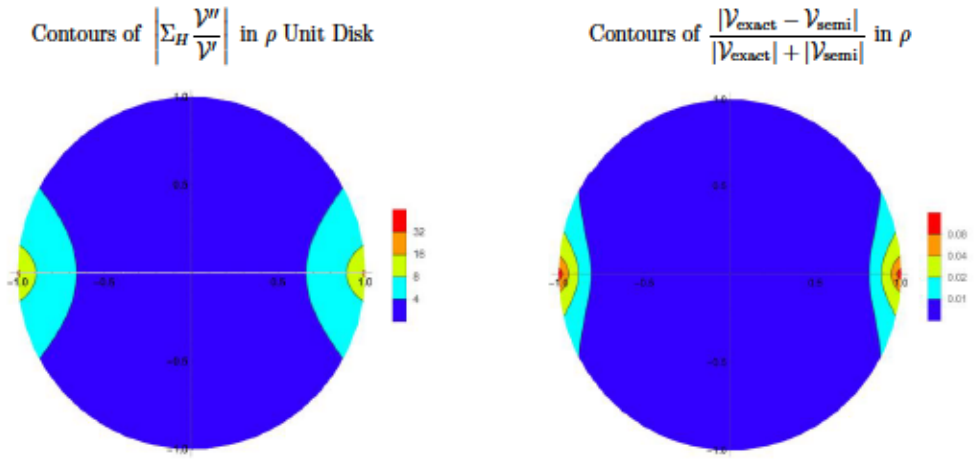

Figure 3.18: The figure on the left shows a contour plot of the function $|\Sigma_H \frac{\mathcal{V}''}{\mathcal{V}'}|$ from equation (3.4.2) in the ρ unit disk with $h_L = 1$ and $h_H = \frac{c}{30}$. In this case $h_H < \frac{c}{24}$, so the heavy-light block does not include a black hole – instead it corresponds to a light probe interacting with a deficit angle in AdS_3. Thus there are no forbidden singularities, and the semiclasssical approximation is reliable in a much larger region as compared to figure 3.17 (note the difference in scales). The figure on the right is the deviation of the exact and semiclassical Virasoro vacuum blocks with the same parameters and $c = 60$. The plot on the left can be viewed as a kind of analytic prediction for the deviation plotted on the right.

$h_H < \frac{c}{24}$, so that the heavy background state does not correspond to a black hole, the original semiclassical approximation remains good throughout the Euclidean region. We demonstrate this explicitly in figure 3.18. So the breakdown of the semiclassical limit exhibited in figure 3.17 really does depend on the presence of a black hole, and is not a general feature of all Virasoro blocks at large central charge.

3.5 Discussion

We would eventually like to resolve the black hole information paradox by doing the right calculation. In the context of AdS/CFT, this means discerning under what circumstances, if any, bulk reconstruction is possible near and behind black hole horizons.

If firewalls [62] are completely generic, or if bulk reconstruction is sufficiently ambiguous, then this could be a fools errand. But even in this case, one can still hope for a more constructive argument rather than various reductio ad absurdums [42]. For example, one would like to reconstruct the 'experience' of a collapsing spherical shell, and explicitly compute the timescale beyond which subsequent infallers will not see a smooth (or well-defined) geometry.

But let us imagine that the strict semiclassical limit is not misleading and black holes often have smooth interiors. In this case, violations of bulk locality should arise from the difference between computations in the semiclassical limit and the exact CFT observables (or perhaps meta-observables). This sort of approach has already been successfully pursued in the context of local bulk scattering [35]. We have identified gross differences between exact and

semiclassical CFT correlators in both the late Lorentzian time and the Euclidean regime. These do not seem to affect a certain naive bulk reconstruction algorithm, but perhaps they do afflict more sophisticated methods yet to be developed. Hopefully we have done some of the right calculations but do not yet know how to give them the right interpretation. In the case of quantum mechanics and QFT, we were in that sort of boat for decades.

Appendix

3.A Details of Recursion Relations and Our Algorithm

In this appendix we will present more details about Zamolodchikov's recursion relations and the algorithm we used to compute with them.

3.A.1 Zamolodchikov's Recursion Relations

There are actually two Zamolodchikov recursion relations, based on viewing the Virasoro blocks as either a sum over poles in the central charge c or the intermediate state dimension h. The latter is more powerful and will be our focus.

The Virasoro block of the four-point function $\langle \mathcal{O}_1(0)\mathcal{O}_2(z)\mathcal{O}_3(1)\mathcal{O}_4(\infty)\rangle$ with central charge c, external dimensions h_i and intermediate dimension h takes the following form

$$\mathcal{V}_{h,h_i,c}(z) = (16q)^{h-\frac{c-1}{24}} z^{\frac{c-1}{24}-h_1-h_2} (1-z)^{\frac{c-1}{24}-h_2-h_3} [\theta_3(q)]^{\frac{c-1}{2}-4\sum_{i=1}^4 h_i} H(c,h_i,h,q), \tag{3.A.1}$$

where

$$q = e^{i\pi\tau}, \ \ \tau = i\frac{K(1-z)}{K(z)}, \tag{3.A.2}$$

and the inverse transformations is

$$z = \left(\frac{\theta_2(q)}{\theta_3(q)}\right)^4. \tag{3.A.3}$$

If we parametrize the central charge c, the external operator dimensions h_i and the degenerate operator dimensions h_{mn} as follows

$$c = 13 + 6\left(b^2 + \frac{1}{b^2}\right), \quad h_i = \frac{1}{4}\left(b + \frac{1}{b}\right)^2 - \lambda_i^2, \quad h_{m,n} = \frac{1}{4}\left(b + \frac{1}{b}\right)^2 - \lambda_{m,n}^2, \tag{3.A.4}$$

with

$$\lambda_{m,n} = \frac{1}{2}\left(\frac{m}{b} + nb\right), \tag{3.A.5}$$

then the function $H(b, h_i, h, q)$ can be calculated using the following recursion realtion

$$H(b, h_i, h, q) = 1 + \sum_{m,n\geq 1} \frac{q^{mn} R_{m,n}}{h - h_{m,n}} H(b, h_i, h_{m,n} + mn, q), \tag{3.A.6}$$

where $R_{m,n}$ is given by

$$R_{m,n} = 2\frac{\prod_{p,q}\left(\lambda_1 + \lambda_2 - \lambda_{p,q}\right)\left(\lambda_1 - \lambda_2 - \lambda_{p,q}\right)\left(\lambda_3 + \lambda_4 - \lambda_{p,q}\right)\left(\lambda_3 - \lambda_4 - \lambda_{p,q}\right)}{\prod'_{k,l}\lambda_{k,l}}, \tag{3.A.7}$$

and the ranges of p, q, k, and l are:

$$p = -m+1, -m+3, \cdots, m-3, m-1,$$

$$q = -n+1, -n+3, \cdots, n-3, n-1,$$

$$k = -m+1, -m+2, \cdots, m,$$

$$l = -n+1, -n+2, \cdots, n.$$

The prime on the product in the denominator means that $(k,l) = (0,0)$ and $(k,l) = (m,n)$ are excluded. Note that our definition of $\lambda_{p,q}$ differs by a factor of $-\frac{i}{2}$ from the original paper.

In each iteration of the recursion relation 3.A.6, the only thing that changes is the value of the intermediate state dimension $h \to h_{m,n} + mn$, which only depends on the values of m and n. For simplicity we'll omit the arguments and denote $H(b, h_i, h, q)$ as H and $H(b, h_{m,n} + mn, h_i, q)$ as $H_{m,n}$ in the following discussion.

This recursion relation was derived by viewing the Virasoro block $\mathcal{V}_h$ as a function of the intermediate dimension h, so it can be written as a remainder term that survives when $h \to \infty$ plus a sum over poles at $h = h_{m,n}$, where $h_{m,n}$ are the dimensions of the degenerate operators. The prefactor in front of H in 3.A.1 is the $h \to \infty$ limit of $\mathcal{V}_h$, as can be derived from [24–26]. The reason that $\mathcal{V}_h$ has poles at $h = h_{m,n}$ is because of the existence of the null-operator (whose norm is zero) at level mn of the descendants of $\mathcal{O}_{h_{m,n}}$, which usually will make $\mathcal{V}_h$ diverge when $h \to h_{m,n}$.[11] The residue of the pole at $h_{m,n}$ will be proportional to the block $\mathcal{V}_{h_{m,n}+mn}$ with intermediate operator being the null-operator with dimension $h_{m,n} + mn$. Thus, these residues will have high powers of q, which accounts for the q^{mn} factor in front of $H_{m,n}$ and naturally makes the Virasoro block $\mathcal{V}_h$ a series expansion in q.

The numerator of the factor $R_{m,n}$ is constructed such that it vanishes when $\mathcal{O}_1$ (or $\mathcal{O}_3$) belongs to the set of operators allowed by the fusion rule of $\mathcal{O}_2\mathcal{O}_{h_{m,n}}$

[11] This is easy to see by writing $\mathcal{V}_h$ as a sum over contributions from the states in the Verma Module of $\mathcal{O}_h$. In this sum, we need to orthogonalize the states, but the zero norm of the null-state will appear as a denominator in this process, which causes the divergence.

(or $\mathcal{O}_4\mathcal{O}_{h_{m,n}}$). The denominator of $R_{m,n}$ comes from the norm of the null-state when $h \to h_{m,n}$ (factoring out $h - h_{m,n}$); as far as we know, although it has passed numerous checks, it's never been derived from first principles.

3.A.2 Algorithm

In this paper, we only consider the case that $h_1 = h_2 = h_L$ and $h_3 = h_4 = h_H$. Under this circumstance, $R_{m,n}$ becomes directly proportional to $\lambda_{p,q}^2$, so $R_{m,n} = 0$ whenever (m, n) are both odd, because (p, q) can then be $(0, 0)$. This means that every $H_{m,n}$ with odd mn is also zero, as every term contributing to it contains at least one R_{m_l,n_l} with odd $m_l n_l$. As a consequence of this, only even powers of q ever appear, and there's no need to compute anything with odd mn. This provides some simplification for the calculation, but it's easy to generalize the following discussion to the case that all h_is are different.

Now we turn to the algorithm we used to compute the recursion relation. The main idea is to sort every contribution to the functions H and $H_{m,n}$ by its order in q. By doing this from the beginning of the computation, we are able to use lower-level terms as partial sums for the higher-level terms, saving a great deal of computation.

Denote the coefficient of q^k in any function f as $f^{(k)}$. Then the recursion relation for the coefficients of q^k in the function H is

$$H^{(k)} = \sum_{i=2}^{k} \sum_{\substack{l=1 \\ m_l n_l = i}}^{\mathrm{div}(i)} \frac{R_{m_l,n_l}}{h - h_{m_l,n_l}} H_{m_l,n_l}^{(k-i)}, \tag{3.A.8}$$

where in the first sum i runs over even integers (odd terms will always be zero, as explained at the beginning of this section) and the second sum counts

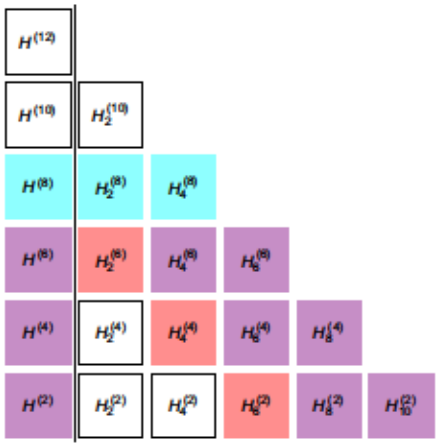

Figure 3.19: This figure shows a half-completed computation with max order q^{12}; each cell $H_i^{(k)}$ represents 2 to 4 distinct terms $H_{m_l n_l}^{(k)}$ with $m_l n_l = i$. The cyan row, order q^8, is currently being computed, and the red diagonal contains the terms which are being used in the computation of the cyan row. The purple cells have already been computed and are being stored for future use, and the white cells have not been computed yet or have been deleted to save RAM. The row with $k = 0$ (which would be at the bottom) contains the seed terms $H^{(0)} = H_{m,n}^{(0)} = 1$ and is not shown.

the ways to write i as the product of two integers m_l and n_l, so l runs from 1 to the number of divisors of i, which we denote as $\mathrm{div}(i)$. For large i, $\mathrm{div}(i)$ is roughly of order $\sim \log i$. Similarly, for the coefficients $H_{m,n}^{(i)}$ of q^i in $H_{m,n}$, we have

$$H_{m,n}^{(k)} = \sum_{i=2}^{k} \sum_{\substack{l=1 \\ m_l n_l = i}}^{\mathrm{div}(i)} \frac{R_{m_l,n_l}}{h_{m,n} + mn - h_{m_l,n_l}} H_{m_l,n_l}^{(k-i)}. \tag{3.A.9}$$

Notice that in the above two equations, $H^{(k)}$ and $H_{m,n}^{(k)}$ only depend on lower order terms $H_{m_l,n_l}^{(k-i)}$ for which $(k-i) + m_l n_l = k$. As illustrated in Figure 3.19, we can perform the calculation from lower rows (small k) to upper rows (large k). In this way, when calculating $H_{m,n}^{(k)}$, all the $H_{m_l,n_l}^{(k-i)}$s are known already (and they are in the diagonal positions, which suggests to store them

in diagonals), and there are only $\sim k \log k$ such terms, so the time complexity is only roughly $O\left(N^3 (\log N)^2\right)$. This is better than the literal implementation of the recursion relation (getting the coefficients $H^{(k)}$ by directly recursing down to $H^{(0)}_{m_l,n_l}$), which seems to have a complexity of $O(e^N)$.

There are several other tricks that one can do to even speed up the calculation. For example, one can precompute all of the residue prefactors $\frac{R_{p,q}}{h_{m,n}+mn-h_{p,q}} \equiv C_{m,n,p,q}$ in 3.A.9. There are only $O(N\,(\log N)^2)$ of these, so we can save time by computing them in advance and reusing them. Although precomputation dramatically improves performance, it also doubles memory consumption; but since we store the $H^{(i)}_{m,n}$ in diagonals, this can be ameliorated by deleting them after they're used, as shown in 3.19.

Precomputing $C_{m,n,p,q}$ can only improve overall speed if each of its terms can be computed in constant time. This is potentially problematic, since $R_{p,q}$ contains two products of $O(pq)$ complexity, but it can be solved by filling $R_{p,q}$ recursively – $R_{p,q}$ can be computed in $O(p)$ time from $R_{p,q-2}$, and there are only $O(N \log N)$ of them, so the computational complexity of filling all $R_{p,q}$ is just $O(N^2 \log N)$. These can be further sped up by pairing up terms to rewrite all of the defining equations in terms of b^2 and $\lambda^2_{m,n}$ instead of b and $\lambda_{m,n}$. In addition to the reduced number of multiplications, this also allows the entire computation to be done using real numbers when $c > 25$, which is generally an order of magnitude faster. When $c < 25$, b^2 becomes complex, and even though the final coefficients must be real by unitarity, this only occurs at the very last step in the form of a $b^2 \leftrightarrow \frac{1}{b^2} = (b^2)^*$ symmetry.

We have implemented this algorithm in both Mathematica and C++(with

Mathematica integration). The Mathematica notebook is included as a companion to this paper, while the C++ implementation is maintained at https://github.com/chussong/virasoro. The C++ implementation is about one order of magnitude faster, and the coefficients used in this paper were obtained using it. The C++ implementation has used the GMP [65], MPFR [66], MPC [67], and MPFR C++ [68] numerical libraries. On standard personal computers we were able to compute the $H^{(k)}$ to $k = 1000$ in around two minutes or $k = 2000$ in about 22 minutes (for $c > 25$ so that b is real); the main barrier to going higher is memory consumption, which grows roughly as $N^3 \log N$: we need to remember $O(N^2 \log N)$ numbers and they need to be kept at $O(N)$ bits of precision due to the increasingly large cancellations between different $H_{m,n}$, which often reach into the thousands of binary orders of magnitude.

Using a cluster with 128 GB of RAM, we estimate that we could reach order of 6000 in a few hours. We also find that the coefficients of q^i approach a power law in i well before the limits of our desktop computation, and expect that a numerical fit for this power law would be good enough to get higher order coefficients.

At the end of this section, we want to mention an issue about the recursion relation if b^2 is a rational number. Notice that the denominator in 3.A.9 and the denominator of $R_{m,n}$ in 3.A.7 can be zero:

$$h_{m,n} + mn - h_{m_l,n_l} = 0 \quad \Rightarrow \quad b^2 = \frac{m + m_l}{n - n_l} \text{ or } \frac{m - m_l}{n + n_l} \tag{3.A.10}$$

$$\lambda_{k,l} = 0 \quad \Rightarrow \quad b^2 = -\frac{k}{l} \tag{3.A.11}$$

Both of these will eventually occur for any rational choice of b^2. This would appear to preclude numerical computation entirely (since for numerical calculation, b provided to the computer will always be rational), but actually for almost all rational numbers they will not appear until very high orders in the computation, so they can be ignored as long as the numerator or denominator of b^2 (as a irreducible fraction) is very large. In this paper, we've chose $\sqrt{c}$ to be irrational (and set b to be a very high-precision number) to avoid this problem.

3.B Technical Details and Extra Plots

3.B.1 A Non-Perturbative Differential Equation for the Vacuum Block

Here we describe the functions appearing in the differential equation (3.4.2). Note that although the equation itself is perturbative, its solution includes non-perturbative corrections to the heavy-light vacuum Virasoro block. The equation was derived [15] by studying the general differential equations satisfied by degenerate operators and then analytically continuing these equations in the integer index r labeling the degenerate operators. We should also note that although equation (3.4.2) only includes some of the first $1/c$ corrections, if one zooms in on the vicinity of the forbidden singularities by holding $\sqrt{c}(z - z_n)$ fixed at large c, then the equation incorporates all of the leading effects at large c. As discussed in [15], there are both general arguments and consistency checks on the validity of equation (3.4.2).

We identify the parameter $r = 2\pi i T_H = \sqrt{1 - \frac{24h_H}{c}}$, so that T_H is the

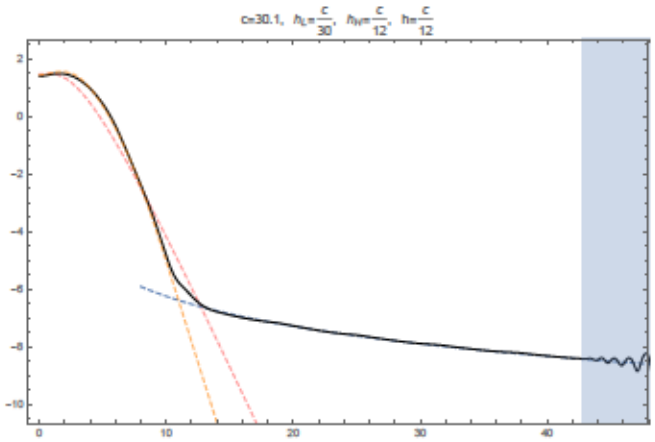

Figure 3.20: This figure corresponds to the top-right plot of figure 3.10, but includes a match to the semiclassical blocks obtained using the methods of [13], which allow for $h, h_L \propto c$. The poorly fitted dashed line is the approximation of equation (3.2.10), which assumes $h, h_L \ll c$, and clearly provides a much less reliable fit for these parameter values.

Hawking temperature associated with the heavy operator. We also are using a Euclidean time variable $\tau = -\log(1-z)$. Then the functions included in equation (3.4.2) are $g_H \equiv g_{2\pi i T_H}$ with

$$g_r(\tau) = \coth\left(\frac{\tau}{2}\right) - r\coth\left(\frac{r\tau}{2}\right) \tag{3.B.1}$$

and $\Sigma_H \equiv \Sigma_r + \Sigma_{-r}$ where we define

$$\Sigma_r(\tau) = -\frac{1}{r\sinh\left(\frac{r\tau}{2}\right)}\left(e^{-\frac{r\tau}{2}}\tilde{B}_r(\tau) + e^{\frac{r\tau}{2}}\tilde{B}_r(-\tau) - 2\cosh\left(\frac{r\tau}{2}\right)\tilde{B}_r(0)\right) \tag{3.B.2}$$

Finally, we have introduced the function $\tilde{B}_r(t)$ which can be represented as

$$\tilde{B}_r(\tau) = -\log(1-e^{\tau}) - \frac{e^{r\tau}{}_2F_1(1,r,1+r,e^{\tau})}{r} \tag{3.B.3}$$

For derivations and more complete descriptions see [15].

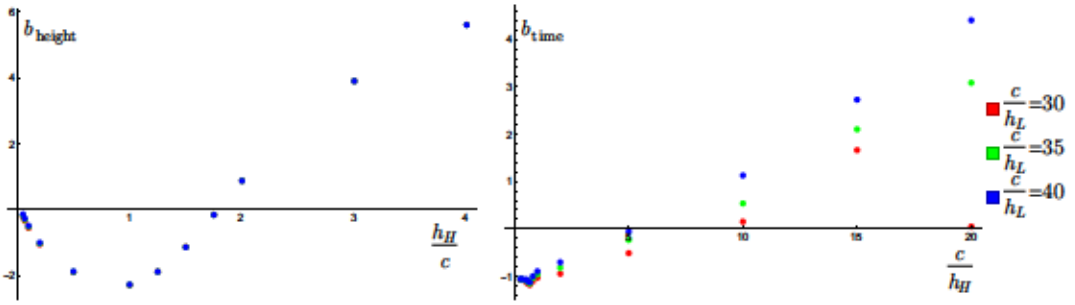

Figure 3.21: We have found empirically that the time and height of the maxima of heavy-light Virasoro blocks have a simple dependence on both h and h_H. This figure shows data on the parameters b_{height} and b_{time} defined in equations (3.3.6) and (3.3.5). These plots both have $c = 10$. Each point is obtained from linear fitting of data points at $\frac{h}{c} = \frac{n}{3}$ for $n = 1, 2, \cdots, 30$. We see explicitly that there is very little dependence on h_L, especially at large values of h_H.

3.B.2 Some Extra Plots

In this section we have included some extra plots for readers who might like to some more details and examples. These include the semiclassical fit to our numerical results for $h, h_L \propto c$ using [13] (figure 3.20), the behavior of the b_{time} and b_{height} parameters from equations (3.3.6) and (3.3.5) (figure 3.21) and a version of figure 3.12 zoomed in on the large h_H/c region (figure 3.22), which is rather compressed in that figure.

We also show some plots of the more complicated coefficient behavior which was alluded to in section 3.3.2, with the sign of the coefficients corresponding to the color of plotted points. Figure 3.23 illustrates a very common scenario where the coefficients are chaotic at low c, but as c increases they coalesce into distinct positive and negative lines. A spike-shaped feature then appears at low order and moves upward, turning the coefficients that it passes positive, until all (visible) coefficients have become positive. The two lines then gradually merge into a single power law similar to those shown in figure

3.14.

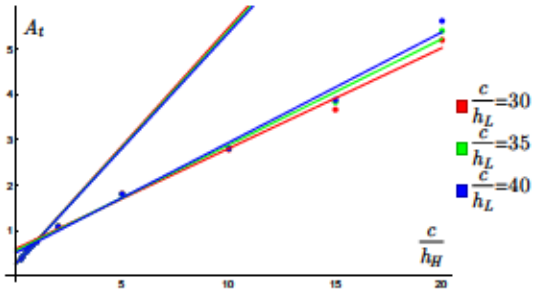

Figure 3.22: This is a version of figure 3.12 where we have zoomed out to show the small $\frac{h_H}{c}$ region. The zoomed-out points with $\frac{c}{h_L} = (30, 35, 40)$ more closely fit slopes $(0.221, 0.233, 0.242)$, which are shown as solid lines; the $(0.521, 0.515, 0.509)$ fits for large $\frac{h_H}{c}$ are shown as dotted lines.

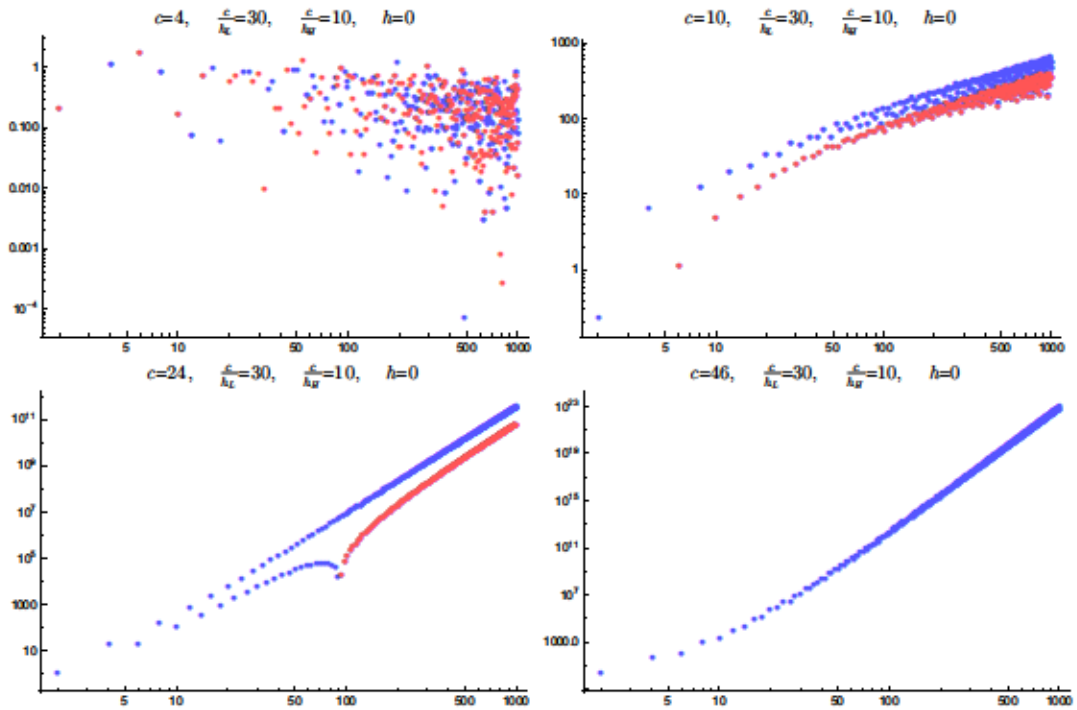

Figure 3.23: This figure shows the coefficients c_n of the q^{2n} expansion of H. We plot $|c_n|$ as a function of n, with both n and c_n on log scales, for increasing c with $\frac{h_L}{c}$ and $\frac{h_H}{c}$ held constant. The sign of the c_n are illustrated by the color of the points, with blue for positive coefficients and red for negative coefficients.

Chapter 4

RG Flow from ϕ^4 Theory to the 3D Ising Model

Adapted from a paper currently in preparation in collaboration with Nikhil Anand, Emanuel Katz, Zuhair Khandker, and Matthew Walters

4.1 Introduction and Summary

4.2 Introduction

Quantum field theory, while an excellent framework for conceptualizing many of the pressing problems in modern physics, provides little guidance in actually calculating phenomena outside of the so-called 'weakly-coupled' physical regime, in which particles are taken to be approximately free and interactions are approximated via Taylor series[69]. The terms in this Taylor series are usually represented by Feynman diagrams and grow exponentially more numerous as orders are added in the interaction parameter; they also become more difficult to calculate. Accordingly, the 'summing diagrams'

approach to QFT is only really useful when the interactions are weak enough that the series converges nicely in the first two or three orders. This is the case for many interesting processes, including the electroweak interactions in particle physics, but it is also not true of many others, such as quantum chromodynamics (QCD), which models the strong interaction.

The traditional way to investigate strongly-coupled quantum field theories like QCD is to quantize spacetime on a lattice, thereby reducing the infinite-dimensional problem to a finite-dimensional one which can be simulated on a computer[70]. This method changes the objects of study from continuum quantum fields to a discrete set of sites – the field can be reconstructed from the sites, but any variations taking place on a smaller length scale than the lattice spacing a become invisible. In the language of QFT, this effectively places an energy cutoff at $1/a$, above which all physics is lost.

In recent years, a competing procedure for studying strongly-coupled theories has emerged, called Hamiltonian truncation[71]. The idea is that, rather than discretizing the individual modes of field excitations as a lattice does, one will instead discretize the space of possible modes which can be included, and then impose some natural cutoff to make this space finite. The modes themselves are still treated as exact continuum objects, so this provides a line of inquiry which is in some sense orthogonal to that of the lattice.

If one is to attempt truncation, the first and paramount question is which full basis to begin with (and subsequently truncate). Recent approaches have tended to start with high-energy CFTs due to their orderly behavior, then add relevant operators to the Hamiltonian and renormalize the theory to

low energy[72]. Because the spectrum of CFT operators is naturally discrete and bounded below in dimension Δ, we can produce a finite basis by simply removing all operators having $\Delta > \Delta_0$ for some cutoff Δ_0. If the CFT is placed on a sphere, this dimension cutoff corresponds to an energy cutoff, so by performing it we are including low-energy operators and excluding high-energy ones. If we then flow the theory to low energy, we expect that these low energy modes will be the most relevant, and therefore low energy phenomena ought to be represented reasonably well by them[73].

This technique has been successfully used to study QFTs in two dimensions [74], but a 3D formulation has not yet materialized. In this chapter, we present a complete accounting of the theory necessary to prepare a ϕ^4 theory for conformal truncation in 3D, along with a numerical implementation of this truncation, which we then use to study the 3D Ising model as a proof of concept. We are able to observe the closing of the mass gap as the coupling strength is increased and correctly reproduce the spectral density of the low energy theory.

4.3 Conformal Truncation and Scalar Field Theory

4.3.1 Review of Conformal Truncation

Conformal truncation is a method for using CFT data to numerically study the IR dynamics of more general QFTs. This method can be applied to any theory that can be described as an RG flow originating from some UV CFT

deformed by one or more relevant operators,

$$S = S_{\text{CFT}} - \lambda \int d^d x \, \mathcal{O}_R(x). \tag{4.3.1}$$

Following the approach presented in [73], a useful basis for the Hilbert space of this theory consists of UV eigenstates of the quadratic Casimir of the conformal group,

$$|\mathcal{C}, \vec{P}, \mu\rangle \equiv \int d^d x \, e^{-iP\cdot x} \mathcal{O}(x)|0\rangle, \tag{4.3.2}$$

where $\mu^2 \equiv P^2$. These basis states are created by primary operators[1] in the original CFT, and are characterized by their Casimir eigenvalue, spatial momentum, and invariant mass (suppressing other possible quantum numbers like the spin ℓ).

The strategy of conformal truncation is to restrict the Hilbert space to the subspace spanned by states with Casimir eigenvalue $\mathcal{C} \leq \mathcal{C}_{\text{max}}$. The full Hamiltonian (CFT + deformation), when restricted to this subspace, can be diagonalized numerically, yielding an approximation to the true spectrum of the IR QFT.

To define the Hamiltonian, we first need to choose a quantization scheme. As discussed in [73], we work in lightcone quantization, with the Hilbert space defined on slices of constant lightcone "time" $x^+ \equiv \frac{1}{\sqrt{2}}(t + x)$. We thus need

[1] In this work, "primary" refers to any operator which is primary with respect to the global conformal group $SO(d,2)$ and thus annihilated by the special conformal generators ($[K_\mu, \mathcal{O}(0)] = 0$). In 2D, this includes operators which are often referred to as "quasi-primary" or "global primary" in the literature.

to compute matrix elements for the associated lightcone Hamiltonian

$$P_+ = P_+^{(\mathrm{CFT})} + \lambda \int d^{d-1}\vec{x}\, \mathcal{O}_R(x^+ = 0, \vec{x}). \tag{4.3.3}$$

By construction, our basis is built from eigenstates of the CFT Hamiltonian, so we only need to compute matrix elements associated with the relevant deformation. These matrix elements are simply Fourier transforms of three-point functions in the original UV CFT,

$$\langle \mathcal{C}, \vec{P}, \mu | \delta P_+ | \mathcal{C}', \vec{P}', \mu' \rangle = \lambda \int d^d x\, d^{d-1}\vec{y}\, d^d z\, e^{i(P\cdot x - P'\cdot z)} \langle \mathcal{O}(x) \mathcal{O}_R(y) \mathcal{O}'(z) \rangle \tag{4.3.4}$$

We thus only need data from the UV fixed point to study the full RG flow: the spectrum of local operators gives us a complete basis, while the OPE coefficients give us the Hamiltonian matrix elements.

4.3.2 3D Scalar Field Theory

Our starting point is a UV CFT of a free scalar field ϕ with the Lagrangian

$$\mathcal{L}_{\mathrm{CFT}} = \frac{1}{2} : \partial_\mu \phi \partial^\mu \phi :, \tag{4.3.5}$$

where the notation $: \mathcal{O} :$ indicates that the operator should be normal-ordered. We will work in $2+1$ dimensions in lightcone coordinates, which are defined by $x^\pm \equiv \frac{1}{\sqrt{2}}(t \pm x)$, as well as the tranverse direction $x^\perp$. The coordinate x^+ is treated as the "time" direction and the metric is given by

$$ds^2 = 2dx^+ dx^- - dx^{\perp 2}. \tag{4.3.6}$$

The associated momenta are given by $p_\mu = i\partial_\mu$, from which we can determine the Lorentz invariant quantity

$$p^2 = 2p_+p_- - p_\perp^2. \tag{4.3.7}$$

Our goal will be to determine the IR spectrum and eigenstates by diagonalizing the invariant mass-squared operator in a frame with total momentum $\vec{P}$. In terms of the momentum generators, this means diagonalizing

$$M^2 = 2P_+P_- - P_\perp^2. \tag{4.3.8}$$

We will diagonalize this operator on a basis of Casimir eigenstates associated with the UV free scalar. The free scalar field can be expanded in terms of its mode functions

$$\phi(x) = \int \frac{d^2p}{(2\pi)^2\sqrt{2p_-}} \left(e^{-ip\cdot x}a_p + e^{ip\cdot x}a_p^\dagger\right), \tag{4.3.9}$$

where

$$\left[a_p, a_q^\dagger\right] = (2\pi)^2\delta(p-q). \tag{4.3.10}$$

This expansion for $\phi(x)$ leads to an expression for the lightcone Hamiltonian P_+ (as well as the other lightcone momenta) in terms of oscillator modes, as we will see momentarily. We will then diagonalize the mass-squared operator by similarly expressing our complete basis states in terms of mode functions, truncating at some maximum Casimir eigenvalue to obtain a finite-dimensional matrix.

After expanding in oscillator modes, the CFT Hamiltonian takes the form

$$P_+^{(\mathrm{CFT})} = \int \frac{d^2p}{(2\pi)^2} a_p^\dagger a_p \frac{p_\perp^2}{2p_-}. \tag{4.3.11}$$

The deformations to the UV CFT that we will study are the mass term and a quartic interaction, given by

$$\delta\mathcal{L} = -\frac{1}{2}m^2\phi^2 - \frac{1}{4!}\lambda\phi^4. \tag{4.3.12}$$

This results in the following corrections to the lightcone Hamiltonian, respectively:

$$\delta P_+^{(m)} = \int \frac{d^2p}{(2\pi)^2} a_p^\dagger a_p \frac{m^2}{2p_-}, \tag{4.3.13}$$

and

$$\delta P_+^{(\lambda)} = \frac{\lambda}{24}\int \frac{d^2p d^2q d^2k}{(2\pi)^6\sqrt{8p_-q_-k_-}}\left(\frac{4a_p^\dagger a_q^\dagger a_k^\dagger a_{p+q+k}}{\sqrt{2(p_-+q_-+k_-)}} + \text{h.c.} + \frac{6a_p^\dagger a_q^\dagger a_k a_{p+q-k}}{\sqrt{2(p_-+q_--k_-)}}\right). \tag{4.3.14}$$

4.3.3 Conformal Basis for 3D Scalar Fields

The conformal truncation prescription amounts to diagonalizing M^2 on a basis of Casimir eigenstates. In this section, we will explain how to construct these eigenstates and how the basis is modified in the presence of the mass deformation.

Our starting point in the UV is the free massless scalar field, and so our basis is comprised of primary (and descendant) operators of the free scalar. In order to construct these operators, we have the following building blocks

$$\phi, \qquad \partial_+\phi, \qquad \partial_-\phi, \qquad \partial_\perp\phi. \tag{4.3.15}$$

The equations of motion imply that $\partial_+\phi = \frac{\partial_\perp^2}{2\partial_-}\phi$, so we can focus on only the $\partial_-\phi$ and $\partial_\perp\phi$ building blocks.

The idea is to construct a basis of Casimir eigenstates from these building blocks. In previous work, we started with the "all-minus" subset of the basis, comprised of operators built only from ϕ and ∂_- derivatives. Then, we obtained the other states by acting on the all-minus states with the Pauli-Lubanski operator.

Our approach in this work will be more pedestrian. We will simply start with the building blocks eq. (4.3.15) and construct the linear combinations that are primary with a brute-force algorithm. These operators take the form

$$\mathcal{O}(x) = \sum_{\{m_n\}} C^{\mathcal{O}}_{\{m_n\}} \partial^{m_1}\phi(x)\partial^{m_2}\phi(x)\cdots\partial^{m_n}\phi(x), \tag{4.3.16}$$

for some yet-to-be-determined coefficients $C^{\mathcal{O}}_{\{m_n\}}$. We can express these operators in momentum space by inserting a complete set of states:

$$\begin{aligned}|\mathcal{O};\vec{P},\mu\rangle &= \frac{1}{n!}\int \frac{d^2p_1\cdots d^2p_n}{(2\pi)^{2n}2p_{1-}\cdots 2p_{n-}}\langle p_1,\ldots,p_n|\mathcal{O};\vec{P},\mu\rangle|p_1,\ldots,p_n\rangle \\ &= \frac{1}{n!}\int \frac{d^2p_1\cdots d^2p_n}{(2\pi)^{2n}2p_{1-}\cdots 2p_{n-}}(2\pi)^3\delta^3\left(\sum_i p_i - P\right)F_{\mathcal{O}}(p)|p_1,\ldots,p_n\rangle,\end{aligned} \tag{4.3.17}$$

where the wavefunction $F_{\mathcal{O}}(p)|p_1,\ldots,p_n\rangle$ is just given by the overlap of the operator with a Fock space state

$$F_{\mathcal{O}}(p) = \langle\mathcal{O}(0)|p_1,\ldots,p_n\rangle = \sum_{\{m_n\}} C^{\mathcal{O}}_{\{m_n\}} p_1^{m_1}\cdots p_n^{m_n}. \tag{4.3.18}$$

We can therefore focus on determining these polynomials, which are simply

the Fourier transforms of local operators.

In order to determine these wavefunctions, we must find the operators that are annihilated by the special conformal transformations K_μ. As differential operators acting on a generic monomial $P_+^a P_-^b P_\perp^c \phi$, they take the form

$$\begin{aligned}
K_- &= 2P_+\frac{\partial^2}{\partial P_+^2} + 2P_\perp\frac{\partial^2}{\partial P_+\partial P_\perp} + 2\Delta_\phi\frac{\partial}{\partial P_+} + P_-\frac{\partial^2}{\partial P_\perp^2},\\
K_\perp &= -2P_+\frac{\partial^2}{\partial P_+\partial P_\perp} - 2P_-\frac{\partial^2}{\partial P_-\partial P_\perp} - P_\perp\frac{\partial^2}{\partial P_\perp^2} - 2\Delta_\phi\frac{\partial}{\partial P_\perp} - 2P_\perp\frac{\partial^2}{\partial P_+\partial P_-},\\
K_+ &= 2P_-\frac{\partial^2}{\partial P_-^2} + 2P_\perp\frac{\partial^2}{\partial P_-\partial P_\perp} + 2\Delta_\phi\frac{\partial}{\partial P_-} + P_+\frac{\partial^2}{\partial P_\perp^2}.
\end{aligned} \tag{4.3.19}$$

We could determine the primary operators by then finding the null space of these operators acting on the space of monomials. However, this basis of primary operators is actually not the final basis we are after.

To explain why, we first note that we are interested in deforming the CFT Hamiltonian by a mass term (and interaction terms), as given in eq. (4.3.13). As reviewed in Appendix 4.A, the presence of this mass term results in a divergence in the mass matrix elements. Regulating this divergence with an ϵ prescription, we find some eigenstates that are lifted out of the spectrum and those that remain finite as $\epsilon \to 0$. The eigenstates corresponding to the finite matrix elements are a reshuffling of the original primary basis, such that these states satisfy *Dirichlet* boundary conditions. Explicitly, this means operators which have at least one factor of P_- on each particle insertion to cancel against the Lorentz invariant measure of the mass deformation. In momentum space,

this corresponds to wavefunctions of the type

$$p_{1-}p_{2-}\cdots p_{n-}\,(\cdots)\,, \tag{4.3.20}$$

where the second set of ellipses indicates a generic function of p_{i-}, $p_{i\perp}$, and p_{i+}. We will therefore introduce the following notation to specify a Dirichlet basis state:

$$\begin{aligned}|\mathcal{O};\vec{P},\mu\rangle =&\frac{1}{n!}\int\frac{d^2p_1\cdots d^2p_n}{(2\pi)^{2n}2p_{1-}\cdots 2p_{n-}}(2\pi)^3\delta^3\left(\sum_i p_i - P\right)\\ &\times p_{1-}p_{2-}\cdots p_{n-}\bar{F}_{\mathcal{O}}(p)|p_1,\cdots,p_n\rangle,\end{aligned} \tag{4.3.21}$$

where $\bar{F}_{\mathcal{O}}(p)$ indicates the Dirichlet wavefunction.

One might be tempted to create a basis for the Dirichlet states by taking a list of all primary operators and throwing out the non-Dirichlet ones. Unfortunately, this would be incomplete, because acting with P_- can cause an operator to become Dirichlet when it wasn't before. Therefore, we need to include both the Dirichlet primaries and the non-primary Dirichlet operators for which acting with K produces non-Dirichlet states. But these, too, are not in general orthonormal, and lacking a good systematic way to identify an orthonormal subset of them, we opted to abandon the primaries altogether, instead writing all possible below-cutoff Dirichlet states and finding an orthonormal subset using the Gram-Schmidt process. Details of our implementation can be found in Appendices 4.A and 4.C.

Finally, to complete the discussion on our basis states, we must note that μ as it appears in (4.3.17) is still a continuous parameter. It denotes the kinetic energy of the state i.e. its eigenvalue under P^2. In order to obtain a complete,

discrete basis, we must introduce some prescription to discretize over this parameter. A general way to do this is to integrate μ weighted by functions that carry some index $k \in \mathbb{Z}_{\geq 0}$:

$$|\mathcal{O};\vec{P},k\rangle = \int d\mu^2 f(\mu) g_k(\mu) \frac{1}{n!} \int \frac{d^2p_1 \cdots d^2p_n}{(2\pi)^{2n} 2p_{1-} \cdots 2p_{n-}} (2\pi)^3 \delta^3 \left(\sum_i p_i - P \right)$$
$$\times p_{1-} p_{2-} \cdots p_{n-} F_{\mathcal{O}}(p) |p_1, \cdots, p_n\rangle, \tag{4.3.22}$$

where $f(\mu)$ is a measure that we have freedom to choose. The region of integration for μ is supposed to be taken from $[0, \infty)$. The reason that it is non-negative is that there is a Wightman prescription for the 2-pt. function of these operators that ensures positivity of the lightcone momenta. However, the integral will diverge and must be regulated. For this reason, we have to introduce a UV cutoff Λ. Cutting off the integral and rescaling the region of integration to $[0,1]$ we find that our final states are given by

$$\boxed{|\mathcal{O};\vec{P},k\rangle = \frac{1}{\sqrt{2\pi} P_-^{n+|\boldsymbol{\lambda}_-|} \Lambda^{\frac{n-5}{2}+|\boldsymbol{\lambda}_\perp|}} \int_0^1 \frac{d\bar{\mu}^2}{\bar{\mu}^{\frac{n-3}{2}+|\boldsymbol{\lambda}_\perp|}} g_k(\bar{\mu})} \tag{4.3.23}$$

$$\boxed{\times \frac{1}{n!} \int \frac{d^2p_1 \cdots d^2p_n}{(2\pi)^{2n} 2p_{1-} \cdots 2p_{n-}} (2\pi)^3 \delta^3 \left(\sum_i p_i - P \right)} \tag{4.3.24}$$

$$\boxed{\times p_{1-} p_{2-} \cdots p_{n-} \bar{F}_{\mathcal{O}}(p) |p_1, \cdots, p_n\rangle,}$$

where we have defined the dimensionless $\bar{\mu} \equiv \frac{\mu}{\Lambda}$ and $|\boldsymbol{\lambda}_{-,\perp}|$ count the number of $-$ and $\perp$ derivatives in $F_{\mathcal{O}}(p)$, respectively. In this paper, we discretize μ into linearly spaced bins:

$$g_k(\bar{\mu}) = \frac{1}{\sqrt{\bar{\mu}_k^2 - \bar{\mu}_{k-1}^2}} \left[\theta(\bar{\mu}^2 - \bar{\mu}_{k-1}^2) - \theta(\bar{\mu}^2 - \bar{\mu}_k^2) \right], \tag{4.3.25}$$

where θ is the Heaviside step function. The purpose of the above equation is to the set the region of integration in $\bar{\mu}$ to be in a bin between $\bar{\mu}_{k-1}$ and $\bar{\mu}_k$. Truncating at some $k_{\max}$, we can obtain a discrete, finite-dimensional basis of Dirichlet states. The normalization of these weight functions is chosen such that

$$\int_0^1 d\bar{\mu}^2 g_k(\bar{\mu}) g_{k'}(\bar{\mu}) = \delta_{kk'}. \tag{4.3.26}$$

This completes our discussion of computing the Dirichlet basis. To summarize: we tabulate all possible monomials $P_+^a P_-^b P_\perp^c \phi$ that satisfy Dirichlet boundary conditions and obtain the orthonormal linear combinations through a Gram-Schmidt procedure. We discretize in μ using the weight functions in eq. (4.3.25) and truncate at some $\mathcal{C}_{\max}$, $k_{\max}$ obtain our final discrete, truncated basis.

4.3.4 Review of Spectral Densities

After we have truncated the basis to some $\mathcal{C}_{\max}$ and computed the associated Hamiltonian matrix elements, we can construct the invariant mass operator

$$M^2 = 2P_+P_-. \tag{4.3.27}$$

Because our basis consists of P_- eigenstates, diagonalizing this Lorentz invariant operator is actually equivalent to diagonalizing the lightcone Hamiltonian P_+.

The mass eigenvalues that result from diagonalizing M^2 are an approximation to the spectrum of the IR QFT. However, in addition to the eigenvalues, we also obtain the associated eigenstates $|\mu_i\rangle$, which we can use to compute

dynamical IR observables. One natural and important observable for us to study is the spectral density of any local operator $\mathcal{O}(x)$,

$$\rho_{\mathcal{O}}(\mu) \equiv \sum_i |\langle \mathcal{O}(0)|\mu_i\rangle|^2 \delta(\mu^2 - \mu_i^2). \tag{4.3.28}$$

As shown in eq. (4.4.1), spectral densities encode the same information as real-time, infinite-volume correlation functions. For presenting results, it will be more convenient to show the integrated spectral density,

$$I_{\mathcal{O}}(\mu) \equiv \int_0^{\mu^2} d\mu'^2 \rho_{\mathcal{O}}(\mu') = \sum_{\mu_i \leq \mu} |\langle \mathcal{O}(0)|\mu_i\rangle|^2, \tag{4.3.29}$$

which contains the same dynamical information as the spectral density.

4.4 Sanity Checks

In this section, we perform consistency checks in the free massive theory where $\lambda = 0$. We then compare with theoretical predictions, which gives us a nontrivial check of the Dirichlet basis.

In section 4.4.1, we first explain how to compute the theoretical predictions for the spectral density associated with a generic local operator $\mathcal{O}_{\mu_1,\ldots,\mu_\ell}(x)$. We then compare these analytic answers to the numerical results obtained from conformal truncation. We will primarily focus on comparisons involving the energy-momentum tensor.

4.4.1 Spectral Densities in Free Field Theory

Let's briefly review some details about spectral densities of operators in free massive theory. The spectral density is the decomposition of the two-point

correlation function in terms of mass eigenstates:

$$\langle \mathcal{O}(x)\mathcal{O}(0)\rangle = \int d\mu^2 \rho_{\mathcal{O}}(\mu) \int \frac{d^2P}{(2\pi)^2 2P_0} e^{-iP\cdot x}. \tag{4.4.1}$$

Forbrevity, we have omitted any tensor structure, but the operators appearing on theLHS could, for example, be various components of spinning operators. In a freetheory, we can expand the correlator on the LHS in terms of Fock space modes:

$$\begin{aligned}\langle \mathcal{O}(x)\mathcal{O}(0)\rangle &= \frac{1}{n!}\int \frac{d^3p_1\cdots d^3p_n}{(2\pi)^{3n}} \prod_i (2\pi)\delta(p_i^2 - m^2) |\langle \mathcal{O}(0)|p_1,\ldots,p_n\rangle|^2 e^{-i(\sum_i p_i)\cdot x} \\ &= \int \frac{d\mu^2}{2\pi}\frac{1}{n!}\int \frac{d^3p_1\cdots d^3p_n}{(2\pi)^{3n}} \left(\prod_i (2\pi)\delta(p_i^2-m^2)\right)(2\pi)^3\delta^3\left(P - \sum_i p_i\right) \\ &\quad \times |\langle \mathcal{O}(0)|p_1,\ldots,p_n\rangle|^2 \times \int \frac{d^2P}{(2\pi)^2 2P_0} e^{-iP\cdot x},\end{aligned} \tag{4.4.2}$$

where we inserted a complete set of states and used the fact that $d^3P = d\mu^2 \frac{d^2P}{2P_0}$. Equating this to eq. (4.4.1), we can therefore obtain an explicit equation for the spectral density associated with any local operator $\mathcal{O}$:

$$\rho_{\mathcal{O}}(\mu) = \frac{1}{2\pi n!}\int \frac{d^3p_1\cdots d^3p_n}{(2\pi)^{3n}} \left(\prod_i (2\pi)\delta(p_i^2-m^2)\right)(2\pi)^3\delta^3(P-\sum_i p_i)|\langle \mathcal{O}(0)|p_1,\ldots,p_n\rangle|^2. \tag{4.4.3}$$

This formula also holds for operators with spin, so that we can compare theoretical predictions for spectral densities of various components of spinning operators. The simplest way to apply eq. (4.4.3) is to compute the overlap $|\langle \mathcal{O}(0)|p_1,\ldots,p_n\rangle|$, evaluate the integrals in the total momentum frame $P = (\mu, \vec{0})$, $p_i = (E_i, \vec{p}_i)$, and then perform a boost to the lightcone frame. Let's see

how this works for a few examples.

Consider the spectral density associated with the simplest two-particle operator ϕ^2. The overlap of this operator with the two-particle Fock space state is simply

$$\langle \phi^2(0)|p_1, p_2\rangle = 2. \tag{4.4.4}$$

Plugging this into eq. (4.4.3), and evaluating in the frame

$$P = (\mu, \vec{0}), \qquad p_1 = (E_1, \vec{p}_1), \qquad p_2 = (E_2, \vec{p}_2), \tag{4.4.5}$$

we find

$$\rho_{\phi^2}(\mu) = \frac{1}{4\pi\mu}\theta(\mu - 2m). \tag{4.4.6}$$

Note that the step function signifies that the two-particle spectral density starts at the two-particle threshold, as expected. There is no need to boost this answer to the lightcone frame as this spectral density is associated with the scalar two-point function $\langle \phi^2\phi^2\rangle$. We can repeat this analysis for any ϕ^n operator which gives the spectral density

$$\rho_{\phi^n}(\mu) = \frac{n!(\mu - nm)^{n-2}}{(n-2)!(4\pi)^{n-12\mu}}. \tag{4.4.7}$$

Now let's consider a more nontrival example of the stress-energy tensor. It is given by

$$T_{\mu\nu} = \frac{3}{4}\partial_\mu\phi\partial_\nu\phi - \frac{1}{4}\eta_{\mu\nu}\partial_\sigma\phi\partial^\sigma\phi - \frac{1}{4}\phi\partial_\mu\partial_\nu\phi + \frac{1}{2}m^2\eta_{\mu\nu}\phi^2. \tag{4.4.8}$$

Let's start with the all minus component T_{--}. The overlap is given by

$$\langle T_{--}(0)|p_1, p_2\rangle = -\frac{1}{4}\left(6p_{1-}p_{2-} - p_{1-}^2 - p_{2-}^2\right). \tag{4.4.9}$$

We can evaluate the integrals in eq. (4.4.3) by noting that

$$p_{1\pm} = \frac{1}{\sqrt{2}}(E_1 \pm p_{1x}), \qquad p_{2\pm} = \frac{1}{\sqrt{2}}(E_2 \pm p_{2,x}), \tag{4.4.10}$$

which gives

$$\tilde{\rho}_{T_{--}}(\mu) = \frac{\mu^4 - 8\mu^2 m^2 + 48m^4}{2048\pi\mu}, \tag{4.4.11}$$

where the tilde indicates that we still need to boost to the lightcone frame. We have computed the spectral density associated with T_{--} in the frame $(P_+, P_-, P_\perp) = \left(\frac{\mu}{\sqrt{2}}, \frac{\mu}{\sqrt{2}}, 0\right)$ while the lightcone frame is given by $(P_+, P_-, P_\perp) = \left(\frac{\mu^2}{2P_-}, P_-, 0\right)$. In lightcone coordinates, a boost which sends a vector $V_+ \to \tau V_+$ takes $V_- \to \tau^{-1} V_-$ to preserve the lightcone inner product. We therefore need $\tau = \frac{\mu}{\sqrt{2}P_-}$ so that $\rho_{T_{--}} = \tau^{-4}\tilde{\rho}_{T_{--}}$, since there are four minus indices in $\langle T_{--}T_{--}\rangle$. We therefore get

$$\boxed{\rho_{T_{--}}(\mu) = \frac{P_-^4(\mu^4 - 8\mu^2 m^2 + 48m^4)}{512\pi\mu^5}.} \tag{4.4.12}$$

We can apply this procedure to generate the spectral densities for the remaining components. Note that

$$\langle T_{-\perp}(0)|p_1, p_2\rangle = -\frac{1}{4}(3p_{1-}p_{2\perp} + 3p_{1\perp}p_{2-} - p_{1-}p_{1\perp} - p_{2-}p_{2\perp}), \tag{4.4.13}$$

which gives

$$\boxed{\rho_{T_{-\perp}}(\mu) = \frac{P_-^2(\mu^2 - 4m^2)^2}{512\pi\mu^3}.} \tag{4.4.14}$$

Finally, we have

$$\langle T_{\perp\perp}(0)|p_1, p_2\rangle = -\frac{1}{4}(4p_{1\perp}p_{2\perp} + 2p_{1+}p_{2-} + 2p_{1-}p_{2+} - p_{1\perp}^2 - p_{2\perp}^2) - m^2\eta_{\perp\perp}, \tag{4.4.15}$$

which gives

$$\boxed{\rho_{T_{\perp\perp}}(\mu) = \frac{\mu^4 - 8m^2\mu^2 + 88m^4}{512\pi\mu}.} \tag{4.4.16}$$

Now that we have theoretical predictions for these spectral densities, we can compare them to those obtained from conformal truncation. In order to do this, we will need the overlaps of the UV operators with our eigenstates in order to compute the cumulative overlap in eq. (4.3.29). That is to say, in order to compute eq. (4.3.29), we can insert a resolution of the identity corresponding to our basis

$$I_{\mathcal{O}}(\mu) = \sum_{\mu_i \leq \mu} \sum_{\tilde{\mathcal{O}}} |\langle \mathcal{O}(0)|\tilde{\mathcal{O}}\rangle\langle\tilde{\mathcal{O}}|\mu_i\rangle|^2. \tag{4.4.17}$$

The second piece $\langle\tilde{\mathcal{O}}|\mu_i\rangle$ merely picks out that operator of our eigenvector. Meanwhile, the overlaps $\langle\mathcal{O}(0)|\tilde{\mathcal{O}}\rangle$ are given by

$$\langle \mathcal{O}(0)|\tilde{\mathcal{O}}\rangle = \frac{P_-^{d_-}\Lambda^{\frac{n-1}{2}+d_\perp}}{\sqrt{2\pi}} \left(\frac{2}{\frac{n+1}{2}+d_\perp}\right) \left(\frac{\mu_k^{\frac{n+1+2d_\perp}{2}} - \mu_{k-1}^{\frac{n+1+2d_\perp}{2}}}{\sqrt{\mu_k^2 - \mu_{k-1}^2}}\right) \times \mathcal{I}^{\text{inner}}_{\mathcal{O}\tilde{\mathcal{O}}}. \tag{4.4.18}$$

$d_{-,\perp}$ count the number of minus and perp derivatives in $\mathcal{O}$. And $\mathcal{I}^{\text{inner}}_{\mathcal{O}\tilde{\mathcal{O}}}$ is the inner product between $\mathcal{O}$ and $\tilde{\mathcal{O}}$ as defined in eq. (4.A.21)[2].

In Fig. 4.1, we show the spectral densities of the operators ϕ^2 through ϕ^5. We see that the numerical results agree with the theoretical prediction for the spectral density for a wide range of μ. Our IR cutoff is set by k_{max}, where

$$\Lambda_{\text{IR}} \sim \frac{\Lambda_{\text{UV}}}{k_{\text{max}}} \tag{4.4.19}$$

[2]Note that the wavefunction corresponding to $\mathcal{O}$ isn't necessarily one that satisfies the Dirichlet boundary conditions which we introduce in later sections.

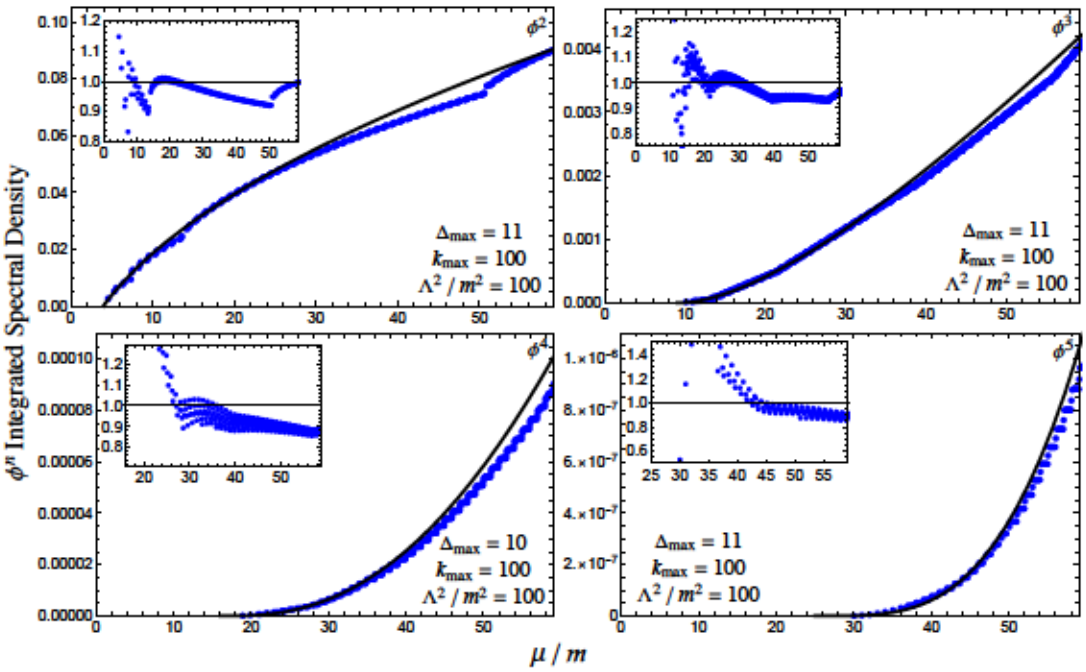

Figure 4.1: Integrated spectral densities for ϕ^2 (upper left), ϕ^3 (upper right), ϕ^4 (lower left), and ϕ^5 (lower right) in massive free field theory ($\lambda = 0$), both the raw value (main plot) and normalized by the theoretical prediction (inset). The conformal truncation results (blue dots) for each plot are computed using the Δ_{max} shown, with the corresponding number of n-particle basis states, and compared to the theoretical prediction (black curve).

and at $k_{\text{max}} = 100$, we see that the IR cutoff is small enough that the spectral density is within a few percent of the theoretical prediction even for $\mu \gg m$. In Figs. 4.2 and 4.3, we show the spectral densities for T_{--}, $T_{-\perp}$, which similarly agree with the analytic predictions. Similar plots exist for the remaining components and also agree closely with the theoretical result.

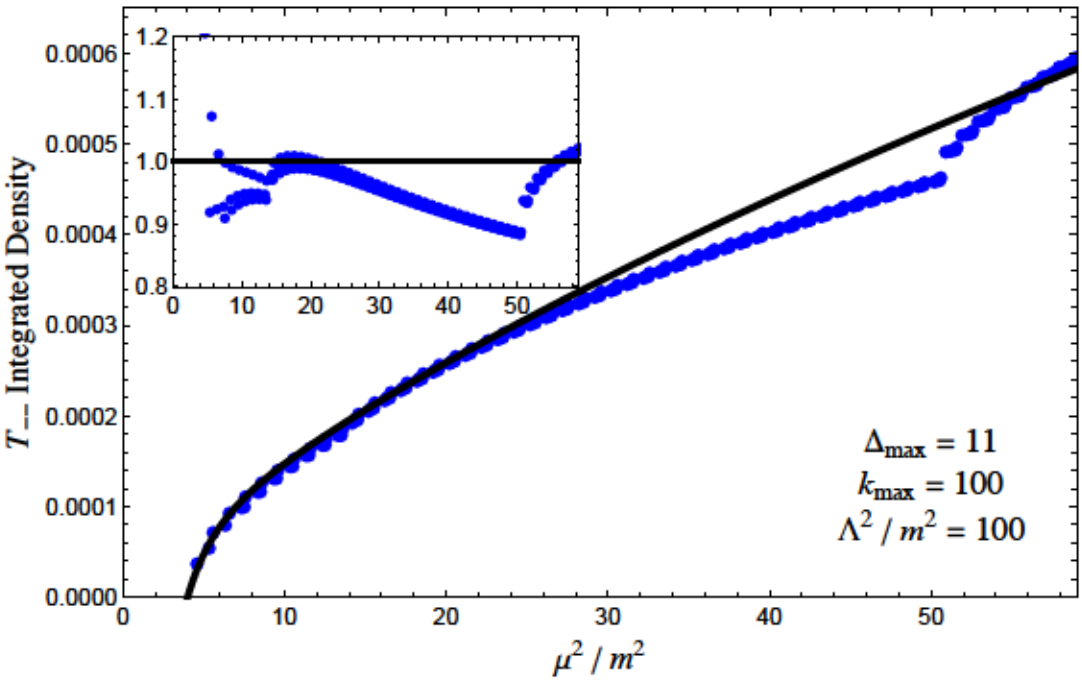

Figure 4.2: Integrated spectral densities for the stress tensor component T_{--} in massive free field theory ($\lambda = 0$), both the raw value (main plot) and normalized by the theoretical prediction (inset). The conformal truncation results (blue dots) for each plot are computed using the Δ_{max} shown, with the corresponding number of n-particle basis states, and compared to the theoretical prediction (black curve).

4.5 Discussion

This project is still in the final debugging stages, but we believe it to be numerically correct and are working on producing illustrative plots now. Figure 4.4 gives a visualization of the Hamiltonian created by the truncation methods of this chapter.

In order to demonstrate the correctness of our truncation method, we can look at the closing of the Ising model's mass gap as the strength of the deformation's coupling λ is increased. This can be seen by finding the eigenvalues of the Hamiltonian and taking the lowest one – this will be the mass of the

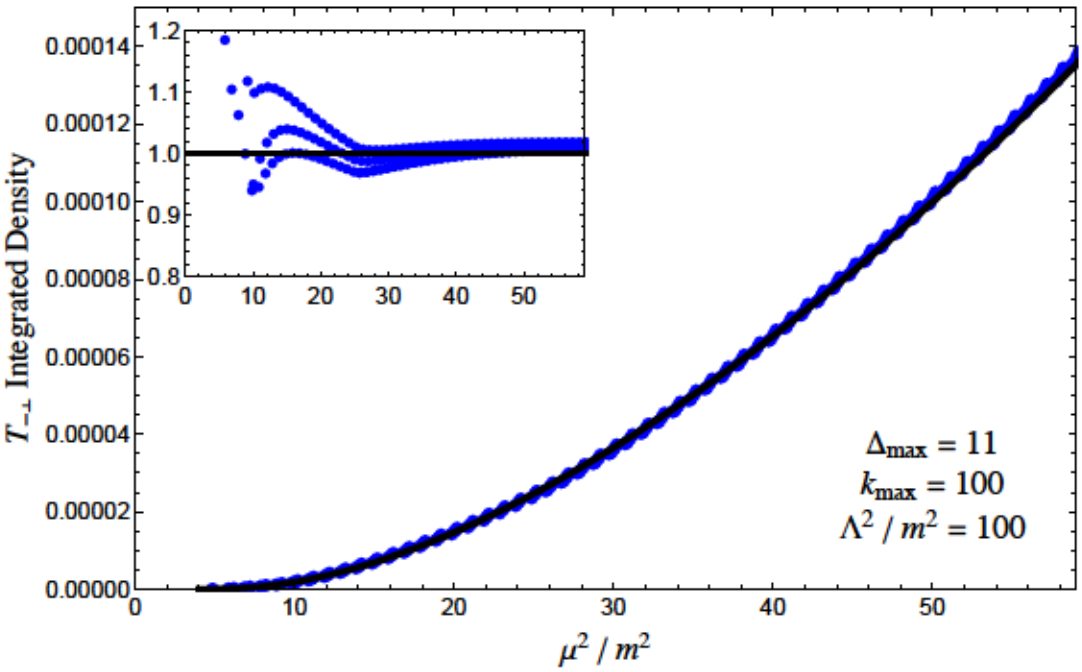

Figure 4.3: Integrated spectral densities for $T_{-\perp}$ in massive free field theory ($\lambda = 0$), both the raw value (main plot) and normalized by the theoretical prediction (inset). The conformal truncation results (blue dots) for each plot are computed using the Δ_{max} shown, with the corresponding number of n-particle basis states, and compared to the theoretical prediction (black curve).

1-particle state, which starts at a finite value and drops to 0 (along with the other states) as the mass gap closes. This is shown in figure 4.5, and the observed behavior seems consistent with that seen in 2D and less comprehensive studies of 3D.

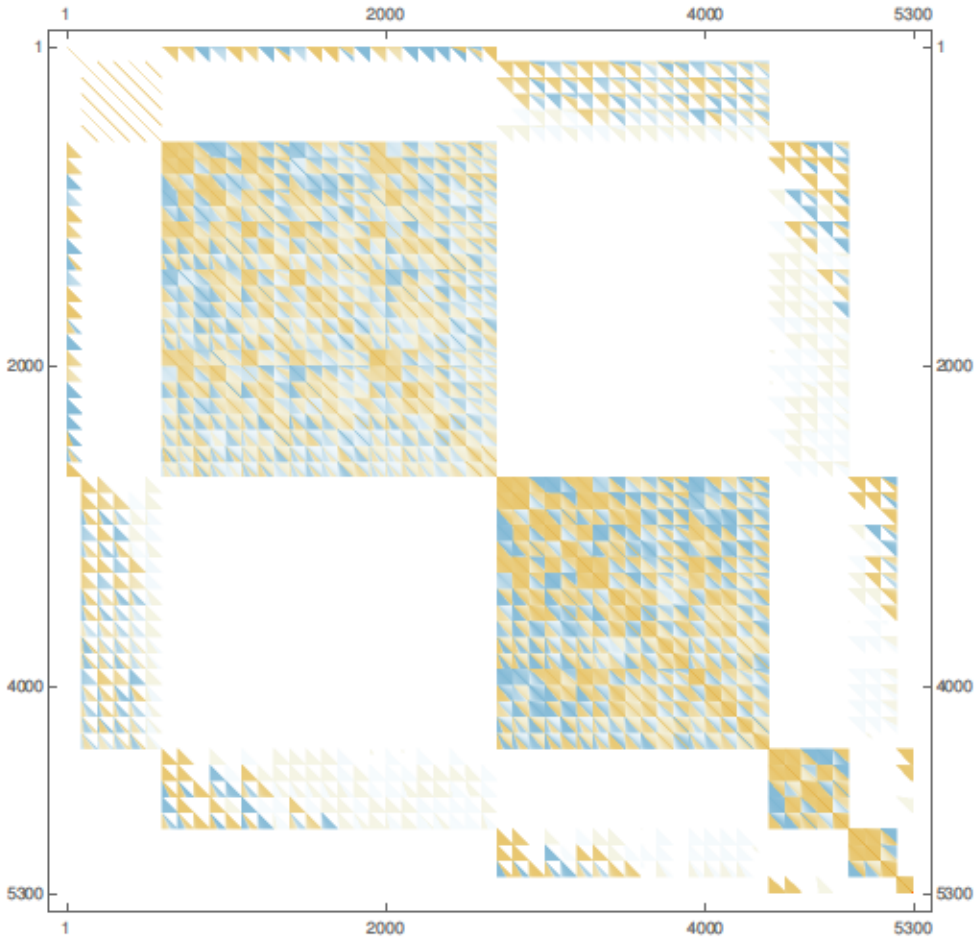

Figure 4.4: This is the $P_\perp$-even Hamiltonian produced with $\Delta_{\max} = 11$, $k_{\max} = 100$, and $m^2 = \Lambda = \lambda = 1$. Warm colors are positive entries and cool colors are negative entries, with saturation indicating the magnitude. The $n \to n + 2$ entries outside of the diagonal blocks are jagged because these interactions are kinematically prohibited when the low-n state has more energy than the high-n state, which is the half of the block closer to the diagonal.

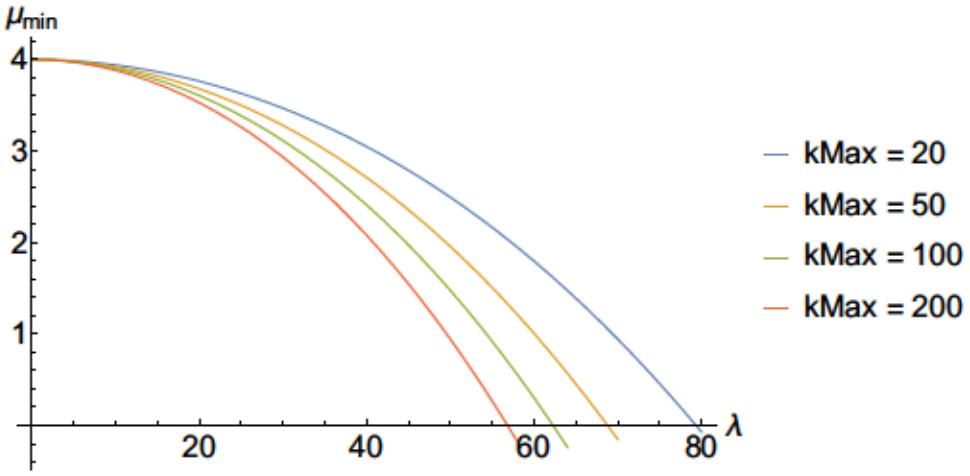

Figure 4.5: This shows the effective mass of the single-particle state as a function of the interaction coupling λ. Each of these is at $\Delta_{max} = 8, m = 1, \Lambda = 20$, but k_{max} is varied between 20 and 200, appearing to approach an asymptotic 'correct' value as $k_{max} \to \infty$.

Appendix

4.A Constructing the Basis of Dirichlet States

By definition, the original basis of Casimir eigenstates consists of eigenstates of the CFT Hamiltonian. However, once we introduce a relevant mass deformation to the Hamiltonian

$$\delta P_+^{(m)} = \int \frac{d^2p}{(2\pi)^2} a_p^\dagger a_p \frac{m^2}{2p_-}, \tag{4.A.1}$$

there are IR divergences associated with the mass matrix whenever any individual lightcone momentum of an n-particle eigenstate go to zero. If we regulate these divergences by introducing a small parameter ϵ, the resultant mass spectrum contains two types of eigenstates: those that diverge as $\epsilon \to 0$ and those that remain finite. The states that diverge in this limit are lifted out of the spectrum, such that we can focus on the low-lying sector. The states that remain finite can be seen as a specific linear combination of Casimir eigenstates, a reshuffling of the original UV basis such that their eigenvalues are finite in the limit $\epsilon \to 0$. In practice, this reshuffling gives rise to a "Dirichlet" wavefunction $\tilde{F}_{\mathcal{O}}^{(n)}(p)$ that is schematically the product of the lightcone

momenta times a wavefunction which we denote $\bar{F}^{(n)}_{\mathcal{O}}(p)$:

$$F^{(n)}_{\mathcal{O}}(p) \to \tilde{F}^{(n)}_{\mathcal{O}}(p) \sim p_{1-} p_{2-} \cdots p_{n-} \bar{F}^{(n)}_{\mathcal{O}}(p). \tag{4.A.2}$$

We will drop the (n) superscript for brevity.

It is important to note that the size of the Dirichlet basis is smaller than that of the original Casimir basis. While every Dirichlet state has this overall factor of $p_{1-} \cdots p_{n-}$, we cannot obtain it from starting with the UV basis and simply tacking on the product of momenta. These states consist of *specific* linear combinations of UV primaries that are orthogonal with respect to an inner product, and in the following section we outline how to numerically compute them.

4.A.1 Two-Particle Example

Before we move onto the general case, we briefly review how the Dirichlet basis arises in a simple two-particle example. We will show how the addition of a mass deformation to the Hamiltonian reshuffles the basis, resulting in a divergent piece that is lifted out of the IR spectrum and a finite piece that is a physical state.

To see this, consider a truncated 2-particle basis consisting of the operators ϕ^2 and T_{--}, where T_{--} is given by[3]

$$T_{--} = \phi \partial_-^2 \phi - 3(\partial_- \phi)^2. \tag{4.A.3}$$

In momentum space, we can express the wavefunction associated with T_{--}

[3]Up to a normalization constant that we will ignore as it is not important for this discussion.

as

$$\int d^3x\, e^{ix\cdot P}\langle \phi\partial_-^2\phi(x) - 3(\partial_-\phi)^2(x)|p_1,p_2\rangle = [6p_{1-}p_{2-} - (p_1^2+p_2^2)]\times\delta(P-p_1-p_2), \tag{4.A.4}$$

Let's first start with the simple example of the mass term matrix element between ϕ^2. We find

$$\begin{aligned}\langle \phi^2; P'|2P_-\delta P_+^{(m)}|\phi^2,P\rangle =& 2P_- m^2\int \frac{d^2k_1 d^2k_2}{(2\pi)^4 2k_{1-}2k_{2-}}(2\pi)^3\delta^3(k_1+k_2-P') \\ &\times(2\pi)^3\delta^3(k_1+k_2-P)\left(\frac{1}{k_{1-}}+\frac{1}{k_{2-}}\right).\end{aligned} \tag{4.A.5}$$

Already, we can see how the divergence will arise. We see that when any of the $k_{i-}\to 0$, the integral above will exhibit a divergence which will need to be regulated. In fact, the delta functions cause the two integrals above to collapse to a single integral and introducing an ϵ regulator and performing that integral using the coordinate transformations in Appendix 4.A.2, we find

$$\langle \phi^2; P'|2P_-\delta P_+^{(m)}|\phi^2,P\rangle = 2P_-(2\pi)^2\delta(\vec{P}-\vec{P}')\frac{m^2}{\mu}\left(\frac{1}{\sqrt{P_-\epsilon}}+\mathcal{O}(\epsilon)\right), \tag{4.A.6}$$

where $P^2=\mu^2$. As expected, this matrix element diverges as $1/\sqrt{\epsilon}$. Now, performing the same exercise for the other operator T_{--}, we find

$$\langle T_{--}; P'|2P_-\delta P_+^{(m)}|T_{--};P\rangle = 2P_-(2\pi)^2\delta^2(\vec{P}-\vec{P}')\frac{m^2}{\mu}\left(\frac{P_-^{7/2}}{\sqrt{\epsilon}}+\mathcal{O}(\epsilon)\right). \tag{4.A.7}$$

We can also similarly compute the matrix element between T_{--} and ϕ^2. Ignoring overall numerical factors and the μ dependence, we find that the divergent

part of the matrix elements looks like

$$M^2 \sim \frac{1}{\sqrt{\epsilon}} \begin{pmatrix} P_-^{-1/2} & P_-^{3/2} \\ P_-^{3/2} & P_-^{7/2} \end{pmatrix} \tag{4.A.8}$$

This matrix has two eigenvalues: 0 and one that diverges as $\epsilon \to 0$, which is $\sim \frac{1}{\sqrt{\epsilon}}$. If we look at the eigenvector corresponding to the former, we find that it is just a linear combination

$$\begin{pmatrix} P_-^2 & 1 \end{pmatrix} = -P_-^2\phi^2 + T_{--} = -(p_1+p_2)^2\phi^2 + T_{--} = -\phi\partial_-^2\phi - (\partial_-\phi)^2 + T_{--}. \tag{4.A.9}$$

We see that the $\phi\partial_-^2\phi$ cancels against the same term in T_{--}, leaving just a term proportional to $(\partial_-\phi)^2$. The effect of the Dirichlet boundary condition is to therefore to *reshuffle* the basis and remove the problematic piece in T_{--}. The reduced Dirichlet basis, which in this case consists of the single eigenstate corresponding to the operator $(\partial_-\phi)^2$, is the finite eigenstate, while the divergent piece is lifted out of the spectrum. In effect, the Dirichlet basis consists of reshuffling of the original basis such that the operators that remain have a product of momenta $p_{1-}p_{2-}\cdots p_{n-}$ necessary to cancel against the IR divergence.

The purpose of this example was to show how the Dirichlet basis arises from the standard conformal primary basis once we deform by a mass term. We see that the size of the Dirichlet basis is smaller than that of the original basis (and this behavior will persist as we increase the size of the basis). In practice, one could construct the Dirichlet states by finding the finite linear combinations of eigenstates, which amounts to determining the kernel of the divergent part of the mass matrix. However, our approach will simply be to

construct these states by demanding that every Dirichlet state has a product of momenta $p_{1-}p_{2-}\cdots p_{n-}$ and using their associated inner product. We will describe this in the next section.

4.A.2 General Case

While the above method for constructing the Dirichlet basis can be generalized, in this work we will explicitly construct the basis of Dirichlet states from their associated inner product. This basis is identical to what is obtained by starting with Casimir eigenstates and demanding that they satisfy Dirichlet boundary conditions, but it is computationally more efficient to implement. We leave the details of our numerical algorithm to section 4.C; below we will derive the Dirichlet inner product and explain the symmetrization procedure to obtain our final basis states.

Our Dirichlet states take the form as in eq. (4.B.5), which we reproduce here:

$$\begin{aligned}|\mathcal{O};\vec{P},k\rangle =&\frac{1}{\sqrt{2\pi}P_-^{n+|\boldsymbol{\lambda}_-|}\Lambda^{\frac{n-5}{2}+|\boldsymbol{\lambda}_\perp|}}\int_0^1\frac{d\bar{\mu}^2}{\bar{\mu}^{\frac{n-3}{2}+|\boldsymbol{\lambda}_\perp|}}g_k(\bar{\mu})\\&\times\frac{1}{n!}\int\frac{d^2p_1\cdots d^2p_n}{(2\pi)^{2n}2p_{1-}\cdots 2p_{n-}}(2\pi)^3\delta^3\left(\sum_i p_i-P\right)\\&\times p_{1-}p_{2-}\cdots p_{n-}\bar{F}_{\mathcal{O}}(p)|p_1,\cdots,p_n\rangle,\end{aligned}\tag{4.A.10}$$

where we have substituted in the Dirichlet wavefunction in eq. (4.A.2). The

inner product then takes the form

$$\langle \mathcal{O}'; \vec{P}', k' | \mathcal{O}; \vec{P}, k \rangle = \frac{2P_-(2\pi)^2\delta^2(\vec{P}-\vec{P}')}{2^n n!} \frac{1}{2\pi P_-^{2n+|\boldsymbol{\lambda}_-|+|\boldsymbol{\lambda}'_\perp|}\Lambda^{n-5+|\boldsymbol{\lambda}_\perp|+|\boldsymbol{\lambda}'_-|}}$$

$$\times \int_0^1 \frac{d\bar{\mu}^2}{\bar{\mu}^{\frac{n-3}{2}+|\boldsymbol{\lambda}_\perp|}} \int_0^1 \frac{d\bar{\mu}'^2}{\bar{\mu}'^{\frac{n-3}{2}+|\boldsymbol{\lambda}_\perp|}} g_k(\bar{\mu}^2) g_{k'}(\bar{\mu}'^2)(2\pi)\delta(\bar{\mu}^2-\bar{\mu}'^2)$$

$$\times \int \frac{d^2p_1\cdots d^2p_n}{(2\pi)^{2n}}(2\pi)^3\delta^3\left(\sum_i p_i - P\right) p_{1-}\cdots p_{n-}\bar{F}_{\mathcal{O}}(p)\bar{F}_{\mathcal{O}'}(p). \tag{4.A.11}$$

Using the equations of motion and the choice of our reference frame of $P_\perp = 0$, the set of delta functions can be recast as

$$\delta^3\left(\sum_i p_i - P\right) = \delta\left(\sum_i \frac{p_{i\perp}^2}{2p_{i-}} - \frac{\mu^2}{2P_-}\right)\delta\left(\sum_i p_{i-} - P_-\right)\delta\left(\sum_i p_{i\perp}\right). \tag{4.A.12}$$

Here, it is useful to define dimensionless variables

$$x_i \equiv \frac{p_{i-}}{P_-}, \qquad\qquad y_i \equiv \frac{p_{i\perp}}{\mu}, \tag{4.A.13}$$

so that the wavefunctions have a scaling set by

$$\tilde{F}_{\mathcal{O}}(p) = \mu^{|\boldsymbol{\lambda}_\perp|}P_-^{n+|\boldsymbol{\lambda}_-|}x_1\cdots x_n F_{\mathcal{O}}(x,y), \tag{4.A.14}$$

where $|\boldsymbol{\lambda}_\perp|$ counts the number of $P_\perp$ derivatives while $|\boldsymbol{\lambda}_-|$ counts the number of P_- derivatives in $\tilde{F}_{\mathcal{O}}(p)$. These scaling factors cancel against the factors coming from the $\bar{\mu}$ integration measure. Since our weight functions are *defined* to be orthonormal when integrated over μ^2 with unit measure, the inner product factorizes into an orthogonal piece with respect to k and k' and a piece

that depends on $\mathcal{O}$ and $\mathcal{O}'$:

$$\langle \mathcal{O}'; \vec{P}', k' | \mathcal{O}; \vec{P}, k \rangle = 2P_- (2\pi)^2 \delta^2(\vec{P} - \vec{P}') \delta_{kk'} \mathcal{I}_{\mathcal{O}'\mathcal{O}}. \tag{4.A.15}$$

To determine $\mathcal{I}_{\mathcal{O}'\mathcal{O}}$, we can choose integration variables defined by

$$\begin{aligned}
x_1 &= (1-z_1)(1-z_2)(1-z_3)\cdots(1-z_{n-1}), \\
x_2 &= \quad z_1(1-z_2)(1-z_3)\cdots(1-z_{n-1}), \\
x_3 &= \quad\quad z_2(1-z_3)\cdots(1-z_{n-1}), \\
&\vdots \qquad\qquad \ddots \\
x_n &= \quad\quad\quad\quad z_{n-1},
\end{aligned} \tag{4.A.16}$$

where the z_i range from $[0,1]$, and

$$\begin{aligned}
y_1 &= -(y_2 + y_3 + \cdots + y_n), \\
y_2 &= \tilde{y}_1 \sqrt{z_1(1-z_1)\cdots(1-z_{n-1})} - z_1(y_3 + \cdots + y_n), \\
y_3 &= \tilde{y}_2 \sqrt{z_2(1-z_2)\cdots(1-z_{n-1})} - z_2(y_4 + \cdots + y_n), \\
&\vdots \\
y_n &= \tilde{y}_{n-1} \sqrt{z_{n-1}(1-z_{n-1})}.
\end{aligned} \tag{4.A.17}$$

In these variables, the original set of delta functions we had simply reduce to

$$\delta^3\left(\sum_i p_i - P\right) \to \frac{2}{\mu^3} \delta\left(\sum_i^{n-1} \tilde{y}_i^2 - 1\right). \tag{4.A.18}$$

Introducing angular variables for the remaining $\tilde{y}$ variables to implement this

constraint

$$\begin{aligned}
\tilde{y}_1 &= \sin\theta_1 \sin\theta_2 \cdots \sin\theta_{n-2}, \\
\tilde{y}_2 &= \cos\theta_1 \sin\theta_2 \cdots \sin\theta_{n-2}, \\
\tilde{y}_3 &= \cos\theta_2 \sin\theta_3 \cdots \sin\theta_{n-2}, \\
&\vdots \\
\tilde{y}_{n-1} &= \cos\theta_{n-2},
\end{aligned} \tag{4.A.19}$$

where $\theta_i \in [0, \pi]$ for $i = 1, \ldots, n-3$ and $\theta_{n-2} \in [0, 2\pi]$, we find that the inner product becomes

$$\langle \mathcal{O}'; \vec{P}', k' | \mathcal{O}; \vec{P}, k \rangle = 2P_- (2\pi)^2 \delta^2(\vec{P} - \vec{P}') \delta_{kk'} \mathcal{I}_{\mathcal{O}'\mathcal{O}}, \tag{4.A.20}$$

with

$$\boxed{\begin{aligned}
\mathcal{I}_{\mathcal{O}'\mathcal{O}} = \frac{1}{n! 2^n (2\pi)^{2n-3}} \int dz_1 \cdots dz_{n-1} \left(\prod_i z_i^{\frac{3}{2}} (1 - z_i)^{\frac{5}{2} i - 1} \right) \\
\times \int d\theta_1 \cdots d\theta_{n-2} \left(\prod_j \sin^{j-1} \theta_j \right) \bar{F}_{\mathcal{O}}(z, \theta) \bar{F}_{\mathcal{O}'}(z, \theta).
\end{aligned}} \tag{4.A.21}$$

To obtain our final Dirichlet states, we tabulate a list of Dirichlet monomials at and below a given maximum Casimir eigenvalue $\mathcal{C}_{\max}$. This set of monomials will be overcomplete, so in order to determine the complete orthonormal basis, we compute the Gram matrix using eq. (4.A.21) between

different monomials. We then determine the final basis by performing a QR decomposition on the Gram matrix, the details of which we leave to Appendix 4.C.

4.B Matrix Elements and Operator Overlaps

In this section, we compute the matrix elements between the invariant mass M^2 and the Dircichlet basis states. The mass operator can be written in terms of momentum generators as

$$M^2 = 2P_+P_- - P_\perp^2. \tag{4.B.1}$$

However, since the Hamiltonian deformations we will study do not break translational invariance, we can choose a reference frame where P_- is fixed and $P_\perp = 0$. We can therefore compute the simpler matrix elements

$$\langle \mathcal{O}'; \vec{P}', k' | M^2 | \mathcal{O}; \vec{P}, k \rangle = 2P_- \langle \mathcal{O}'; \vec{P}', k' | P_+ | \mathcal{O}; \vec{P}, k \rangle. \tag{4.B.2}$$

These matrix elements take the form

$$\langle \mathcal{O}'; \vec{P}', k' | M^2 | \mathcal{O}; \vec{P}, k \rangle = 2P_- (2\pi)^2 \delta^2(\vec{P} - \vec{P}') \mathcal{M}_{\mathcal{O},\mathcal{O}',k,k'}. \tag{4.B.3}$$

We will suppress the overall kinematic factor and focus on the matrix elements $\mathcal{M}_{\mathcal{O},\mathcal{O}',k,k'}$ for the remainder of this section.

4.B.1 Kinetic Term

We begin by computing the M^2 matrix elements in the original CFT. The CFT Hamiltonian can be expressed in terms of raising and lowering operators as

$$P_+^{(\mathrm{CFT})} = \int \frac{d^2p}{(2\pi)^2} a_p^\dagger a_p \frac{p_\perp^2}{2p_-}. \tag{4.B.4}$$

Note that this term preserves particle number, so that we consider sectors with differing particle number separately. As discussed in section 4.A, our Dirichlet states take the form

$$\begin{aligned} |\mathcal{O};\vec{P},k\rangle =& \frac{1}{\sqrt{2\pi}P_-^{n+|\lambda_-|}\Lambda^{\frac{n-5}{2}+|\lambda_\perp|}} \int_0^1 \frac{d\bar{\mu}^2}{\bar{\mu}^{\frac{n-3}{2}+|\lambda_\perp|}} g_k(\bar{\mu}) \\ &\times \frac{1}{n!}\int \frac{d^2p_1\cdots d^2p_n}{(2\pi)^{2n}2p_{1-}\cdots 2p_{n-}}(2\pi)^3\delta^3\left(\sum_i p_i - P\right) \\ &\times p_{1-}p_{2-}\cdots p_{n-}\bar{F}_{\mathcal{O}}(p)|p_1,\cdots,p_n\rangle. \end{aligned} \tag{4.B.5}$$

Inserting eq. (4.B.4) in between two states and using the coordinate transformations in eqs. (4.A.16), (4.A.17), and (4.A.19) we find that

$$\boxed{\mathcal{M}^{(\mathrm{CFT})}_{k,k';\mathcal{O},\mathcal{O}'} = \Lambda^2\left(\frac{\mu_k^2+\mu_{k-1}^2}{2}\right)\delta_{k,k'}\mathcal{I}_{\mathcal{O},\mathcal{O}'}.} \tag{4.B.6}$$

4.B.2 Mass Term

The first deformation we consider to the UV Hamiltonian is the mass term, which results in a correction

$$\delta P_+^{(m)} = \int \frac{d^2p}{(2\pi)^2} a_p^\dagger a_p \frac{m^2}{2p_-}. \tag{4.B.7}$$

Like the kinetic term, this term preserves particle number. We can use the same coordinate transformations as in the inner product and kinetic terms to arrive at

$$\boxed{\begin{aligned}\mathcal{M}^{(m)}_{k,k';\mathcal{O},\mathcal{O}'} =& \delta_{k,k'}\frac{m^2}{(n-1)!2^n(2\pi)^{2n-3}}\int dz_1\cdots dz_{n-1}\left(\prod_i z_i^{\frac{3}{2}}(1-z_i)^{\frac{5}{2}i-1}\right)\\ &\times\left(\frac{1}{z_{n-1}}\right)\int d\theta_1\cdots d\theta_{n-2}\left(\prod_j \sin^{j-1}\theta_j\right)\bar{F}_{\mathcal{O}}(z,\theta)\bar{F}_{\mathcal{O}'}(z,\theta).\end{aligned}} \tag{4.B.8}$$

4.B.3 Quartic Interaction

We now move onto the more nontrivial deformation of a quartic interaction to the Hamiltonian, which gives rise to a Hamiltonian correction of the form

$$\delta P^{(\lambda)}_{+} = \frac{\lambda}{24}\int\frac{d^2pd^2qd^2k}{(2\pi)^6\sqrt{8p_-q_-k_-}}\left(\frac{4a^\dagger_p a^\dagger_q a^\dagger_k a_{p+q+k}}{\sqrt{2(p_-+q_-+k_-)}} + \text{ h.c. } + \frac{6a^\dagger_p a^\dagger_q a_k a_{p+q-k}}{\sqrt{2(p_-+q_--k_-)}}\right). \tag{4.B.9}$$

This deformation contains two types of terms, one that changes particle number and one that preserves it. We will refer to the former, which corresponds to the first two terms in eq. (4.B.9), as the n-to-$n+2$ interaction since it changes particle number by two. We will call the latter type of term in eq. (4.B.9) the n-to-n interaction.

Unlike the kinetic and mass terms, the interaction terms give rise to matrix elements that depend separately on both μ and μ'. In other words, the

discretization integrals over μ and μ' do not collapse into one simple integral, but instead depend on μ and μ' through the ratio

$$\boxed{\alpha \equiv \frac{\mu}{\mu'}.} \tag{4.B.10}$$

For this reason, we will introduce the useful notation

$$\langle \mathcal{O}'; \vec{P}', k' | \delta M^2 | \mathcal{O}; \vec{P}, k \rangle = 2P_-(2\pi)^2 \delta^2(\vec{P} - \vec{P}')$$
$$\times \frac{\lambda\Lambda}{2\pi} \frac{1}{P_-^{2n+|\boldsymbol{\lambda}_-|+|\boldsymbol{\lambda}'_\perp|} \Lambda^{n-5+|\boldsymbol{\lambda}_\perp|+|\boldsymbol{\lambda}'_-|}} \int_0^1 \frac{d\bar{\mu}^2}{\bar{\mu}^{\frac{n-3}{2}+|\boldsymbol{\lambda}_\perp|}} \int_0^1 \frac{d\bar{\mu}'^2}{\bar{\mu}'^{\frac{n-3}{2}+|\boldsymbol{\lambda}_\perp|}} g_k(\bar{\mu}^2) g_{k'}(\bar{\mu}'^2) \mathcal{M}_{\mathcal{O}\mathcal{O}'}(\alpha). \tag{4.B.11}$$

The computation of $\mathcal{M}_{\mathcal{O}\mathcal{O}'}(\alpha)$ for the interaction terms will be the main focus of the following two sections.

4.B.3.1 n-to-$n+2$ Interaction

Let's first consider the n-to-$n+2$ interaction, which gives rise to the following matrix element between an n particle state and an $n+2$ particle state:

$$\mathcal{M}^{(n\text{-to-}n+2)}_{\mathcal{O}\mathcal{O}'}(\alpha) = \frac{\lambda}{6(n-1)!} \int \frac{d^2p_1 \cdots d^2p_n}{(2\pi)^{2n} 2p_{1-} \cdots 2p_{n-}} (2\pi)^3 \delta^3 \left(\sum_i p_i - P \right) p_{1-} \cdots p_{n-} \bar{F}_{\mathcal{O}}(p)$$
$$\times \int \frac{d^2p'_1 \cdots d^2p'_{n+2}}{(2\pi)^{2n+4} 2p'_{1-} \cdots 2p'_{n+2-}} (2\pi)^3 \delta^3 \left(\sum_i p'_i - P' \right) p'_{1-} \cdots p'_{n+2-} \bar{F}_{\mathcal{O}'}(p')$$
$$\times 2p_{2-}(2\pi)^2 \delta^2(p_2 - p'_4) \cdots 2p_{n-}(2\pi)^2 \delta^2(p_n - p'_{n+2}). \tag{4.B.12}$$

It is useful to switch to the dimensionless variables defined in eq. (4.A.13) separately for the both the primed and unprimed variables. That is, we take

eq. (4.A.16)-(4.A.17) for the unprimed variables and

$$\begin{aligned} x_1' &= (1-z_1')(1-z_2')(1-z_3')\cdots(1-z_{n+1}'), \\ x_2' &= \quad z_1'(1-z_2')(1-z_3')\cdots(1-z_{n+1}'), \\ x_3' &= \quad\quad z_2'(1-z_3')\cdots(1-z_{n+1}'), \\ &\vdots \quad\quad\quad\quad \ddots \\ x_{n+2}' &= \quad\quad\quad\quad\quad z_{n+1}' \end{aligned} \tag{4.B.13}$$

for the primed coordinates and analogously for eq. (4.A.17). We then find

$$\begin{aligned} \mathcal{M}_{\mathcal{O}\mathcal{O}'}^{(n\text{-to-}n+2)}(\alpha) &= \frac{\lambda n\sqrt{(n+1)(n+2)}}{24\pi}\frac{1}{\mu'}\alpha^{\frac{n-3}{2}}\int dz_1\cdots dz_{n-1}d\tilde{y}_1\cdots d\tilde{y}_{n-1} \\ &\times\left(\prod_{i=1}^{n-1} z_i^{\frac{3}{2}}(1-z_i)^{\frac{5}{2}i+1}\right)\delta\left(\sum_i^{n-1}\tilde{y}_{n-1}^2-1\right)F_{\mathcal{O}}(z,\tilde{y}) \\ &\times\int dz_1'dz_2'd\tilde{y}_1'd\tilde{y}_2'\,z_1'^{\frac{1}{2}}(1-z_1')^{\frac{1}{2}}z_2'^{\frac{1}{2}}(1-z_2')^2 \\ &\times\delta\left(\tilde{y}_1'^2+\tilde{y}_2'^2+\alpha^2\sum_{i=1}^{n-1}\tilde{y}_i^2-1\right)\bar{F}_{\mathcal{O}'}(z',\tilde{y},\tilde{y}'). \end{aligned} \tag{4.B.14}$$

The first delta function constrains the $n-1$ $\tilde{y}$'s, which correspond to the variables of the "spectator" particles, to a sphere of radius 1. The other delta function for the interacting particles constrains $\tilde{y}'$ to a sphere of radius $1-\alpha^2$, which constrains $\alpha \leq 1$. Physically, this is due to the fact that the n-to-$n+2$ interactions can only increase the kinetic energy due to the creation of two additional particles. Parameterizing these two spheres with angular variables

for the spectators and interacting particles we obtain

$$\boxed{\begin{aligned}\mathcal{M}_{\mathcal{O}\mathcal{O}'}^{(n\text{-to-}n+2)}(\alpha) &= \frac{1}{(n-1)!3\pi^{2n}2^{3n+4}}\frac{1}{\mu'}\alpha^{\frac{n-3}{2}} \\ &\times \int dz_1\cdots dz_{n-1}dz_1'dz_2'\left(\prod_{i=1}^{n-1} z_i^{\frac{3}{2}}(1-z_i)^{\frac{5}{2}i+1}\right) z_1'^{\frac{1}{2}}(1-z_1')^{\frac{1}{2}}z_2'^{\frac{1}{2}}(1-z_2')^2 \\ &\times \int d\theta_1\cdots d\theta_{n-2}d\theta'\left(\prod_j \sin^{j-1}\theta_j\right)\bar{F}_{\mathcal{O}}(z,\theta)\bar{F}_{\mathcal{O}}(z',\theta',\theta,\alpha).\end{aligned}} \tag{4.B.15}$$

4.B.3.2 n-to-n Interaction

Finally, we turn to the n-to-n part of the quartic interaction. It takes the form

$$\begin{aligned}\mathcal{M}_{\mathcal{O}\mathcal{O}'}^{(n-\text{to}-n)}(\alpha) =& \frac{\lambda n(n-1)}{4}\frac{1}{n!}\int \frac{d^2p_1\cdots d^2p_n}{(2\pi)^{2n}2p_{1-}\cdots 2p_{n-}}(2\pi)^3\delta^3\left(\sum_i p_i - P\right) \\ &\times p_{1-}\cdots p_{n-}F_{\mathcal{O}}(p)\int \frac{d^2p_1'\cdots d^2p_n'}{(2\pi)^{2n}2p_{1-}'\cdots 2p_{n-}'} \\ &\times (2\pi)^3\delta^3\left(\sum_i p_i' - P'\right)p_{1-}'\cdots p_{n-}'\bar{F}_{\mathcal{O}}(p') \\ &\times 2p_{3-}(2\pi)^2\delta^2(p_3-p_3')\cdots 2p_{n-}(2\pi)^2\delta^2(p_n-p_n').\end{aligned} \tag{4.B.16}$$

Performing the coordinate transforms in eqs. (4.A.16)-(4.A.17) for both the primed and unprimed coordinates, we find

$$\begin{aligned}\mathcal{M}_{\mathcal{O}\mathcal{O}'}^{(n-\text{to}-n)}(\alpha) =& \frac{\lambda n(n-1)\alpha^{\frac{n-3}{2}}}{16\pi\mu'} \int dz_1 d\tilde{y}_1 dz_1' d\tilde{y}_1' \sqrt{z_1(1-z_1)z_1'(1-z_1')} \\ & \times \delta\left(\sum_i \tilde{y}_i^2 - 1\right) \delta\left(\tilde{y}_1'^2 + \alpha^2 \sum_{i=2} \tilde{y}_i^2 - 1\right) \\ & \times \int dz_2 \cdots dz_{n-1} d\tilde{y}_2 \cdots d\tilde{y}_{n-1} \left(\prod_{i>1} z_i^{\frac{3}{2}} (1-z_i)^{\frac{5i-3}{2}}\right) \\ & \times F_{\mathcal{O}}(z,\tilde{y}) F_{\mathcal{O}}(z',\tilde{y}').\end{aligned} \tag{4.B.17}$$

We can use the delta functions to perform the integration over the $\tilde{y}$ coordinates of the interacting particles. Note that they impose the constraints

$$\tilde{y}_1 = \pm\sqrt{1-r^2}, \qquad \tilde{y}_1' = \pm\sqrt{1-\alpha^2 r^2}, \tag{4.B.18}$$

where

$$r^2 \equiv \tilde{y}_2^2 - \tilde{y}_3^2 \cdots - \tilde{y}_{n-1}^2. \tag{4.B.19}$$

Note that when $\alpha = 1$, the two constraints coincide, and the range of integration r is taken to be between $[0,1]$. Similarly, when $\alpha < 1$, the reality condition on $\tilde{y}_1$ requires $r \in [0,1]$, which automatically satisfies the constraint on $\tilde{y}_1'$. However, when $\alpha > 1$, the reality condition on $\tilde{y}_1'$ provides a stronger constraint and requires $r \in [0, \alpha^{-1}]$.

Defining spherical coordinates for the remaining spectators

$$\begin{aligned}
\tilde{y}_2 &= r \sin\theta_1 \sin\theta_2 \cdots \sin\theta_{n-3}, \\
\tilde{y}_3 &= r \cos\theta_1 \sin\theta_2 \cdots \sin\theta_{n-3}, \\
\tilde{y}_4 &= r \cos\theta_2 \sin\theta_3 \cdots \sin\theta_{n-3}, \\
&\vdots \\
\tilde{y}_{n-1} &= r \cos\theta_{n-3},
\end{aligned} \tag{4.B.20}$$

and defining

$$F_{\mathcal{O}\pm} \equiv F_{\mathcal{O}}(\tilde{y}_1 = \pm\sqrt{1-r^2}), \qquad F_{\mathcal{O}'\pm} \equiv F_{\mathcal{O}'}(\tilde{y}_1 = \pm\sqrt{1-\alpha^2 r^2}), \tag{4.B.21}$$

the matrix element can be summarized as

$$\begin{aligned}
\mathcal{M}^{(n\text{-to-}n)}_{\mathcal{O}\mathcal{O}'}(\alpha) &= \frac{1}{(n-2)!\pi^{2n-2}2^{3n+2}}\frac{1}{\mu'}\alpha^{\frac{n-3}{2}} \\
&\times \int dz_1\cdots dz_{n-1}dz_1'\sqrt{z_1(1-z_1)z_1'(1-z_1')}\left(\prod_{i>1} z_i^{\frac{3}{2}}(1-z_i)^{\frac{5i-3}{2}}\right) \\
&\times \int_0^{\min\left(1,\alpha^{-1}\right)} dr \int d\theta_1\cdots d\theta_{n-3}\left(\prod_j \sin^{j-1}\theta_j\right)\frac{r^{n-3}}{\sqrt{(1-r^2)(1-\alpha^2r^2)}} \\
&\times \left(\sum_{\pm}\bar{F}_{\mathcal{O}}(z,r,\theta)\right)\left(\sum_{\pm}\bar{F}_{\mathcal{O}'}(z,\alpha r,\theta)\right).
\end{aligned} \tag{4.B.22}$$

4.C Details of Code and Algorithms

Broadly speaking, the goal of the program is to reduce as many computations as possible to pure linear algebra operations. This allows us both to avoid a great deal of repeated work and to take advantage of established libraries for linear algebra. So in order to do this, we need a basis for all relevant operators and we need to express the quantities of interest as vectors and matrices on

this basis.

Our computation begins with a naive list of all Dirichlet monomials having total scaling dimension below some cutoff Δ. We intend to use this as a basis for all states below the cutoff, but since it's vastly overcomplete, we must first eliminate all of the redundant monomials, the first step of which is to compute the Gram matrix containing the inner products of all of the monomials in the naive list with all of the others. Before computing the Gram matrix, we normalize the input monomials so that it's easier to distinguish floating point epsilons from inner products which just happen to be small, and we also separate the states with an even number of $P_\perp$ derivatives from those with an odd number: the former are always orthogonal to the latter, and their matrix elements with each other are always zero, so we can treat both cases separately. Since matrix algorithms generally have complexity of roughly $O(N^3)$, any simplification which breaks the overall matrix up into invariant subspaces is tremendously advantageous.

With the Gram matrix in hand, there are a number of ways to produce an orthogonal basis from the overcomplete one, the simplest of them being a QR decomposition. However, the QR decomposition of a rank-deficient matrix is not unique, and the Gram matrix is rank-deficient due to the basis being overcomplete. This is a mixed blessing: while it means that off-the-shelf QR decomposition functions will often yield a correct but non-useful basis, it also means that we have a lot of freedom to arrange to produce the most convenient basis possible.

Our implementation uses the Modified Gram-Schmidt Algorithm [75],

feeding in monomials one at a time starting with the monomials with the most evenly distributed powers of P_- and $P_\perp$. This produces a basis where the fewest possible monomials are used, which is desirable because it's $O(N^2)$ easier to compute matrix elements between single monomials than between arbitrary superpositions of them. The evenly distributed exponents on the monomials means that each individual monomial will have fewer unique permutations, again simplifying the computation of the matrix elements.

Note that the Gram-Schmidt process produces exponentially compounding roundoff errors in the coefficients of the output vectors because each coefficient depends on all of the ones before it. Because of this problem, we found that we had to use 128-bit precision floating point numbers to keep epsilons from growing to sizes comparable to the actual answers; if one were to increase total scaling dimension beyond what we attempted, one would likely need to increase the precision further, which could quickly create performance bottlenecks.

Having finished Gram-Schmidt and obtained a basis of orthonormal states, the next step is to actually compute the matrix elements between these states. All of the matrix elements are bilinear in the two states' reduced wavefunctions $\bar{F}$, which themselves are sums of permutations of ordered monomials. This suggests a second layer of linear algebra structure: we can represent the orthonormal basis states as vectors on the (non-orthonormal) space of ordered monomials which appear in them.

We refer to this latter space as the 'minimal basis' and write the orthonormal polynomial basis as a matrix P whose columns each represent one of

the polynomials, with entry (i, j) giving the contribution of minimal basis monomial i to orthonormal polynomial j. Now, to produce matrix elements between the orthonormal basis polynomials, we can simply compute the matrix elements M_{ij} between minimal basis monomials and transform them to $P^T MP$, producing exactly the desired matrix. Note that M and P are precisely the same size in our implementation, thanks to our choice of orthogonalization of the naive basis – if we had not deliberately selected one which used as few individual monomials as possible, M could have been several times larger.

The matrix M is properly a 4th-order tensor relating the kth μ^2 partition of monomial m to the k'th μ^2 partition of monomial m', i.e. we're computing the entries $M_{mkm'k'}$. For computation simplicity, however, we actually treat this as a matrix: if there are N_m minimal basis monomials and N_k μ^2 partitions, then M is an $N_m N_k \times N_m N_k$ matrix where each pair of monomials has its own $N_k \times N_k$ block.

We compute M block by block, first getting an overall factor a by doing all of the integrals not involving μ^2, then computing a discretization matrix D and multiplying it by a. The entry D_{ij} contains the integral of all μ^2 factors across the appropriate window:

$$D_{ij} = \int_{i/N_k}^{(i+1)/N_k} d\mu^2 \int_{j/N_k}^{(j+1)/N_k} d\mu'^2 f(\mu^2, \mu'^2). \tag{4.C.1}$$

For the kinetic and mass matrices, $f(\mu^2, \mu'^2)$ is just proportional to $\delta(\mu^2 - \mu'^2)$, while for the interaction matrices it's close to a polynomial in μ^2/μ'^2. We memoized each discretization matrix in a hash table keyed by $f(\mu^2, \mu'^2)$, so a matrix element calculation can be represented with the following pseudocode:

```
for each unique permutation of m and m':
 do integrals to get {numerical factor a} and {list of which f appear}
  for each f which appears:
    answer += a * D(f)
return answer * degeneracy
```

where the degeneracy is the number of permutations which are indistinguishable from a given unique permutation; which is of course the same for every unique permutation so it becomes an overall factor. Note that if the integrals in (4.C.1) can be done analytically, it's possible to program in the answers as a function of a given set of input exponents. This is fantastically faster and more precise than a numerical integration, being able to quickly get 10 or 15 decimal digits of precision while the latter struggles to get 5.

Once all of the minimal basis matrices M have been computed, everything else is just standard matrix algebra. In particular, the Hamiltonian is just

$$\sum_i P^T M_i P, \tag{4.C.2}$$

summed over the kinetic, mass, and interaction terms. Interesting quantities like eigenvalues can then be computed using ordinary matrix libraries; one might think that some special care is required to take advantage of various properties of the matrix, for instance the fact that it is "block sparse" in that the block of n-particle states is coupled only to itself and the blocks of $n-2$- and $n+2$-particle states. However, because the bulk of the states lie in the middle of the particle number range, this actually includes quite a large proportion of the possible pairs, and in fact upon inspection one sees that the matrix

is about half full at $\Delta_{\max} = 10$. If $\Delta_{\max}$ were increased further, the matrix would become increasingly sparse (technically block sparse), but we do not expect that it would be worth considering sparse methods such as the Lanczos algorithm until $\Delta_{\max} = 15$ or higher.

Using the double linear algebra formulation and aggressive memoization of all the repeated work we could find, we were able to produce finished matrices up to $\Delta_{\max} = 10, k_{\max} = 100$ on an ordinary desktop computer in around two minutes. We believe that we will be able to solve everything up to around $\Delta_{\max} = 15$ before the resulting matrices become too large to deal with; this is our main obstacle, since $k_{\max}$ must be kept high to maintain good convergence. If $k_{\max}$ is kept at 100, the final matrices become unwieldy once more than about 100 orthogonal states are introduced, which happens at around $\Delta_{\max} = 15$.

Chapter 5

Discussion and Conclusion

The analyses in both of the preceding chapters represent ways of using numerical computation to attack problems from unexpected angles. Whereas quantum field theory is most often solved using perturbation theory in weak interaction, these projects present entirely orthogonal solutions. In chapter 3, the power series found by the program is the *exact* correct answer up to the given power in q (floating point errors notwithstanding) – accuracy of the predictions is guaranteed within a given coordinate range, entirely irrespective of the mass of the objects or the strength of the gravitational interaction. In chapter 4, the program creates a Hamiltonian for the system which is exactly correct for all of the states included – the approximation is in ignoring the higher energy states rather than making any assumptions about the strength of the interactions.

Accordingly, numerical methods can answer problems which are essentially intractable in traditional analytic, proof-based particle physics. The best known analytic treatment of the AdS_3 black hole system remains the semiclassical approximation to which we compare our results – as we demonstrated,

this approximation completely fails to capture the resolution of the paradox. The behavior could only be found using numerical methods grounded in a carefully chosen angle of attack.

Similarly, while the comparisons in chapter 4 are grounded in the relatively well understood 3d Ising model, many aspects of this model remain unknown, and the conformal truncation method we use can easily be adapted to study any low energy effective theory which can be thought of as a CFT deformed by some relevant operator. This is a very broad class of theories, and we expect that conformal truncation will yield many otherwise inaccessible results when applied to systems from particle theory and particularly condensed matter.

We would also like to point out that neither of these projects would have been possible without a cross-disciplinary understanding of various efficiency-related topics in computer science. Both make extensive use of dynamic programming, and both use a number of data structures and algorithms which were carefully selected to minimize repeated work and maximize parallelizability without explicit synchronization. We believe that many outstanding problems in theoretical physics would be amenable to resolution by a combined approach using both physics and computer science, and would encourage any physicists interested in computation to improve their understanding of algorithm design by working through short CS problems like those at Project Euler.

Ultimately, since the problems of theoretical physics are becoming more mathematically complex while computers are becoming more powerful, we expect that the application of cross-disciplinary numerical methods like those

used in this thesis will grow increasingly common. When combined with novel mathematical approaches like AdS/CFT holography, we believe that computation represents a compelling forefront for particle physics research, and we are glad to have had the opportunity to contribute to it.

References

[1] S. Weinberg, *The Quantum Theory of Fields. Vol. 1: Foundations* (Cambridge University Press, 2005).

[2] M. Perelstein, "Introduction to collider physics", TASI Proceedings (2009).

[3] I. E. D. A. A. Abrikosov L. P. Gor'kov, *Methods of quantum field theory in statistical physics* (Prentice-Hall, New Jersey, 1963).

[4] S. W. Hawking, "Particle Creation by Black Holes", Commun. Math. Phys. 43, 199–220 (1975).

[5] R. Sundrum, "From Fixed Points to the Fifth Dimension", Phys.Rev. D86, 085025 (2012).

[6] J. M. Maldacena, "The large N limit of superconformal field theories and supergravity", Adv. Theor. Math. Phys. **2**, 231–252 (1998).

[7] J. Polchinski, "Introduction to Gauge/Gravity Duality", (2010).

[8] J. Kaplan, "Lectures on ads/cft from the bottom up", (2013).

[9] A. L. Fitzpatrick, J. Kaplan, and M. T. Walters, "Universality of Long-Distance AdS Physics from the CFT Bootstrap", JHEP **1408**, 145 (2014).

[10] A. L. Fitzpatrick, J. Kaplan, and M. T. Walters, "Virasoro Conformal Blocks and Thermality from Classical Background Fields", (2015).

[11] A. L. Fitzpatrick, J. Kaplan, M. T. Walters, and J. Wang, "Hawking from Catalan", (2015).

[12] A. L. Fitzpatrick and J. Kaplan, "Conformal Blocks Beyond the Semi-Classical Limit", (2015).

[13] A. Liam Fitzpatrick and J. Kaplan, "On the Late-Time Behavior of Virasoro Blocks and a Classification of Semiclassical Saddles", (2016).

[14] T. Anous, T. Hartman, A. Rovai, and J. Sonner, "Black Hole Collapse in the 1/c Expansion", (2016).

[15]A. L. Fitzpatrick, J. Kaplan, D. Li, and J. Wang, "On Information Loss in AdS_3/CFT_2", (2016).

[16]E. Hijano, P. Kraus, and R. Snively, "Worldline approach to semi-classical conformal blocks", (2015).

[17]E. Hijano, P. Kraus, E. Perlmutter, and R. Snively, "Semiclassical Virasoro Blocks from AdS_3 Gravity", (2015).

[18]M. Besken, A. Hegde, E. Hijano, and P. Kraus, "Holographic conformal blocks from interacting Wilson lines", JHEP **08**, 099 (2016).

[19]K. B. Alkalaev and V. A. Belavin, "Classical conformal blocks via AdS/CFT correspondence", JHEP **08**, 049 (2015).

[20]K. B. Alkalaev and V. A. Belavin, "Monodromic vs geodesic computation of Virasoro classical conformal blocks", (2015).

[21]O. Hulik, T. Prochazka, and J. Raeymaekers, "Multi-centered AdS3 solutions from Virasoro conformal blocks", (2016).

[22]A. L. Fitzpatrick, J. Kaplan, D. Li, and J. Wang, "Exact Virasoro Blocks from Wilson Lines and Background-Independent Operators", (2016).

[23]M. Besken, A. Hegde, and P. Kraus, "Anomalous dimensions from quantum Wilson lines", (2017).

[24]A. Zamolodchikov, "Conformal Symmetry in Two-Dimensions: An Explicit Recurrence Formula for the Conformal Partial Wave Amplitude", Commun.Math.Phys. **96**, 419–422 (1984).

[25]A. Zamolodchikov, "Conformal Symmetry in Two-dimensional Space: Recursion Representation of the Conformal Block", Teoreticheskaya i Matematicheskaya Fizika **73**, 103–110 (1987).

[26]A. B. Zamolodchikov and V. A. Fateev, "Disorder Fields in Two-Dimensional Conformal Quantum Field Theory and N=2 Extended Supersymmetry", Sov. Phys. JETP **63**, 913–919 (1986).

[27]E. Plamadeala, M. Mulligan, and C. Nayak, "Perfect Metal Phases of One-Dimensional and Anisotropic Higher-Dimensional Systems", Phys. Rev. **B90**, 241101 (2014).

[28]J. M. Maldacena, "Eternal black holes in anti-de Sitter", JHEP **04**, 021 (2003).

[29]P. Hayden and J. Preskill, "Black holes as mirrors: Quantum information in random subsystems", JHEP **09**, 120 (2007).

[30]J. Maldacena, S. H. Shenker, and D. Stanford, "A bound on chaos", (2015).

[31]J. L. Cardy, "Operator Content of Two-Dimensional Conformally Invariant Theories", Nucl.Phys. B270, 186–204 (1986).

[32]D. Pappadopulo, S. Rychkov, J. Espin, and R. Rattazzi, "OPE Convergence in Conformal Field Theory", (2012).

[33]A. L. Fitzpatrick, J. Kaplan, D. Poland, and D. Simmons-Duffin, "The Analytic Bootstrap and AdS Superhorizon Locality", JHEP 1312, 004 (2013).

[34]Z. Komargodski and A. Zhiboedov, "Convexity and Liberation at Large Spin", JHEP 1311, 140 (2013).

[35]J. Maldacena, D. Simmons-Duffin, and A. Zhiboedov, "Looking for a bulk point", (2015).

[36]A. Hamilton, D. N. Kabat, G. Lifschytz, and D. A. Lowe, "Local bulk operators in AdS/CFT: A Boundary view of horizons and locality", Phys.Rev. D73, 086003 (2006).

[37]R. Bousso, B. Freivogel, S. Leichenauer, V. Rosenhaus, and C. Zukowski, "Null Geodesics, Local CFT Operators and AdS/CFT for Subregions", Phys. Rev. D88, 064057 (2013).

[38]S. Leichenauer and V. Rosenhaus, "AdS black holes, the bulk-boundary dictionary, and smearing functions", Phys. Rev. D88, 026003 (2013).

[39]I. A. Morrison, "Boundary-to-bulk maps for AdS causal wedges and the Reeh-Schlieder property in holography", JHEP 05, 053 (2014).

[40]K. Papadodimas and S. Raju, "An Infalling Observer in AdS/CFT", JHEP 10, 212 (2013).

[41]K. Papadodimas and S. Raju, "State-Dependent Bulk-Boundary Maps and Black Hole Complementarity", Phys. Rev. D89, 086010 (2014).

[42]A. Almheiri, D. Marolf, J. Polchinski, D. Stanford, and J. Sully, "An Apologia for Firewalls", JHEP 09, 018 (2013).

[43]E. Perlmutter, "Virasoro conformal blocks in closed form", JHEP 08, 088 (2015).

[44]D. Harlow, J. Maltz, and E. Witten, "Analytic Continuation of Liouville Theory", JHEP 1112, 071 (2011).

[45]T. Hartman, "Entanglement Entropy at Large Central Charge", (2013).

[46]S. Collier, P. Kravchuk, Y.-H. Lin, and X. Yin, "Bootstrapping the Spectral Function: On the Uniqueness of Liouville and the Universality of BTZ", (2017).

[47]L. F. Alday, "Large Spin Perturbation Theory", (2016).

[48]H. Chen, A. L. Fitzpatrick, J. Kaplan, D. Li, and J. Wang, "Degenerate Operators and the $1/c$ Expansion: Lorentzian Resummations, High Order Computations, and Super-Virasoro Blocks", (2016).

[49]J. L. F. Barbon and E. Rabinovici, "Geometry And Quantum Noise", Fortsch. Phys. **62**, 626–646 (2014).

[50]J. S. Cotler, G. Gur-Ari, M. Hanada, J. Polchinski, P. Saad, S. H. Shenker, D. Stanford, A. Streicher, and M. Tezuka, "Black Holes and Random Matrices", (2016).

[51]E. Dyer and G. Gur-Ari, "2D CFT Partition Functions at Late Times", (2016).

[52]A. del Campo, J. Molina-Vilaplana, and J. Sonner, "Scrambling the spectral form factor: unitarity constraints and exact results", (2017).

[53]T. Guhr, A. Muller-Groeling, and H. A. Weidenmuller, "Random matrix theories in quantum physics: Common concepts", Phys. Rept. **299**, 189–425 (1998).

[54]A. M. García-García and J. J. M. Verbaarschot, "Spectral and thermodynamic properties of the Sachdev-Ye-Kitaev model", Phys. Rev. **D94**, 126010 (2016).

[55]B. Ponsot and J. Teschner, "Liouville bootstrap via harmonic analysis on a noncompact quantum group", (1999).

[56]J. Teschner, "A Lecture on the Liouville vertex operators", Int. J. Mod. Phys. **A19S2**, 436–458 (2004).

[57]S. Ferrara, A. Grillo, and R. Gatto, "Tensor representations of conformal algebra and conformally covariant operator product expansion", Annals Phys. **76**, 161–188 (1973).

[58]A. M. Polyakov, "Non-Hamiltonian Approach to the Quantum Field Theory at Small Distances", Zh.Eksp.Teor.Fiz. (1973).

[59]R. Rattazzi, V. S. Rychkov, E. Tonni, and A. Vichi, "Bounding scalar operator dimensions in 4D CFT", JHEP **12**, 031 (2008).

[60]P. Kraus and A. Maloney, "A Cardy Formula for Three-Point Coefficients: How the Black Hole Got its Spots", (2016).

[61]D. L. Jafferis, "Bulk reconstruction and the Hartle-Hawking wavefunction", (2017).

[62]A. Almheiri, D. Marolf, J. Polchinski, and J. Sully, "Black Holes: Complementarity or Firewalls?", (2012).

[63]D. Kabat and G. Lifschytz, "Finite N and the failure of bulk locality: Black holes in AdS/CFT", JHEP **09**, 077 (2014).

[64]E. Witten, "Analytic Continuation Of Chern-Simons Theory", AMS/IP Stud. Adv. Math. **50**, 347–446 (2011).

[65]T. Granlund, *The gnu multiple precision arithmetic library*, 6.1.2 ().

[66]L. Fousse, G. Hanrot, V. Lefèvre, P. Pélissier, and P. Zimmerman, *Mpfr: a multiple-precision binary floating-point library with correct rounding*, 3.1.5 (2007).

[67]A. Enge, M. Gastineau, P. Th'eveny, and P. Zimmerman, *Mpc — a library for multiprecision complex arithmetic with exact rounding*, 1.0.3, INRIA (2015).

[68]P. Holoborodko, *Mpfr c++* (2008-2015).

[69]M. Peskin and D. Schroeder, *An Introduction to Quantum Field Theory* (Westview Press, 1995).

[70]A. Bazavov, D. Toussaint, C. Bernard, J. Laiho, C. Detar, L. Levkova, M. B. Oktay, S. Gottlieb, U. M. Heller, J. E. Hetrick, P. B. MacKenzie, R. Sugar, and R. S. van de Water, "Nonperturbative QCD simulations with 2+1 flavors of improved staggered quarks", Reviews of Modern Physics **82**, 1349–1417 (2010).

[71]D. Lee, N. Salwen, and D. Lee, "The diagonalization of quantum field Hamiltonians", Physics Letters B **503**, 223–235 (2001).

[72]V. P. YUROV and A. B. ZAMOLODCHIKOV, "Truncated comformal space approach to scaling lee-yang model", International Journal of Modern Physics A **05**, 3221–3245 (1990).

[73]E. Katz, Z. U. Khandker, and M. T. Walters, "A conformal truncation framework for infinite-volume dynamics", Journal of High Energy Physics **2016**, 140 (2016).

[74]N. Anand, V. X. Genest, E. Katz, Z. U. Khandker, and M. T. Walters, "RG flow from ϕ^4 theory to the 2D Ising model", Journal of High Energy Physics **2017**, 56 (2017).

[75]P.-O. Persson, "Gram-Schmidt Orthogonalization", (2006).

Biography

Charles Hussong was born on July 4th, 1989 in Boston, Massachusetts. Charles was homeschooled from age 7 until entering Cornell University as an undergraduate. He received a B.A. from Cornell in 2011 with majors in Physics and Mathematics and a minor in Asian Studies, and in 2012 entered the Ph.D. program in the Physics and Astronomy department at Johns Hopkins University.

Charles was a teaching assistant for introductory physics the entire time he was at Hopkins, and was the head teaching assistant for Physics II for Engineers for three years, during which the course was changed from a traditional lecture into a group-based active learning format. He was the recipient of JHU's 2016 Excellence in Teaching Award for graduate teaching assistant.

Charles's research at Hopkins has been in theoretical particle physics, focusing on conformal field theories. While he originally worked on the conformal bootstrap, his interests shifted toward numerical analysis like those presented in this thesis. He has ultimately decided to follow this interest in numerics into a career in software engineering after graduation.